TU/e EINDHOVEN UNIVERSITY OF TECHNOLOGY

Non-equilibrium in flowing atmospheric plasmas

Citation for published version (APA):
de Haas, J. C. M. (1986). *Non-equilibrium in flowing atmospheric plasmas*. [Phd Thesis 1 (Research TU/e / Graduation TU/e), Applied Physics and Science Education]. Technische Universiteit Eindhoven. https://doi.org/10.6100/IR250619

DOI:
10.6100/IR250619

Document status and date:
Published: 01/01/1986

Document Version:
Publisher's PDF, also known as Version of Record (includes final page, issue and volume numbers)

Please check the document version of this publication:

• A submitted manuscript is the version of the article upon submission and before peer-review. There can be important differences between the submitted version and the official published version of record. People interested in the research are advised to contact the author for the final version of the publication, or visit the DOI to the publisher's website.
• The final author version and the galley proof are versions of the publication after peer review.
• The final published version features the final layout of the paper including the volume, issue and page numbers.

Link to publication

General rights
Copyright and moral rights for the publications made accessible in the public portal are retained by the authors and/or other copyright owners and it is a condition of accessing publications that users recognise and abide by the legal requirements associated with these rights.

• Users may download and print one copy of any publication from the public portal for the purpose of private study or research.
• You may not further distribute the material or use it for any profit-making activity or commercial gain
• You may freely distribute the URL identifying the publication in the public portal.

If the publication is distributed under the terms of Article 25fa of the Dutch Copyright Act, indicated by the "Taverne" license above, please follow below link for the End User Agreement:

www.tue.nl/taverne

Take down policy
If you believe that this document breaches copyright please contact us at:

openaccess@tue.nl

providing details and we will investigate your claim.

Download date: 16. Nov. 2023

NON-EQUILIBRIUM IN FLOWING ATMOSPHERIC PLASMAS

J.C.M. DE HAAS

NON-EQUILIBRIUM IN FLOWING ATMOSPHERIC PLASMAS

PROEFSCHRIFT

ter verkrijging van de graad van doctor aan de Technische Universiteit Eindhoven, op gezag van de rector magnificus, prof. dr. F.N. Hooge, voor een commissie aangewezen door het college van dekanen in het openbaar te verdedigen op dinsdag 30 september 1986 te 16.00 uur

door

JOHANNES CORNELIS MARIA DE HAAS

geboren te Someren

Druk: Dissertatiedrukkerij Wibro, Helmond.

Dit proefschrift is goedgekeurd door de promotoren:

Prof.dr.ir. D.C. Schram
en
Prof.dr. L.H.Th. Rietjens

copromotor dr. A. Veefkind

Aan mijn ouders

CONTENTS

1. GENERAL INTRODUCTION 1

2. BASIC EQUATIONS 2
2.1 Introduction 2
2.2 Mass, momentum, and energy balances 3
2.3 Source terms 4
2.3.1 Collisional radiative model 4
2.3.2 Source terms in the mass balance 10
2.3.3 Source terms in the energy balance 15
2.3.4 The escape of radiation 19
2.4 Transport quantities 22
2.4.1 Diffusion coefficients 22
2.4.2 Electrical conductivity 22
2.4.3 Heat conductivity 23
2.4.4 Heat exchange between electrons and heavy particles 24
2.5 Formulation of the balance equations 24
2.6 Independent thermodynamic variables 25

3. THE PLASMA IN A CLOSED CYCLE MHD GENERATOR 27
3.1 Introduction 27
3.2 Shock tube MHD facility 28
3.3 Discharge structure of a closed cycle linear MHD generator 30
3.4 Present work 33

4. THEORETICAL DESCRIPTION OF A LOW TEMPERATURE AR-CS PLASMA 34
4.1 Introduction 34
4.2 Ionization of neutral cesium 38
4.2.1 The escape of resonance radiation 38
4.2.2 Results of a model with three levels 46
4.2.3 Results of a model with many levels 51
4.2.4 The net source term 54
4.3 The electron mass balance 58
4.3.1 The contribution of transport 58
4.3.2 Deviation from equilibrium 60
4.4 The electron energy balance 61
4.4.1 Source and transport terms 61

4.4.2 Dependence on the radius 66
4.5 The combined balances for the electrons 69
4.6 Conclusions 76

5. COLLECTIVE CO_2 LASER SCATTERING ON MOVING DISCHARGE STRUCTURES IN THE SUBMILLIMETER RANGE IN A MAGNETOHYDRODYNAMIC GENERATOR 78
I. INTRODUCTION 78
II. THE HETERODYNE MIXING TECHNIQUE 78
III. THEORY 79
IV. EXPERIMENTAL RESULTS 80
V. THE STREAMER MODEL 81
VI. CONCLUSIONS AND REMARKS 83
ACKNOWLEDGEMENTS 83
REFERENCES 83

6. THE PLASMA IN AN ARGON CASCADE ARC 84
6.1 Introduction 84
6.2 Cascade arc construction 84
6.3 Non-equilibrium in an atmospheric argon plasma 85
6.4 Present work 87

7. THEORETICAL DESCRIPTION OF A CASCADE ARC WITH FLOW 89
7.1 Introduction 89
7.2 Balance equations 89
7.3 Thermodynamic properties 92
7.4 One-dimensional model 101
7.4.1 Basic formulation 101
7.4.2 Boundary conditions 107

8. EXPERIMENTS ON A CASCADE ARC WITH FLOW 109
8.1 Introduction 109
8.2 Measuring procedure 109
8.3 Temperature and flow speed determination 112
8.4 Results and discussion 116
8.5 Conclusions 121

9. CONCLUSIONS 123

REFERENCES 126

SUMMARY 130

SAMENVATTING 133

DANKWOORD 136

CURRICULUM VITAE 138

This work was supported by the Foundation for Fundamental Research on Matter ("Fundamenteel Onderzoek der Materie")

Chapter 5 has been reprinted with permission from Phys. Fluids **29** (5), 1725-1730 (1986).

1. GENERAL INTRODUCTION

This thesis deals with the fundamental aspects of two different plasmas applied in technological processes. The first one is the cesium seeded argon plasma in a closed cycle Magnetohydrodynamic (MHD) generator, the second is the thermal argon plasma in a cascade arc with an imposed flow.

Knowledge about the plasma state is very important in the design and the utilization of installations in which a plasma is the active medium. The assumption that the plasma is in local thermal equilibrium can often be used as a first approximation. Several effects leading to a deviation from equilibrium can however occur. This may be displayed by the presence of inhomogeneities in a plasma. For instance, highly conducting arcs with a diameter of a few centimetres and with substructures in the submillimetre range were observed in an MHD generator (HEL80,SEN82,WET84). The understanding of the mechanisms causing this kind of plasma behaviour can lead to an improvement of the efficiency of an MHD generator.

It is known that a thermal argon plasma in a cascade arc without flow is close to equilibrium (ROS81,TIM85). The flow of similar plasmas is essential in many applications. A cascade arc with flow is applied in, for example, the deposition of carbon layers (KRO85). The flow may influence the deviation from equilibrium and hence the properties of the plasma. A cascade arc is a reliable apparatus to investigate the properties of an atmospheric plasma with flow.

In Chapter 2 the influence of non-equilibrium on the mass and energy balances of a plasma is worked out. The general theory presented there can be applied to both the plasma in an MHD generator and to the cascade arc with imposed flow. Introductions to these plasmas are given in the Chapters 3 and 6 respectively. These chapters are both followed by two chapters which treat the theoretical and the experimental investigations. The results are summarized in Chapter 9.

2. BASIC EQUATIONS

2.1 Introduction

The characterization of the plasma state depends on the equilibrium model which is applicable to the plasma under consideration. Because of transport and partial radiation escape, laboratory plasmas are not in complete thermodynamic equilibrium. For many applications local thermal equilibrium (LTE) is a useful model to determine the plasma parameters. The next model in the equilibrium hierarchy, the partial local thermal equilibrium (PLTE) is employed to describe plasmas not far from LTE (CIL75,GRI64). For larger deviations from equilibrium an electron saturation balance (ESB) or a corona model has to be used (MUL86). Which of these models has to be considered depends on the processes that govern the population of the levels in the neutral or ion system under consideration. In particular the magnitude of the deviation from the equilibrium (Saha) population of the ground level and of the excited levels is important. The description of the population of the levels used in this chapter is applicable to all models mentioned above, provided the electrons have a Maxwellian distribution function. A method to determine the deviation from equilibrium is given. Numerical evaluation has to show which model is appropriate. This is done in the Chapters 4 and 7 for the MHD generator plasma and the plasma in an atmospheric argon arc respectively.

Deviation from equilibrium also causes extra terms in the mass and energy balances of the different particles in the plasma. These balances, together with the momentum balance, are derived in the next section. They describe the space and time dependencies of macroscopic properties such as densities, velocities, and temperatures of each species of particles. The non-equilibrium model and the source terms are given in Sec. 2.3 and the transport quantities needed in the balance equations in Sec. 2.4. All this will be combined in Sec. 2.5. This chapter ends with some remarks about the set of independent variables in a non-equilibrium plasma and the possible choices for such a set.

2.2 Mass, momentum, and energy balance

The low temperature plasmas considered in this work consist of neutrals, singly ionized ions and electrons, for which respectively the indices *I*, *II* and *e* will be used. The mass balance (continuity equation) for particles of a species labelled α is given by:

$$\left[\frac{\partial n_\alpha}{\partial t}\right] + \nabla\cdot(n_\alpha \mathbf{w}_\alpha) = \left[\frac{\partial n_\alpha}{\partial t}\right]_{CR} \qquad (2.1)$$

where n_α is the density of the particles and $\mathbf{w}_\alpha$ the drift velocity of the particles. The terms in the left-hand side of Eq. (2.1) are the time derivative of the density and the divergence of the particle flux respectively. The right-hand side of this equation gives the gain or loss of particles of species α per unit volume and unit time caused by collisional (C) and radiative (*R*) processes. For the three species mentioned above the following relation is valid:

$$\left[\frac{\partial n_I}{\partial t}\right]_{CR} = -\left[\frac{\partial n_{II}}{\partial t}\right]_{CR} = -\left[\frac{\partial n_e}{\partial t}\right]_{CR} \qquad (2.2)$$

This follows from the ionization and recombination reactions involved:

$$X_I + e \rightleftharpoons X_{II} + 2e \qquad (collisional) \qquad (2.3a)$$

and

$$X_I + h\upsilon \rightleftharpoons X_{II} + e \qquad (radiative) \qquad (2.3b)$$

Here *X* is an arbitrary atom or molecule, *e* is an electron, and $h\upsilon$ a photon. In these reactions the neutral X_I can be a ground state or excited neutral. The net source term in the mass balance of the neutral system is the sum of the net source terms of all levels:

$$\left[\frac{\partial n_I}{\partial t}\right]_{CR} = \sum_q \left[\frac{\partial n_q}{\partial t}\right]_{CR} \qquad (2.4)$$

in which *q* indicates a ground state or an excited state of the neutral. The source term for each neutral level depends on the populations of all excited levels. Therefore the total neutral system has to be considered to get the net ionization-recombination rate. This has been done for helium, neon, argon and krypton (UHL70,UHL74), in which helium has received by far the greatest attention. In helium the major cause of deviation from equilibrium, inward diffusion, is very pro-

nounced. Also for hydrogen extensive studies have been performed (DRA73A,DRA73B). Recently Timmermans et al. published such a study for argon (TIM85) and their method, in which they use the overpopulation of excited levels to describe the neutral system, will be used here (see Sec. 2.3).

The momentum balance for particles of species a is given by

$$n_a m_a \left[\frac{\partial \mathbf{w}_a}{\partial t} + (\mathbf{w}_a \cdot \nabla)\mathbf{w}_a\right] + \nabla p_a + \nabla \cdot \mathbf{\Pi}_a - q_a n_a (\mathbf{E} + \mathbf{w}_a \times \mathbf{B}) = \mathbf{M}_a \qquad (2.5)$$

in which m_a is the mass of a particle, p_a the pressure of the species, $\mathbf{\Pi}_a$ the viscosity tensor, q_a the electric charge of the particles a, and E and B are the electric and magnetic fields. $\mathbf{M}_a$ represents the momentum exchange by collisions of particles of species a with particles of other species. The terms in the left-hand side of Eq. (2.5) give the inertia, the pressure gradient, the viscosity and the forces exerted by the electric and magnetic fields, respectively.

The last equation we need is the energy balance:

$$\frac{\partial}{\partial t}\left[\frac{3}{2} n_a k T_a\right] + \nabla \cdot \left[\frac{3}{2} n_a k T_a \mathbf{w}_a\right] + n_a k T_a \nabla \cdot \mathbf{w}_a$$

$$+ \nabla \cdot \mathbf{q}_a + \mathbf{\Pi}_a : \nabla \mathbf{w}_a = Q_a \qquad (2.6)$$

In this equation T_a is the temperature of species a, $\mathbf{q}_a$ the heat flux carried by species a and Q_a is the gain or loss of energy from particles of species a caused by interactions with particles of other species.

First the different terms in the basic equations will be discussed (Secs. 2.3 and 2.4). Later on they will be reformulated in the most suitable form for further investigations.

2.3 Source terms

2.3.1 *Collisional radiative model*

First we will consider the particle balance equation for level q. For the labeling of the levels the convention $1 \leq p \leq q \leq r \leq N$ will be used (Fig. 2.1). The symbol N identifies the maximum level which has to be taken into account and p and r are the symbols of levels to

be summed up. The net source term of the particle balance for level q is

$$\left[\frac{\partial n_q}{\partial t}\right]_{CR} = n_e \Bigg[\underbrace{\sum_{p=1}^{q-1} (n_p k_{pq} - n_q k_{pq})}_{\text{(de-)exc. (lower lying levels)}} - \underbrace{\sum_{r=q+1}^{N} (n_q k_{qr} - n_r k_{rq})}_{\text{(de-)exc. (higher lying levels)}} - \underbrace{n_q k_{q+}}_{\text{collisional ionization}} + \underbrace{n_e n_{II} k^{(3)}_{+q}}_{\text{collisional recombination}} \Bigg] + \underbrace{n_e n_{II} k^{(2)}_{+q} \Lambda_{+q}}_{\text{radiative recombination}}$$

$$- \underbrace{\sum_{p=1}^{q-1} n_q A_{qp} \Lambda_{qp}}_{\text{spont. emission}} + \underbrace{\sum_{r=q+1}^{N} n_r A_{rq} \Lambda_{rq}}_{\text{cascade radiation}} \qquad (2.7)$$

In Table 2.1 the used symbols are explained. In Eq. (2.7) the collisional processes and their reverse processes are put together. Radiation absorption, which is the reverse process of radiation emission, is treated by escape factors. This is a local approximation in which the escape factor is the ratio between the radiation escaping from a certain volume and the radiation emitted in that volume.

By application of detailed balancing Eq. (2.7) can be simplified. The principle of detailed balancing states that under conditions of thermodynamic equilibrium the differential reactions rates for each microscopic process and for the corresponding inverse process are

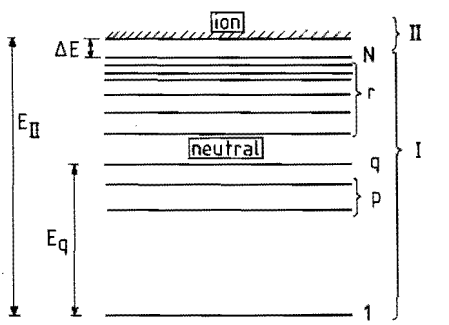

FIG. 2.1. Schematic representation of the distribution of excited levels in the energy spectrum with the notation used in this work (level 1 is the ground level).

TABLE 2.1. Symbols used in Eq. (2.7)

n_e	: electron density (m^{-3})
n_p	: population density of level p (m^{-3})
n_I	: total neutral density (m^{-3})
n_{II}	: ion ground level density (m^{-3})
k_{pq}	: electron (de-)excitation rate coefficient from level p to level q ($m^{-3}s^{-1}$)
$k^{(3)}_{q+}$	: electron ionization rate coefficient from level q (m^3s^{-1})
$k^{(2)}_{+q}$	: collisional recombination rate coefficient to level q (m^6s^{-1})
k_{+q}	: radiative recombination rate coefficient to level q (m^3s^{-1})
A_{+q}	: escape factor for radiative recombination to level q (-)
A_{qp}	: transition probability for line emission from level q to level p (s^{-1})
Λ_{qp}	: escape factor for line radiation from level q to level p (-)

equal. In general, detailed balancing applies only to the relationship between cross sections, such as that for the excitation from one level to another and that for the reverse process of de-excitation. If however the electron distribution function is Maxwellian the macroscopic reaction rates for opposite processes are also interrelated. The use of these relations, which also hold when a plasma is not in thermodynamic equilibrium, is called the method of detailed balancing (MIT73). This method can also be applied for a plasma with different electron and heavy particle temperatures. Because of the large mass ratio between electrons and heavy particles only the electron temperature determines the rate coefficients. For the processes of excitation and de-excitation and that of collisional ionization and recombination the relations between the rate coefficients are given by

$$n_e n_{q,s} k_{qp} = n_e n_{p,s} k_{pq} \tag{2.8a}$$

and

$$n_e n_{q,s} k_{q+} = n_e^2 n_{II} k^{(3)}_{+q} \tag{2.8b}$$

The Saha density $n_{q,s}$ is given by the Saha expression

$$S_{q+}(T_e) = \frac{n_e n_{II}}{n_{q,s}} = \frac{2g_{II}}{g_q}\left[\frac{2\pi m_e kT_e}{h^2}\right]^{1.5} \exp\left[\frac{-(E_{II} - E_q - \Delta E)}{kT_e}\right] \tag{2.9}$$

with

g_{II} : statistical weight of the ion ground level,

g_q : statistical weight of the excited level q,

E_q : the energy of level q,

E_{II} : the energy of the ion ground level,

ΔE : the reduction of the ionization energy (GRI63,DRA65).

The ratio of the Saha-densities of two excited levels yields the corresponding Boltzmann expression as follows

$$B_{rq} = \frac{n_{r,s}}{n_{q,s}} = \frac{g_r}{g_q} \exp\left[-\frac{E_r - E_q}{kT_e}\right] = \frac{S_{q+}}{S_{r+}} \tag{2.10}$$

Note that, except for the reduction of the ionization energy, S_{q+} and B_{rq} are only functions of the electron temperature.

A second way to simplify Eq. (2.7) is to write the densities of the levels with respect to the corresponding Saha-density. The reduced density b_q of level q and the related relative deviation δb_q will be used. These are defined by the following relations

$$b_q := \frac{n_q}{n_{q,s}} \tag{2.11a}$$

and $$\delta b_q := b_q - 1 \tag{2.11b}$$

Dividing the terms in Eq. (2.7) by $n_{q,s}$ and using the above defined quantities one gets

$$\frac{1}{n_{q,s}}\left[\frac{\partial n_q}{\partial t}\right]_{CR} = n_e\left[\sum_{p=1}^{N}(\delta b_p - \delta b_q)k_{qp} - k_{q+}^{(3)}\delta b_q\right] + S_{q+}k_{+q}^{(2)}A_{+q}$$

$$-\sum_{p=1}^{q-1}(1 + \delta b_q)A_{qp}A_{qp} + \sum_{r=q+1}^{N}(1 + \delta b_r)B_{rq}A_{rq}A_{rq} \tag{2.12}$$

Note that Eq. (2.12) is the right-hand side of Eq. (2.1) divided by $n_{q,s}$. To calculate the population of the excited levels, it will be assumed that these populations are mainly determined by collisional and radiative processes. For a stationary case and neglecting the transport term the left-hand side of Eq. (2.1) is equal to zero. The ground level will be treated separately because the transport term is not negligible.

So far the word "level" is used to denote a degenerate set of

indistinguishable quantum states of identical energy. In practice the balance equations are often applied to groups of such levels of nearly the same energy. Such a group will be called an effective level. The grouping of levels is justified because of the strong collisional coupling between the levels in a group. Consequently an effective energy level scheme and the effective degeneracies will be used. The balance equations mentioned above are still applicable except that the labelling now refers to the effective levels and not to the separate levels. Also effective rate coefficients, transition probabilities and escape factors have to be used. For reasons of simplicity the word effective often will be omitted in the following.

For a numericial evaluation of the balance equations the rate coefficients, transition probabilities, and escape factors have to be known. Besides that one needs to know the total heavy particle density $n_X = n_I + n_{II}$ of the atomic system X under consideration. The three remaining unknown variables are the electron temperature, the electron density, and the deviation from equilibrium. These variables are related to each other. By neglecting the difference between the partition function of the neutrals and the degeneracy of the neutral ground level and by assuming quasi-neutrality one gets

$$n_X = n_I + n_{II} \approx n_1 + n_e \tag{2.13}$$

In this equation n_1 is the density of the ground level only whereas n_I is the density of ground and excited levels. With the definitions of Eqs. (2.9) and (2.11) one arrives at

$$n_X = \frac{n_e^2}{S_{1+}} (1 + \delta b_1) + n_e \tag{2.14}$$

Solving this quadratic equation in the electron density gives

$$n_e = \frac{2n_X}{\sqrt{1 + 4n_X(1 + \delta b_1)/S_{1+}} + 1} \tag{2.15}$$

For $\delta b_q = 0$ one gets the LTE value of the electron density

$$n_{e,LTE} = \frac{2n_X}{\sqrt{1 + 4n_X/S_{1+}} + 1} \tag{2.16}$$

When δb_1 is small enough in first order the expansion leads to

$$n_e \approx n_{e,LTE}\left[1 - \frac{1}{2}\left[1 - \frac{1}{\sqrt{1 + 4n_X/S_{1+}}}\right]\delta b_1\right] \tag{2.17}$$

This expansion is valid for

$$\delta b_1 \ll 1 + S_{1+}/(4n_X) \tag{2.18}$$

In evaluating the balance equations at a given value of the electron temperature in many cases the LTE value for the electron density can be used.

Equation (2.12) represents $N - 1$ (only excited levels) or N (ground level included) balance equations which have to be solved simultaneously. Note that N is the number of the highest level that has to be taken into account. In principle the number of levels from the ground level to the ion level is infinite. In a plasma however one has to consider only the levels with an energy interval with the ion ground level larger than the lowering of the ionization energy. This number still can be very large (a few hundred). A way to reduce the number of equations to be solved is to assume δb_q to be zero for all q larger than a certain number M. Then an M-level model is solved because M neutral levels are involved. With the calculated overpopulations of the excited levels the net ionization rate can be calculated. The results of the calculations, for different numbers of levels taken into account, have to show whether enough levels have been used in the calculation.

In solving the balance equations one can choose for two possibilities. The first method is to solve the set of $N - 1$ equations of Eq. (2.12) for the excited levels taking the ground level separately. For a fixed electron temperature, electron density, and total heavy particle density, the independent variables are the deviation from equilibrium of the ground state (δb_1) and the escape factors. This will be done in the next subsection. One then gets information about the net ionization rate. The second method is to take the ground level into account also. The transport term in the balance equation for the ground level ($\nabla\cdot(n_1\mathbf{w}_1)$) and the escape factors then are the independent variables. In a stationary case $\nabla\cdot(n_1\mathbf{w}_1) = -\nabla\cdot(n_e\mathbf{w}_e)$ and one solves in fact the mass balance equation for the electrons. For an argon-cesium plasma as occurs in an MHD generator this equation is solved in Sec. 4.2.

2.3.2 *Source terms in the mass balance*

To evaluate the source terms in the mass balance we use Eq. (2.1). The left-hand side is assumed to be negligible for excited levels (see previous subsection). So Eq. (2.12) can be used with the left-hand side set equal to zero. For all excited levels Eq. (2.12) is multiplied with $n_{q,s}$ and summed. The resulting equation reads

$$n_e \sum_{q=2}^{N} (n_{q,s} k_{q+} \delta b_q) - n_e n_{II} \sum_{q=2}^{N} k_{+q}^{(2)} \Lambda_{+q}$$

$$= n_e n_{1,s} \left[\sum_{q=2}^{N} k_{1q} \right] \delta b_1 - n_e n_{1,s} \sum_{q=2}^{N} (k_{1q} \delta b_q)$$

$$- \sum_{q=2}^{N} (n_{q,s} b_q A_{q1} \Lambda_{q1}) \qquad (2.19)$$

Now the terms $n_e n_{1,s} k_{1+} \delta b_1$ and $-n_e n_{II} k_{+1}^{(2)} \Lambda_{+1}$ are added to both the left-hand and the right-hand side of Eq. (2.19). These terms describe the direct collisional and radiative transitions from the ground level to the ion level and vice versa. One gets

$$n_e \sum_{q=1}^{N} (n_{q,s} k_{q+} \delta b_q) - n_e n_{II} \sum_{q=1}^{N} k_{+q}^{(2)} \Lambda_{+q}$$

$$= n_e n_{1,s} K_1 \delta b_1 - n_e n_{1,s} \sum_{q=2}^{N} (k_{1q} \delta b_q)$$

$$- n_e n_{II} k_{+1}^{(2)} \Lambda_{+1} - \sum_{q=2}^{N} (n_{q,s} b_q A_{q1} \Lambda_{q1}) \qquad (2.20)$$

The total collisional rate coefficient for the ground level is defined by

$$K_1 = \sum_{q=1}^{N} k_{1q} + k_{1+} \qquad (2.21)$$

The first term in the left-hand side of Eq. (2.20) describes the direct collisional ionization due to the overpopulation of the neutral levels. The second term describes the loss of ions by radiative recombination. In the derivation of Eq. (2.20) all processes in which the ion level is involved are taken into account. They are put

together in the left-hand side which is thus equal to $+(\partial n_{II}/\partial t)_{CR}$. The first term in the right-hand side describes the loss of ground level neutrals and the others the gain by de-excitation, radiative recombination, and resonance radiation respectively. These four terms describe the net loss of ground level neutrals and their sum is equal to $-(\partial n_1/\partial t)_{CR}$. According to Eq. (2.2) this can also be written as $-(\partial n_I/\partial t)_{CR}$. As source term in the mass balance both the left-hand side and the right-hand side of Eq. (2.20) can be used. In both cases one needs to know the overpopulation of all excited levels.

The expression for $(\partial n_I/\partial t)_{CR}$ however can easily be simplified for many plasmas. To this end the excitation and de-excitation terms in the right-hand side of Eq. (2.20) are rewritten:

$$n_e n_{1,s} K_1 \delta b_1 - n_e n_{1,s} \sum_{q=2}^{N} (k_{1q} \delta b_q)$$

$$= n_e n_{1,s} \left[\sum_{q=2}^{N} (k_{1q} \delta b_1) + k_{1+} \delta b_1 - \sum_{q=2}^{N} (k_{1q} \delta b_q) \right]$$

$$= n_e n_{1,s} \left[\sum_{q=2}^{N} k_{1q} (\delta b_1 - \delta b_q) + k_{1+} \delta b_1 \right] \qquad (2.22)$$

Note we used $k_{11} = 0$ here. The de-excitation can be neglected in comparison with the excitation when $\delta b_q \ll \delta b_1$. This is e.g. the case is an atmospheric argon plasma (TIM85). Because δb_q in general decreases for larger values of q, this will be the case for $q > M$ in which M is a number that has to be determined for the system under consideration. M is the same number as discussed in Subsec. 2.3.1. Note that the summation in the excitation term (K_1) still goes to N though only M levels are taken into account for the calculation of the overpopulations.

In a similar way the term for the resonance radiation can be simplified. Splitting it in equilibrium and non-equilibrium contributions one gets

$$\sum_{q=2}^{N} (n_{q,s} b_q A_{q1} \Lambda_{q1}) = \sum_{q=2}^{N} \left[n_{q,s} (1 + \delta b_q) A_{q1} \Lambda_{q1} \right]$$

$$\approx \sum_{q=2}^{N} (n_{q,s} A_{q1} \Lambda_{q1}) + \sum_{q=2}^{L} (n_{q,s} \delta b_q A_{q1} \Lambda_{q1}) \qquad (2.23)$$

Here L is determined by the condition $\delta b_q \ll 1$ for all $q > L$. This is the same kind of upper limit for the non-equilibrium part of the resonance radiation as M is for the collisional processes. Remember however that M is determined by the condition $\delta b_q \ll \delta b_1$ for all $q > M$. Depending on the value of δb_1 being less than, equal to or greater than 1, L is less than, equal to or greater than M. For $\delta b_1 < 1$, L can be taken equal to M for simplicity. The equilibrium part of the resonance radiation can be estimated by scaling laws for $n_{q,s}$, A_{q1}, and δb_q (MUL86). The net source term for the electrons will be given by

$$\left[\frac{\partial n_e}{\partial t}\right]_{CR} = \left[\frac{\partial n_{II}}{\partial t}\right]_{CR} = n_e n_{1,s} K_1 \delta b_1 - n_e n_{1,s} \sum_{q=2}^{M} (k_{1q} \delta b_q)$$

$$- n_e n_{II} k_{+1}^{(2)} \Lambda_{+1} - \sum_{q=2}^{N} (n_{q,s} A_{q1} \Lambda_{q1})$$

$$- \sum_{q=2}^{L} (n_{q,s} \delta b_q A_{q1} \Lambda_{q1}) \qquad (2.24)$$

In plasmas close to equilibrium M and L can even be equal to 1 and the second and fifth term in the right-hand side of Eq. (2.24) disappear.

To solve the balance equations we use Eq. (2.12) assuming $(\partial n_q/\partial t)_{CR} = 0$ for the excited levels (see above)

$$n_e \left[\sum_{p=1}^{N} (\delta b_p - \delta b_q) k_{qp} - k_{q+} \delta b_q \right] + S_{q+} k_{+q}^{(2)} \Lambda_{+q}$$

$$- \sum_{p=1}^{q-1} \left[(1 + \delta b_q) A_{qp} \Lambda_{qp} \right] + \sum_{r=q+1}^{N} (1 + \delta b_r) B_{rq} A_{rq} \Lambda_{rq} = 0 \qquad (2.25)$$

To make the influence of n_e and δb_1 clear, these equations will be rewritten. The terms with δb_q, $(q \geq 2)$ will stay in the left-hand side of the equation, all other terms are transferred to the right-hand side. Moreover the terms containing n_e will be separated. One gets

$$\left\{ - \left[\sum_{p=1}^{N} (k_{qp}) + k_{q+} \right] \delta b_q + \sum_{p=2}^{N} (k_{qp} \delta b_p) \right\} n_e - \left[\sum_{p=1}^{q-1} (A_{qp} \Lambda_{qp}) \right] \delta b_q$$

$$+ \sum_{r=q+1}^{N} (B_{rq} A_{rq} \Lambda_{rq} \delta b_r) = - k_q n_e \delta b_1 - S_{q+} k_{+q}^{(2)} \Lambda_{+q}$$

$$+ \sum_{p=1}^{q-1} (A_{qp} \Lambda_{qp}) - \sum_{r=q+1}^{N} (B_{rq} A_{rq} \Lambda_{rq}) \qquad (2.26a)$$

Equation (2.26a) represents $(N - 1)$ linear equations in δb_q with $2 \leq q \leq N$. The equivalent matrix notation of Eq. (2.26a) will be given in Eq. (2.26b). For that purpose the following definitions will be used:

a) the total rate coefficient for collisions of level q which can be compared with the total rate coefficient for collisions of level 1, given by Eq. (2.21):

$$K_q := \sum_{p=1}^{N} k_{qp} + k_{q+} \tag{2.27a}$$

b) the total effective transition probability of level q (in which "effective" denotes that the escape factors are taken into account):

$$A_q := \sum_{p=1}^{q-1} (A_{qp}\Lambda_{qp}) \tag{2.27b}$$

c) the effective transition probability for radiative transitions from level p to level q multiplied by the Boltzmann expression concerning these levels:

$$\alpha_{qp} := B_{pq}A_{pq}\Lambda_{pq} = \frac{n_{p,s}A_{pq}\Lambda_{pq}}{n_{q,s}} \qquad \text{for} \quad p > q$$

$$\text{and} \quad \alpha_{qp} := 0 \qquad \text{for} \quad p \leq q \tag{2.27c}$$

By defining α_{qp} also for $q \leq p$ the summation in the last terms of both the left-hand and right-hand side of Eq. (2.26a) can be extended downwards to 2. All this leads to the following reformulation of Eq. (2.26a):

$$\sum_{p=2}^{N} \left[(-\delta_{qp}K_p + k_{qp})n_e + (-\delta_{qp}A_p + \alpha_{qp})\right]\delta b_p$$

$$= -k_{q1}n_e\delta b_1 - S_{q+}k^{(2)}_{+q}\Lambda_{+q} - \left[-A_q + \sum_{p=2}^{N}\alpha_{qp}\right] \tag{2.26b}$$

In this equation δ_{qp} denotes the Kronecker delta function. Note that in the left-hand side the collisional and radiative terms concerning the non-equilibrium part of the populations of the levels p and q are present. The right-hand side gives the contributions of the ground

level population, the ion level population and the equilibrium part of the populations of the levels p and q successively. Eq. (2.26b) has the form

$$\sum_{p=2}^{N} (Y_{qp} \delta b_p) = Z_q$$

and can be written as

$$\mathbf{Y} \cdot \delta \mathbf{b} = \mathbf{Z}$$

Here δb is a vector with the elements δb_2, δb_3, ... , δb_N. The matrix **Y** and the vector **Z** consist of a collisional (C) and a radiative (R) part and can be split into

$$\mathbf{Y} = \mathbf{YC}\, n_e + \mathbf{YR}$$

and

$$\mathbf{Z} = \mathbf{ZC}\, n_e \delta b_1 + \mathbf{ZR}$$

So

$$(\mathbf{YC}\, n_e + \mathbf{YR}) \cdot \delta \mathbf{b} = \mathbf{ZC}\, n_e \delta b_1 + \mathbf{ZR}$$

Neither these matrices nor these vectors are functions of n_e and δb_1, but only of T_e. For a given value of the electron temperature and if the electron density can be approximated by its LTE value, the solutions of Eq. (2.26) can be written as

$$\delta b_q = r_q \delta b_1 + \rho_q \qquad q = 2, 3, \ldots, N \qquad (2.28)$$

Here r_q and ρ_q are constants and ρ_q is the solution of Eq. (2.26) for $\delta b_1 = 0$. Because of the linear dependency, δb_q can be evaluated easily for different values of δb_1. Also the influence of de-excitation and the non-equilibrium part of the resonance radiation then can be evaluated.

As an example the results of the model described above applied to atmospheric argon plasmas by Rosado and Timmermans will be given (ROS81,TIM84,TIM85). Five levels are taken into account namely the 3s ground level and the excited 4s, 4p, 5s, and 3d levels. The 5s and 3d levels were combined to one effective level because of the small difference in excitation energy. So the model uses the ground level and three effective excited levels. By assuming the fourth level to be in equilibrium ($\delta b_4 = 0$), the solution of Eq. (2.26) gives relations for δb_2 (4s level) and δb_3 (4p level). For an argon plasma of 1 eV one gets

$$\delta b_2 \approx 10^{-3}\ \delta b_1 + \frac{10^{19}}{n_e} \qquad (2.29a)$$

$$\delta b_3 \approx 10^{-3}\ \delta b_1 - \frac{5 \times 10^{19}}{n_e} \qquad (2.29b)$$

In the parameter range of interest ($5 \times 10^{21}\ m^{-3} < n_e < 5 \times 10^{22}\ m^{-3}$), δb_2 will be positive but smaller than one per cent of δb_1. For level 3 there is a competition between overpopulation due to collissional excitation from the ground level and underpopulation due to the strong radiative decay to level 2. The absolute value of δb_3 is of the order of one per cent of δb_1. These results show that the net source term for the electrons given by Eq. (2.24) can be rigorously simplified in the case considered here. Both the de-excitation from excited levels and the non-equilibrium part of the resonance radiation can be neglected ($M = L = 1$).

2.3.3 *Source terms in the energy balance*

In this subsection the energy losses of electrons for the processes described above will be discussed. These processes are the following:

a) collisional (de-)excitation, collisional ionization, and collisional (three particle) recombination,

b) radiative recombination and photoionization,

c) line emission and the capture of line emission.

The energy loss caused by

d) free-free transitions (continuum emission)

will also be discussed. In the last process an electron collides with a neutral or an ion without changing the state of the neutral or the ion. The electron looses energy by emission of a photon.

a) Different inelastic processes can occur in a collision between an electron and a neutral or an ion, namely excitation, de-excitation, ionization and (three particle) recombination. In all these cases the potential energy of the heavy particle involved changes. Because the recoil energy can be neglected ($m_e \ll m_I, m_{II}$) the kinetic energy of the heavy particle is nearly unchanged. The difference in potential energy is in the case of excitation or de-excitation provided by the colliding electron whereas in the case of de-excitation or recombination it is transferred to the electron that is involved. Therefore the

energy loss of the electron is $\pm E_{qr}$ for excitation or de-excitation between the levels q and r. For ionization or recombination from or to level q it is $\pm E_{qII}$ with $E_{qII} = E_{II} - \Delta E - E_q$. The total energy loss for the electrons summed over all collisional transitions is given by

$$Q^e_{inel} = - n_e \sum_{q=1}^{N-1} \sum_{r=q+1}^{N} \left[(n_q k_{qr} - n_r k_{rq}) E_{qr} \right]$$

$$- n_e \sum_{q=1}^{N} \left[(n_q k_{q+} - n_e n_{II} k^{(3)}_{+q}) E_{q+} \right] \qquad (2.30)$$

As in the previous subsection this equation can be simplified by the method of detailed balancing and the use of the overpopulation of the levels instead of the absolute densities. This leads to

$$Q^e_{inel} = - n_e \sum_{q=1}^{N-1} \sum_{r=q+1}^{N} \left[n_{q,s} k_{qr} (\delta b_q - \delta b_r) E_{qr} \right]$$

$$- n_e \sum_{q=1}^{N} (n_{q,s} k_{q+} \delta b_q E_{q+}) \qquad (2.31)$$

In the previous subsection it is derived that δb_q can be assumed to be equal to zero for all q greater than a certain number M. So the summation over q can be stopped at M. In the summation over r this is only partially possible: though the de-excitation term from the upper level can be neglected for $r > M$, the excitation to these levels has to be taken into account. Rewriting Eq. (2.31) gives

$$Q^e_{inel} = - n_e \sum_{q=1}^{M} \left[n_{q,s} \delta b_q K_q \langle E_q \rangle - \sum_{r=q+1}^{M} (n_{q,s} k_{qr} \delta b_r E_{qr}) \right.$$

$$\left. - \sum_{r=1}^{q} (n_{q,s} k_{qr} \delta b_q E_{qr}) \right] \qquad (2.32)$$

where

$$\langle E \rangle = \frac{\sum_{r=1}^{N} (k_{qr} E_{qr}) + k_{q+} E_{q+}}{K_q} \qquad (2.33)$$

represents the total mean excitation energy of level q. For a plasma with only the ground level out of equilibrium ($M = 1$) Eq. (2.32) reduces to

$$Q^e_{inel} = - n_e n_{1,s} K_1 \delta b_1 \langle E_1 \rangle \tag{2.34}$$

This is the case for the argon plasma at 1 eV evaluated at the end of Subsec. 2.3.2 (see also TIM85).

b) In the process of radiative recombination an electron collides with an ion forming a neutral under emission of a photon. The recoil energy is again negligible. The kinetic energy of the created neutral equals that of the original ion. The energy loss of the electrons is caused by the disappearance of thermal electrons with a mean energy of $(3/2)kT_e$. The energy of the emitted photon equals the sum of the electron energy and the difference between the potential energy of the ion and the neutral. Radiative recombination has besides the capture of free electrons also another effect. Radiative recombination to a certain level q overpopulates this level. This is compensated by collisional ionization. The energy loss of the electrons in this process equals the energy of the emitted photon namely E_{qII}. For the non-equilibrium levels this already has been accounted for in the collisional term namely by the overpopulation δb_q for $q \leq M$. For the equilibrium levels ($q > M$) one has to put E_{qII} in the term describing the energy loss due to radiative recombination. Furthermore the electrons loose an average energy of $(3/2)kT_e$ per radiative recombination.

In the reverse process of photoionization the emitted radiation is trapped by a neutral and consequently an ion and an electron are formed. As in the previous subsections the photoionization is represented by the escape factor Λ_{+q}. The energy gain for the electrons in photoionization is the same as the loss of energy involved in radiative recombination. To get the effective source term in the energy balance the terms for radiative recombination have to be multiplied by Λ_{+q}. This leads to

$$Q^e_{rad.rec} = - n_e^2 \sum_{q=1}^{M} \left[k^{(2)}_{+q} \Lambda_{+q} \frac{3}{2} kT_e \right] - n_e^2 \sum_{q=M+1}^{N} \left[k^{(2)}_{+q} \Lambda_{+q} \left[\frac{3}{2} kT_e + E_{q+} \right] \right] \tag{2.35}$$

c) Line emission and the capture of line radiation have to be treated in the same way as radiative recombination. Radiative transitions to equilibrium levels have to be distinguished from transitions

to non-equilibrium levels. The electron energy loss corresponding to non-equilibrium levels is already accounted for in the collisional term. Only the loss corresponding to equilibrium levels has to be considered here. Because only the energy of the emitted photon is involved, the equivalent of the first term in Eq. (2.35) does not exist. Again the capture of radiation is treated by an escape factor. The involvement of two levels in the process of line radiation leads to a double summation (TIM85):

$$Q^{e}_{line\ rad} = \sum_{q=M+1}^{N-1} \sum_{r=q+1}^{N} (n_{r,s} b_r A_{rq} A_{rq} E_{rq}) \tag{2.36}$$

Note that in this equation not the overpopulation but the population itself is present.

d) Free-free radiation results from collisions of electrons with ions or neutrals in which no change of the state of the heavy particles occurs. The emission coefficients for free-free radiation are given by (CAB71)

$$\varepsilon_{ei}(\upsilon) = \frac{C_1}{c} \frac{n_e}{T_e^{0.5}} \sum_{z=1}^{\infty} z^2 n_z G_z(\upsilon, T_e) \tag{2.37}$$

and

$$\varepsilon_{eo}(\upsilon) = \frac{C_2}{c} n_e T_e^{1.5} \left[\left[\frac{h\upsilon}{kT_e} + 1 \right]^2 + 1 \right] \exp\left[- \frac{h\upsilon}{kT_e} \right] \times \sum_{h} \left[n_h \sigma_h(T_e) \right] \tag{2.38}$$

with

$\varepsilon(\upsilon)$: emission coefficient in $Jm^{-3}sr^{-1}$,

c : speed of light,

z : charge number,

n_z : density of ions with charge z,

$G_z(\upsilon, T_e) = \xi_{ff,z} \exp\left[\frac{-h\upsilon}{kT_e} \right]$: gauntfactor,

$\xi_{ff,z}$: Bibermanfactor, correction for the atomic structure for non-hydrogen atoms,

n_h : density of neutral particles of species h,

σ_h : cross section for electron-neutral collisions,

$C_1 = 1.632 \times 10^{-43}$ $Wm^4sr^{-1}K^{0.5}$,

and $C_2 = 1.026 \times 10^{-34}$ $Wm^2sr^{-1}K^{-1.5}$.

For the plasmas considered in this work only the term with $z = 1$ has to be taken into account in Eq. (2.37). The energy loss of electrons due to free-free radiation caused by collisions with ions (Q_{ff}^{ei}) can be calculated by integrating $\varepsilon_{ei}(\upsilon)$ over the entire spectrum. Introducing an effective Bibermanfactor ξ_{eff} (KAR61) this results in

$$Q_{ff}^{ei} = 4\pi \int_0^\infty \varepsilon_{ei}(\upsilon)\, d\upsilon = 1.413 \times 10^{-40}\, \xi_{eff} n_e n_{II} T_e^{0.5} \quad W/m^3 \qquad (2.39)$$

For hydrogen ξ_{eff} is unity and for other elements it is close to 1. The same procedure for the part of the free-free radiation caused by collisions with neutrals gives

$$Q_{ff}^{eo} = 4\pi \int_0^\infty \varepsilon_{ei}(\upsilon)\, d\upsilon$$

$$= 1.282 \times 10^{-23}\, n_e T_e^{2.5} \times \sum_h \left[n_h \sigma_h(T_e) \right] \quad W/m^3 \qquad (2.40)$$

2.3.4 *The escape of radiation*

Part of the line radiation emitted by a plasma actually leaves the plasma volume. This is represented by the use of escape factors in the previous subsections. An escape factor is a local approximation for the non-local capture of line radiation (HOL47,HOL51). As above only line radiation emitted by neutral particles will be considered.

Also continuum radiation from radiative recombination or free-free emission is partically trapped in a plasma. These effects can also be treated by escape factors.

The escape of line radiation is determined by the shape (width and profile) of the line, the density of absorbing particles, and the geometry of the plasma. The shape of a line is generally a convolution of a number of line profiles, namely a Doppler profile, a Lorentz profile or a Holtsmark profile (GRI64,GRI74). The Doppler profile originates from the Doppler shift caused by the thermal motion of the emitting particles. When these have a Maxwellian velocity distribution the resulting line profile is represented by a Gaussian function $\exp(-x^2)$ in which x is a scaled frequency. The Lorentz profile mainly originates from line broadening by collisions of the emitting particles with other particles (pressure broadening). The second particle

involved can be an electrically charged particle (electron or ion), a like neutral particle or an unlike neutral particle. The broadening processes caused by collisions with these particles are called Stark, Resonance, and Van der Waals broadening respectively. Also natural broadening gives rise to a Lorentz profile but in the dense plasmas described in this work it is negligible. A normalized Lorentz profile is described by the function $1/(1 + x^2)$. The third line profile that may be involved is the Holtsmark profile. It arises when the impact approximation which results in Lorentz profiles is not valid in pressure broadening. In the impact approximation the time associated with the disturbance of the emitting particle is short compared with the duration of a collision. This criterion will be examined later and will prove to be valid in the plasmas under consideration. So the lines that are of interest can be described by the convolution of a Gaussian and a Lorentz profile: the Voigt profile.

The escape of line radiation with either a Gaussian or a Lorentz profile was treated first by Holstein (HOL47,HOL51). An absorption coefficient $k(\upsilon)$ proportional with the density of absorbing neutrals and with the same frequency dependency as the emmision was assumed. The probability of the radiation traversing a distance ρ in the plasma is given by the transmission coefficient

$$T(\rho,\upsilon) = \exp[-\, k(\upsilon)\rho] \tag{2.41}$$

Integration over the frequency gives the average transmission coefficient $T(\rho)$ which is a function of the optical depth $k_o\rho$. Here k_o is the absorption coefficient in the middle of the line. A numerical evaluation is necessary especially for small values of $k_o\rho$. For large values of the optical depth Holstein gives the following approximations for Gaussian and Lorentz profiles respectively:

$$T_G(\rho) \approx \frac{1}{k_o\rho\,\sqrt{\pi\,\ln(k_o\rho)}} \tag{2.42}$$

and

$$T_L(\rho) \approx \frac{1}{\sqrt{\pi\,k_o\rho}} \tag{2.43}$$

As one can see from Eqs. (2.42) and (2.43), the transmission coefficient is larger for a Lorentz profile than for a Gaussian one. This is caused by the shape of both profiles in the far wing which contributes significantly to the transmission factor.

The escape factor Λ at a certain location in the plasma is determined by the transmission coefficient in the total plasma because the capture of radiation emitted elsewhere has to be taken into account. So the escape factor is obtained by integrating the product of the emission and of the transmission coefficient over the plasma volume. Of course also the geometry of the plasma plays a role. Here only the results for a cylinder of infinite length and with radius R are given (HOL51):

$$\Lambda_G = \frac{1.60}{k_0 R \sqrt{\pi \ln(k_0 R)}} \tag{2.44}$$

$$\Lambda_L = \frac{1.125}{\sqrt{\pi} k_0 R} \tag{2.45}$$

Eqs. (2.44) and (2.45) are only valid for large values of the optical depth, in particular for large values of $k_0 R$. The escape factor has the same functional dependency of $k_0 R$ as the transmission coefficient with respect to $k_0 \rho$ except for a factor of order unity. The factor in Λ_L is 1.125 instead of 1.115 as given by Holstein (HOL51) because here a misprint was involved (IRO79).

Numerical evaluation of the escape factor for small optical depths is given by Drawin (DRA73C). For $k_0 R < 1$ the escape factor is nearly the same for both profiles. Besides that Drawin also gives the escape factor for combined Gaussian and Lorentz profiles. As a parameter one uses the ratio of the widths of the Lorentz and the Gaussian profile. The values of the escape factor for the Voigt profile are in between those for the Gauss and the Lorentz profiles. When the width of the Lorentz profile is more than three times that of the Gaussian profile the escape factor can be approximated by the escape factor of a pure Lorentz profile. This is caused by the strong influence of the far wing of the Lorentz profile on the escape factor. Because the width of the profiles depends strongly on the properties of the emitting neutral and of the plasma parameters they will be discussed later (Chapters 4 and 7).

The escape of continuum radiation can be treated in the same way as the escape of line radiation. By means of the method of detailed balancing the frequency resolved emission coefficient $k(\nu)$ can be calculated from the emissivity of continuum radiation and the spectral

intensity of a black body (CAB71). In both the MHD generator plasma (WET84) and the argon cascade arc (TIM84) the plasma is optically thin for continuum radiation.

2.4 Transport quantities

In this section expressions for the transport quantities needed in the balance equations are given. These quantities are the diffusion coefficient, the electrical conductivity, the heat conductivity, and the transfer of energy from electrons to heavy particles.

2.4.1 *Diffusion coefficients*

The transport term in the mass balance is given by $\nabla\cdot(n_e \mathbf{w}_e)$ which is equal to $\nabla\cdot(n_{II}\mathbf{w}_{II})$. When the drift velocity, $\mathbf{w}_e$, is governed by diffusion, it can be written as

$$\mathbf{w}_e = - D_a \frac{1}{n_e} \nabla n_e \tag{2.46}$$

with D_a the ambipolar diffusion coefficient

$$D_a = D_i \left[1 + \frac{T_e}{T_h} \right] \tag{2.47}$$

In this equation D_i is the diffusion coefficient for the ions and T_h is the heavy particle temperature (MIT73).

2.4.2 *Electrical conductivity*

An electric field causes a drift velocity of the charged particles. The resulting current density is given by

$$\mathbf{J} = - e n_e (\mathbf{w}_e - \mathbf{w}_{II}) \tag{2.48}$$

The electrical conductivity is defined as

$$\sigma = \frac{e^2 n_e}{m_e \sum_h \nu_{eh}} \tag{2.49}$$

in which ν_{eh} is the average momentum transfer collisional frequency for collisions of electrons with heavy particles of species h. It can be written as follows

$$\nu_{eh} = n_h Q_{eh} \bar{v}_e \tag{2.50}$$

where Q_{eh} is the average momentum transfer cross section, and

$$\bar{v}_e = \left[\frac{8kT_e}{\pi m_e}\right]^{1/2}$$

is the mean thermal speed of the electrons. Because of the small electron mass the mean electron speed is used instead of the mean relative speed. In Eq. (2.49) for the electrical conductivity the collision frequencies with all heavy particles are used separately. This expression is given by the classical collision theory. To be valid this theory requires that the number of particles in the Debye sphere is large. The Debye shielding length is given by (MIT73)

$$\lambda_D = \left[\frac{\epsilon_0 kT_e}{n_e e^2}\right]^{1/2} \tag{2.51}$$

This leads to the following number of particles in the Debye sphere:

$$n_D = n_e \lambda_D^3 \tag{2.52}$$

In the cascade arc plasma the requirement $n_D \gg 1$ is not always fulfilled especially at high pressures (TIM84). For the MHD generator plasma this will be checked (Chapter 4) and when necessary corrections will be made.

The energy gain of the electrons due to the current density and the electrical field is given by $\mathbf{J}\cdot\mathbf{E}'$ in which $\mathbf{E}'$ also includes the induced electrical field. With the generalized Ohm's law this can be rewritten to (MIT73)

$$Q_R^e = \frac{J^2}{\sigma} \tag{2.53}$$

For a plasma without induced electric field and without magnetic field $\mathbf{J} = \sigma\mathbf{E}$ and Eq. (2.53) can be rewritten to

$$Q_R^e = \sigma E^2 \tag{2.54}$$

2.4.3 *Heat conductivity*

The heat flux, the term $\nabla\cdot\mathbf{q}_\alpha$ of Eq. (2.6), can for the electrons be written as $\nabla\cdot\mathbf{q}_e = -\nabla\cdot(\lambda_e \nabla T_e)$. The heat conductivity of the electrons, given by the classical mean free path approximation (MIT73), is

$$\lambda_e = \frac{15}{\pi} \frac{k^2 T_e n_e}{m_e \left[\sum_h 2\nu_{eh} + \sqrt{2\nu_{ei}} \right]} \tag{2.55}$$

In this equation ν_{ei} is the collisional frequency of electrons with ions. Again this expression may have to be corrected for non-ideal plasmas with a small number of particles in the Debye sphere.

2.4.4 *Heat exchange between electrons and heavy particles*

The last term in the energy balance that has to be evaluated is the transfer of heat from electrons to heavy particles. Again the expression from the classical collision theory will be used. This leads to (MIT73)

$$P_{eh} = -\frac{3}{2} n_e m_e k (T_e - T_h) \sum_h \left[\frac{2\nu_{eh}}{m_h} \right] \tag{2.56}$$

2.5 Formulation of the balance equations

The terms worked out in the Secs. 2.3 and 2.4 now can be substituted in the balance equations given in Sec. 2.2. This results in the following mass balance for the electrons

$$\left[\frac{\partial n_e}{\partial t} \right] - \nabla \cdot (D_a \nabla n_e) = \left[\frac{\partial n_e}{\partial t} \right]_{CR} \tag{2.57}$$

D_a is given is given by $D_a = D_i \left[1 + \frac{T_e}{T_h} \right]$ and

$$\left[\frac{\partial n_e}{\partial t} \right]_{CR} = n_e n_{1,s} K_1 \delta b_1 - n_e n_{1,s} \sum_{q=2}^{M} (k_{1q} \delta b_q) - n_e n_{II} k_{+1}^{(2)} A_{+1}$$
$$- \sum_{q=2}^{N} (n_{q,s} A_{q1} A_{q1}) - \sum_{q=2}^{L} (n_{q,s} \delta b_q A_{q1} A_{q1})$$

(see Secs. 2.4 and 2.3 respectively).

The energy balance becomes

$$\frac{\partial}{\partial t} \left(\frac{3}{2} n_e k T_e \right) + \nabla \cdot \left(\frac{3}{2} n_e k T_e \mathbf{w}_e \right) + n_e k T_e \nabla \cdot \mathbf{w}_e = \frac{J^2}{\sigma} + Q^e_{inel} + Q^e_{rad.rec}$$
$$+ Q^e_{line\ rad} + Q^{ei}_{ff} + Q^{eo}_{ff} + P_{eh} + \nabla \cdot (\lambda_e \nabla T_e) - \Pi_e : \nabla \mathbf{w}_e \tag{2.58}$$

The time derivative of the internal energy and the convection and expansion terms are given in the left-hand side of Eq. (2.58). All other terms are put in the right-hand side. The left-hand side can be rewritten by substituting the mass balance.

2.6 Independent thermodynamic variables

In the above sections three main variables have been used: the electron temperature, the electron density, and the overpopulation of the ground level (T_e, n_e, and δb_1). A relation between these three variables was derived in Subsec. 2.3.1. When the total density of neutrals and ions ($n_X = n_I + n_{II}$) is known, when the populations of the excited levels compared to that of the ground level can be neglected ($n_I = n_1$) and when quasi-neutrality can be assumed ($n_{II} = n_e$) one can apply Eq. (2.14):

$$n_X = \frac{n_e^2}{S_{1+}} (1 + \delta b_1) + n_e$$

In this equation T_e is present through the temperature dependent Saha expression, S_{1+}. So when two of the variables T_e, n_e and δb_1 are known the third one can be calculated. The electron density was explicitly written as a function of the electron temperature and the overpopulation of the ground level in Eq. (2.15):

$$n_e = \frac{2n_X}{\sqrt{1 + 4n_X(1 + \delta b_1)/S_{1+}} + 1}$$

This equation is made visible as a plane in a three-dimensional space in Fig. 2.2. A certain state of the plasma is represented by a point on this plane. Fig. 2.2 is drawn for conditions which are typical for the argon-cesium plasma in an MHD generator. The total cesium neutral and ion density n_{Cs} replaces n_X in Eq. (2.15). It is derived from the heavy particle temperature T_h, the total pressure p and the seed fraction SF (the part of the total heavy particle density that consists of cesium).

The most commonly used set of variables is the one consisting of electron temperature and electron density. Both quantities are often directly measurable in a plasma. For a theoretical analysis it can be more convenient to use another combination. As can be seen in the

preceding sections, the electron density occurs many times directly in the balance equations and in the transport quantities. The electron temperature is mostly hidden in functions that depend exponentially on it, e.g. S_q and B_{rq}. This is also the case in Eqs. (2.14) and (2.15). The overpopulation of the ground level δb_1 occurs always linearly in the balance equations and in Eq. (2.14). So the combination of n_e and δb_1 as independent thermodynamic variables may be more convenient for a theoretical analysis. In fact this set of independent variables is used in Chapter 4.

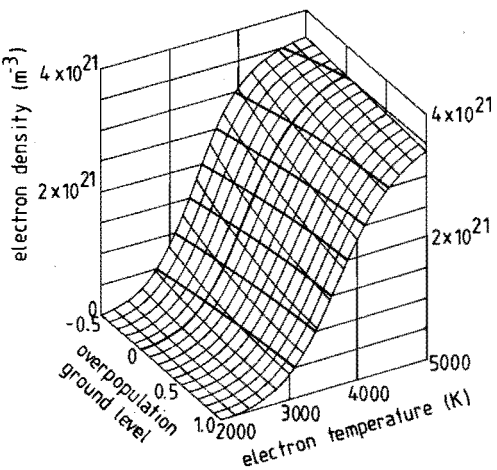

FIG. 2.2. Relation between n_e, T_e, and δb_1 for an Ar–Cs plasma with T_h = 1000 K, $p = 5 \times 10^4$ Pa, and $SF = 10^{-3}$ ($n_{Cs} = 3.62 \times 10^{21}$ m^{-3}).

3. THE PLASMA IN A CLOSED CYCLE MHD GENERATOR

3.1 Introduction

In an MHD generator heat is directly converted into electrical energy. As for every conversion process, thermodynamics gives the Carnot efficiency as the maximum attainable. It is determined by the temperature at which the heat is supplied to the conversion system and the temperature at which the heat is carried off. For a steam cycle, the conventional way of converting heat into electrical energy, these temperatures are about 800 and 300 K respectively. This gives a Carnot efficiency of 62%. In an advanced steam power plant an efficiency of 38% can be obtained. No substantial improvement is expected from further developments of the steam cycle. In an MHD generator no moving mechanical components which restrict the upper temperature are present. Therefore the permissible initial temperature is about 2000 K. On the other hand, the working medium leaving the MHD generator has a high enough temperature to serve as a heat source for the steam cycle. So the total efficiency can be increased by using an MHD topping cycle in combination with a steam cycle. Several studies have indicated that in this way an overall efficiency of 50% can be obtained (SEI76).

MHD power generation is based on the expansion of an electrically conducting fluid through a magnetic field. Due to the Lorentz force acting on the charge carriers, an induced electric field develops. When loading this field with a resistor, electrical power is supplied to the external circuit. MHD power systems can be divided in two types: open cycle and closed cycle MHD. In open cycle MHD the working fluid consists of combusted fossil fuel seeded with an alkali metal. The temperature has to be about 2700 K in order to provide for a sufficiently high conductivity. In closed cycle MHD the working fluid of a closed loop (alkali seeded Ar or He) is heated to a temperature of 1700 to 2000 K. This mixture is expanded through an MHD channel, cooled down and compressed to be used again. The medium in an open cycle MHD generator is in thermodynamical equilibrium (the electron temperature equals the gas temperature) which accounts for the high temperature needed. In a closed cycle MHD generator however the electron temperature is elevated over the gas temperature. This leads to a conductivity that is dependent on the current density. Also non-

equilibrium ionization has to be taken into account. A closed cycle MHD generator typically works at a pressure of about 0.5 bar, a flow velocity of 1000 m/s, and a magnetic induction from a few tesla up to 5 T.

The MHD research program at the Eindhoven University of Technology is engaged on closed cycle MHD conversion. Two facilities are available: the shock tube MHD generator and the blow down facility. In the shock tube generator high stagnation temperatures (up to 3500 K) during a short test time (5 ms) can be reached. In the blow down facility a stagnation temperature up to 2000 K can be generated during 10 s by means of a heat exchanger. The other operating conditions and the channel dimensions are about the same for both facilities. An enthalpic efficiency (electrical output power divided by thermal input power) of over 20% has been achieved at a stagnation temperature of 3000 K in the shock tube facility (BL075). At a stagnation temperature of 2000 K enthalpic efficiencies of 10% (VEE78) and 8.5% (BAL85) were reported in the shock tube and the blow down facility respectively. Very recently an enthalpic efficiency of 12.9% was reached with the blow down facility (BAL86).

The experiments described in this work were carried out using the shock tube facility because of the higher working cycle and the better optical accessibility. This facility will be described in the next subsection. The blow down facility is extensively described elsewhere (FLI83). Furthermore former investigations to the discharge structure and the present work will be discussed in this chapter.

3.2 Shock tube MHD facility

The experiments described in this work as far as related to MHD energy conversion have been performed with the shock tube MHD generator of the Eindhoven University of Technology. This facility is extensively described elsewhere (BL073,WET84) and here only the most important features are given. The facility works in a pulsed mode: the energy for the flow is stored in the driver section of a shock tube and the energy for the magnetic induction in a capacitor bank.

The shock tube has an inner diameter of 22.4 cm. The driver section (length 4 m) is filled with helium, the test section (length 8 m) with argon mixed with one per mille cesium. Maximum testing time is

achieved by operating the shock tube in the tailored interface mode (OER66). This is obtained by choosing a ratio of 8.95 between the driver pressure and the pressure of the test gas. With a pressure in the test section of 0.1 bar this results in a stagnation temperature of 3400 K and a stagnation pressure of 9 bar. Under these conditions the maximum attainable thermal input power of 5 MW is achieved. By changing the pressure ratio between driver gas and test gas, lower stagnation temperatures (from 1750 K upwards) and corresponding lower thermal input powers can be generated.

A hole in the end plate of the shock tube allows the plasma to flow into the generator channel (Fig 3.1). Because this aperture is less than 20% of the cross section of the shock tube, it does not influence the reflection of the incident shock substantially. This results in a testing time of 5 ms. The cross section is 2.9 × 11 cm^2 in the throat of the nozzle and changes linearly over a length of 95 cm to 12 × 11 cm^2 at the outlet of the channel (WET84). At the end of the channel a vacuum vessel is installed to ensure an undisturbed flow during the testing time.

The nozzle is designed to get a supersonic flow with a Mach number of 1.9 at the first pair of electrodes positioned 15 cm downstream of the throat. The electrodes are in the parallel walls while the insulator walls diverge. The first half of the channel is equiped with flat electrodes mounted flush with the wall. Here a large number of electrodes per unit length of channel is used to reduce current concentration on the electrode edges. The second half is equiped with

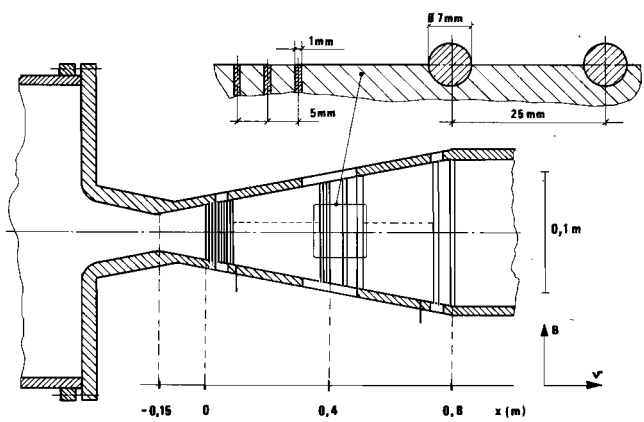

FIG. 3.1. Schematic view of linear channel.

cylindrical electrodes halfway countersunk in the wall (Fig. 3.1). Opposite pairs of electrodes are connected by a load resistance (segmented Faraday type generator). The resistance is 5 Ω per electrode in the first half of the channel and 1 Ω in the second half. This provides a constant loading per unit length.

The magnetic field is provided by an air coil magnet energized by a capacitor bank. The energy stored in the capacitor bank is 1.5 MJ. The current through the magnet oscillates with a period of 55 ms. The magnetic induction is 3.5 T in the first maximum of the current.

All this results in the following typical values for the plasma in the generator: mass flow ϕ = 3 kg/s, velocity v = 1000 m/s, pressure p = 0.1 to 1 bar, gas temperature T = 1000 K, mass density ρ = 0.3 kg/m^3, seed fraction (the part of the total heavy particle density that consists of cesium) SF = 0.1%, and maximum attainable magnetic induction B = 3.5 T.

3.3 Discharge structure of a closed cycle linear MHD generator

Due to non-equilibrium ionization the current density in a closed cycle MHD generator is not uniformly distributed (HEL80). Earlier investigations have shown that the current is concentrated in arcs, called streamers, which move with approximately the flow velocity (SEN82,BOS85). These streamers have a diameter of a few centimetres and are separated by relatively cold, non-conducting regions. The streamers are important in two ways. First they provide the electrical power and second they are important because of the exchange of momentum and energy with the gas flow.

The streamers can be visualized by fast framing photography through large windows in the insulator walls. Typical results for three different sets of operating conditions are given in Fig. 3.2. In each picture six photographs are present, made with a time interval of 1 μs. Time resolved line emmission measurements, which where performed simultaneously with the framing pictures, are shown in Fig. 3.3. Both diagnostics show that the part of the channel filled with hot plasma gets larger with increasing power extraction. Further the photographs suggest that the streamers exhibit a substructure, consisting of filaments.

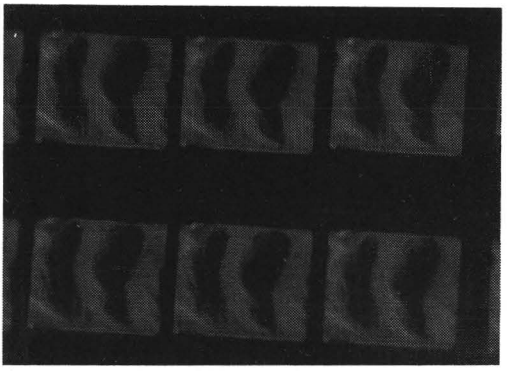

B = 2.3 T
T_s = 2400 K
η = 8.2%

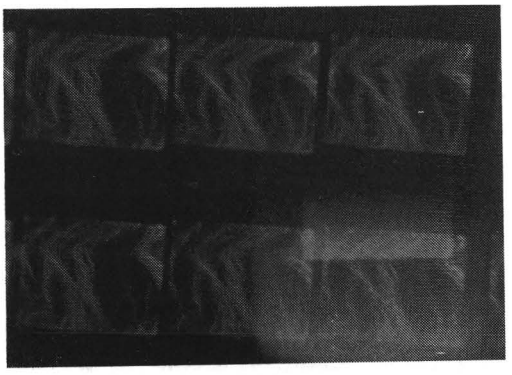

B = 3.3 T
T_s = 2680 K
η = 16.9%

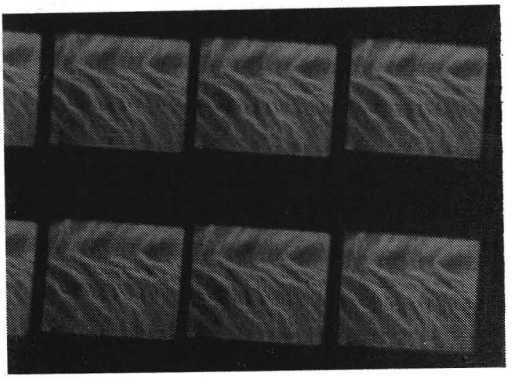

B = 3.4 T
T_s = 3250 K
η = 21.2%

FIG. 3.2. Framing picture of the discharge structure for three set of conditions corresponding to increasing power extraction levels. The flow velocity is from right to left, the magnetic induction is perpendicular to the plane of the picture (B = magnetic induction, T_s = stagnation temperature, and η = enthalpic efficiency).

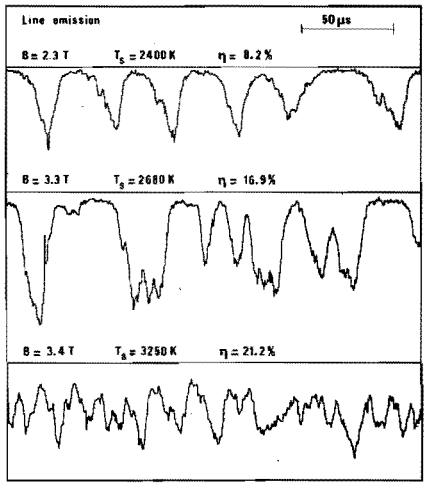

FIG. 3.3. Line emission signal for three sets of conditions corresponding to increasing power extraction levels (B = magnetic induction, T_s = stagnation temperature, and η = enthalpic efficiency).

More quantitative results are given by spectroscopic measurements of continuum emmissivity (WET83). From these measurements the electron density has been obtained spatially resolved in two dimensions. The streamers show an elliptical cross section with the long axis along the magnetic field. The spatial resolution is not sufficient to distinguish the filaments.

The above mentioned measurements lead to values in the streamer of 2.5×10^{21} m^{-3} for the electron density and 4000 to 5000 K for the electron temperature. This is well above the gas temperature. The electrical conductivity in these circumstances is about 500 A/(Vm). The current density has a value of about 10^5 A/m^2 (WET84) when evaluated taking the cross section of a streamer into account. An evaluation for a streamer consisting of filaments with a smaller effective cross section leads to the higher value of 4×10^5 A/m^2.

The observed division of the plasma in regions with high temperature and density and low temperature and density respectively has been considered theoretically in earlier work (MES82). It has been found that there are several unstable modes in such a plasma. The most dominant one is the so-called electrothermal mode. A local rise in electron temperature causes an increase in electron density. This

leads to a higher current density and again to a higher electron temperature. Depending on the conditions at which the calculation starts, the plasma can also go to a low temperature, low density situation. This theory does not give an explanation for the dimensions of the inhomogeneities.

3.4 Present work

The investigation of the characteristics of the filaments and the mechanisms associated with their existence is the main purpose of this part of the present work. Especially the deviation from equilibrium caused by transport of particles and by radiation will be considered.

An experimental determination of the dimension of a filament is necessary. This cannot be obtained with the diagnostics described in the previous subsection as the spatial resolution of these methods is larger than one millimetre. A measuring method only sensitive to electron density pertubations in the submillimetre range is needed. Scattering of CO_2 laser light with heterodyne detection has been used. This method has been applied to several plasmas for measuring the level of turbulences with specific wavelengths (SLU80, POT81, SCH83). These turbulences are mostly described in terms of waves. Instead of this, cylindrical profiles moving through the detection volume are used for the description of the electron density (see Chapter 5).

In the next chapter the mass and energy balances of the electrons for cylindrical structures with a diameter of less than one millimetre will be considered. Because of the small dimension the effects of radiaton, heat conductivity and non-equilibrium have to be taken into account. The evaluation of the combined balances leads to a value for the diameter of the filaments.

4. THEORETICAL DESCRIPTION OF A LOW TEMPERATURE AR-CS PLASMA

4.1 Introduction

In this chapter an Ar-Cs plasma as is present in a closed cycle MHD generator (see Chapter 3) is described theoretically. To this end the basic equations of Chapter 2 will be worked out.

The electron temperature ranges from 2000 to 5000 K. At these temperatures only cesium is ionized. Nevertheless the argon plays an important role in the dynamics of the plasma. The argon neutrals give rise to Van der Waals broadening of neutral cesium lines. This influences the escape factor of these lines and by that the deviation from equilibrium of the cesium system and the source term in the mass balance of the electrons and the cesium neutrals. Furthermore the argon influences the diffusion coefficient of cesium and hence the transport terms in both the mass and the energy balances of electrons and neutrals. The heat transfer of electrons to heavy particles and the argon heat conductivity play also a role in the energy balance of the plasma. The total cesium heavy particle density is obtained from the seed fraction of the Ar-Cs mixture, the total pressure and the heavy particle temperature.

The behaviour of the cesium neutral system is described by the collisional radiative model given in Subsec. 2.3.1. An effective level scheme of neutral cesium is needed. In Fig. 4.1 the ten lowest lying levels of cesium are drawn (note that the word effective is omitted from here on). In this work the non-equilibrium of at most ten levels

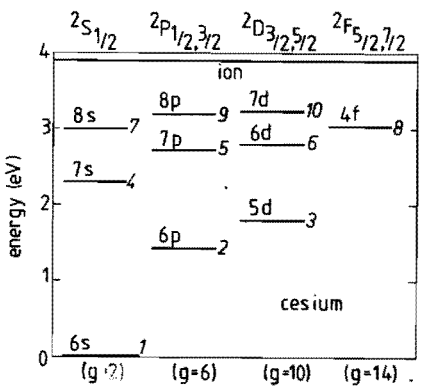

FIG. 4.1. Effective level scheme of neutral cesium. The labels which refer to an effective level as used in this work are given by italic numbers to the right of the lines denoting a level. The degeneracies of the effective levels are given at the lower side of the figure.

TABLE 4.1. Data concerning the level scheme of neutral cesium.

q	quantum state	g	E_q (eV)	effective quantum number
1	6S	2	0.00	1.87
2	6P	6	1.43	2.35
3	5D	10	1.80	2.55
4	7S	2	2.30	2.92
5	7P	6	2.71	3.39
6	6D	10	2.80	3.53
7	8S	2	3.01	3.92
8	4F	14	3.03	3.97
9	8P	6	3.19	4.40
10	7D	10	3.23	4.53
ion	--	1	3.89	--

will be considered. More detailed information about the energies and the statistical weights of these levels can be found in Table 4.1. The Saha expression $S_{q+}(T_e)$ can be calculated for a given electron temperature using these data. To give an impression of their magnitudes and their temperature dependencies, the values of the Saha expressions for the first three levels are drawn in Fig. 4.2 as a function of the

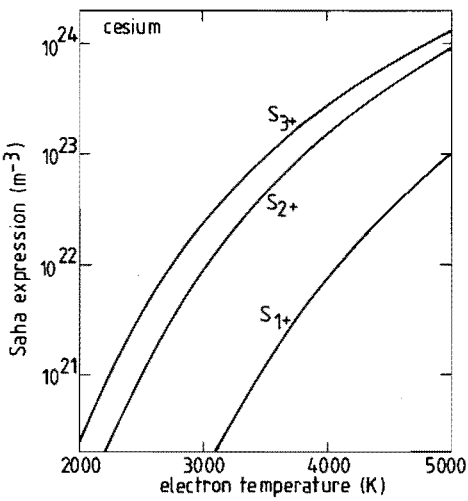

FIG. 4.2. The Saha expressions as a function of the electron temperature for the first three effective levels of neutral cesium according to Eq. (2.9) and the data of Table 4.1.

electron temperature. The Boltzmann expressions are given by the ratio of two Saha expressions according to Eq. (2.10).

For the rate coefficients for excitation and ionization by electrons the theory of Gryzinski (GRY65) has been used. The formulae of Gryzinski are derived on the basis of a semi-classical model and give the cross section for a certain loss of energy of the incoming electron. The rate coefficients for excitation are calculated by integrating the cross sections weighted with a Maxwellian distribution function for the electrons. The rate coefficient for ionization is calculated in a similar way. The integration starts at the energy of the first level which is not taken into account in the ten level scheme (E = 3.33 eV); in this scheme excitation to that level or to a higher level is formally an ionization. In this way the total rate coefficients, K_q, for collisional (de-)excitation and ionization are obtained correctly by Eq. (2.27a) with a summation until q = 10. The rate coefficients for de-excitation and collisional recombination are calculated by detailed balancing. These rate coefficients have been used before in the study of ionization relaxation processes (BOR82). Some of the rate coefficients, k_{qp}, are given in Figs. 4.3, 4.4, and 4.5 as a function of the electron temperature. Also the total rate coefficients, K_q, for collisions are given.

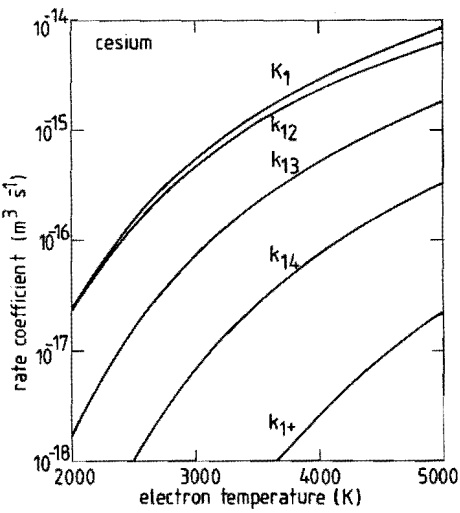

FIG. 4.3. The rate coefficients for collisional processes in which the ground level of neutral cesium is involved (according to the theory of Gryzinski) as a function of the electron temperature.

The transition probabilities for line emission have been calculated using the oscillator strengths given by Fabry (FAB76). The rate coefficients for radiative recombination are taken from Norcross and Stone (NOR66).

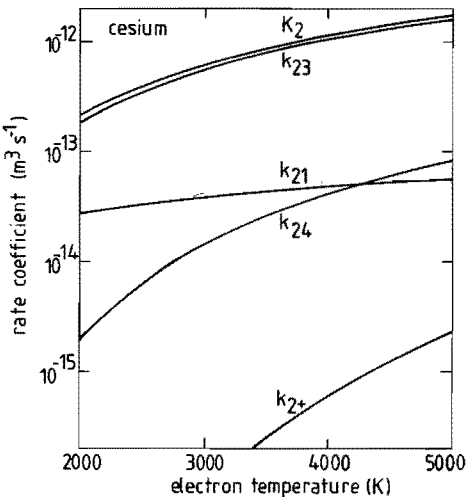

FIG. 4.4. The rate coefficients for collisional processes in which the second effective level of neutral cesium is involved (according to the theory of Gryzinski) as a function of the electron temperature.

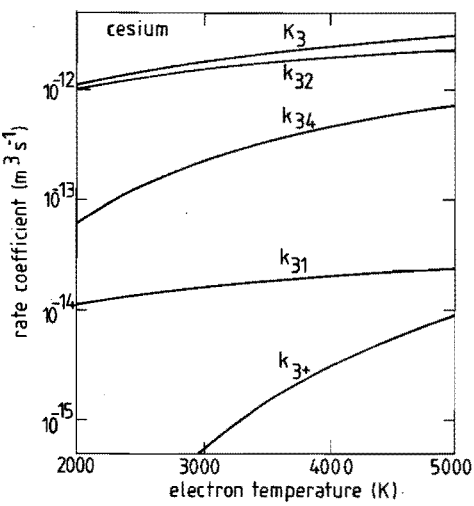

FIG. 4.5. The rate coefficients for collisional processes in which the third effective level of neutral cesium is involved (according to the theory of Gryzinski) as a function of the electron temperature.

4.2 Ionization of neutral cesium

4.2.1 The escape of resonance radiation

In this subsection the Doppler and Lorentz widths of resonance lines of neutral cesium will be calculated. Together with the density of ground level neutrals these calculations lead to the escape factor. The escape factor is needed to calculate the net ionization of neutral cesium. All widths used are full width at half maximum (FWHM) values.

The numerical values for the widths given in this subsection apply to the radiative transitions from level 2 to the ground level. The effective level 2 consists of two sublevels: $6P_{1/2}$ and $6P_{3/2}$. The widths of the lines $6P_{1/2} - 6S_{1/2}$ and $6P_{3/2} - 6S_{1/2}$ are given separately and are denoted by the superscripts a and b respectively. The wavelength and the centre frequency are for the first radiative transition $\lambda = 894.4$ nm and $\upsilon_0 = 3.35 \times 10^{14}$ s^{-1} and for the second radiative transition $\lambda = 852.1$ nm and $\upsilon_0 = 3.52 \times 10^{14}$ s^{-1}. The next level that emits resonance radiation is level 5. Because this level and the higher levels have much smaller populations, their contributions to the net source term of the ground level are also much smaller. Besides that level 5 has a small transition probability for resonance radiation compared to level 2. Therefore we will restrict ourselves to the resonance transitions from level 2 and neglect resonance transitions from higher levels.

The thermal motion of radiating neutrals leads to a Gaussian profile of the line intensity (MIT73):

$$I_G(\upsilon) = \frac{2\sqrt{\ln 2}}{\sqrt{\pi}\,\Delta\upsilon_G} \exp\left[-\left[\frac{2\sqrt{\ln 2}\,(\upsilon - \upsilon_0)}{\Delta\upsilon_G}\right]^2\right] \tag{4.1}$$

The centre frequency of the line is denoted by υ_0 and the width (FWHM) by

$$\Delta\upsilon_G = \upsilon_0 \frac{2\sqrt{\ln 2}}{c}\left[\frac{2kT}{M_{Cs}}\right]^{1/2} \tag{4.2}$$

M_{Cs} is the mass of the cesium neutral. $I_G(\upsilon)$ is normalized to have $\int I_G(\upsilon)\, d\upsilon = 1$. The factor 2 in Eq. (4.2) arises from the use of the full width instead of the half width. The factor $\sqrt{\ln 2}$ arises from the use of the width at half the peak value instead of the width at the

TABLE 4.2. The width of the Doppler profile for the $6P_{1/2}$-$6S_{1/2}$ (a) and $6P_{3/2}$-$6S_{1/2}$ (b) lines of cesium for some temperatures of the heavy particle (T_h).

T_h (K)	$\Delta\nu_D^a$ (s^{-1})	$\Delta\nu_D^b$ (s^{-1})
1000	6.56×10^8	6.89×10^8
2000	9.28×10^8	9.74×10^8
3000	1.14×10^9	1.19×10^9
4000	1.31×10^9	1.38×10^9
5000	1.47×10^9	1.54×10^9

$1/e$ value. The Gaussian widths are given in Table 4.2 for some temperatures of the emitting neutrals.

The broadening by collisions of the emitting particle with other particles leads to a Lorentzian profile:

$$I_L(\nu) = \frac{1}{2}\frac{\Delta\nu_L}{\pi}\frac{1}{(\nu - \nu_0)^2 + (\tfrac{1}{2}\Delta\nu_L)^2} \tag{4.3}$$

The FWHM value of the Lorentzian profile is given by $\Delta\nu_L$. Its magnitude will be considered later. First the convolution of a Gaussian and a Lorentzian profile will be given. This is a Voigt profile:

$$V(a,x) = \frac{a}{\pi}\int_{-\infty}^{+\infty}\frac{\exp(-y^2)}{a^2 + (x - y)^2}\,dy \tag{4.4}$$

The parameter a is determined by the ratio of the widths of the two profiles:

$$a = \sqrt{\ln 2}\,\frac{\Delta\nu_L}{\Delta\nu_G} \tag{4.5}$$

The variable x is a scaled frequency:

$$x = 2\sqrt{\ln 2}\,\frac{\nu - \nu_0}{\Delta\nu_G} \tag{4.6}$$

The Gaussian and Lorentzian profiles given by Eqs. (4.1) and (4.2) are special cases of the Voigt profile given by Eq. (4.4). When $a = 0$ one gets the Gaussian profile, when a tends to infinity one obtains the Lorentzian profile. The two situations will be denoted by Gaussian

limit and Lorentzian limit respectively. In the latter situation one cannot use the variable x because $\Delta\nu_G = 0$, but instead the variable x/a is used.

By integrating the probability that the radiation traverses a certain distance in the plasma (see subsection 2.3.4) over the frequency and the plasma volume one gets the escape factor (HOL51). The absorption profile is assumed to be the same as the emission profile. For a Gaussian line profile the absorption coefficient in the centre of the profile is given by (MIT73)

$$(k_o)_G = \frac{\sqrt{\ln 2}}{4\pi\sqrt{\pi}} \frac{c^2}{\nu_o^2} \frac{g_u}{g_l} \frac{A_{ul}}{\Delta\nu_D} n_l \tag{4.7}$$

The subscripts u and l denote the upper and the lower levels involved in the radiative transition. For a Lorentzian profile the absorption coefficient in the middle of the profile is given by (MIT73)

$$(k_o)_L = \frac{1}{4\pi^2} \frac{c^2}{\nu_o^2} \frac{g_u}{g_l} \frac{A_{ul}}{\Delta\nu_L} n_l \tag{4.8}$$

If in the integration over the plasma volume an infinitely long cylinder with radius R is assumed as the plasma volume, this leads to the Gaussian and the Lorentzian limits for the escape factor as given by Eqs. (2.44) and (2.45). Note that these values are only valid for large values of the optical depth ($k_oR \gg 1$). The escape factor for small values of the optical depth has been calculated by Drawin an Emard (DRA73C). The escape factor is drawn in Fig. 4.6 as a function of k_oR for all values of k_oR. The parameter in this figure is the

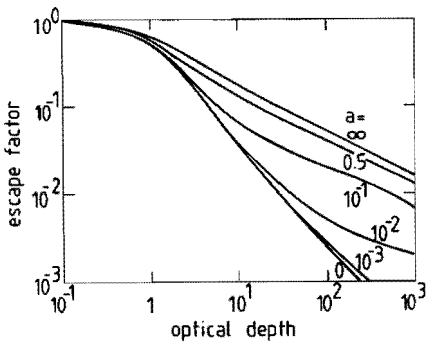

FIG. 4.6. The escape factor of a line with a Voigt profile as a function of the optical depth. The parameter in this figure is the ratio a of the widths of the Lorentzian and the Gaussian parts of the profile as defined by Eq. (4.5).

ratio a of the widths of the two profiles as defined by Eq. (4.5). The curve with $a = 0$ is the Gaussian limit and that with $a = \infty$ is the Lorentzian limit. For Voigt profiles the escape factor is in between these curves. For k_0 one has to use the absorption in the centre of the Voigt profile:

$$(k_0)_V = \frac{\sqrt{\ln 2}}{4\pi\sqrt{\pi}} \frac{c^2}{\nu_0^2} \frac{g_u}{g_l} \frac{A_{ul}}{\Delta\nu_V} n_l \qquad (4.9)$$

The width of the Voigt profile is given by $\Delta\nu_V$. The escape factor can be derived from Fig. 4.6 for known values of $(k_0)_V$, the radius R of the filament, and a.

The three broadening effects causing a Lorentzian profile will be discussed here. A standard condition for the heavy particles is used. It includes a heavy particle temperature $T_h = 1000$ K, a total pressure $p = 5 \times 10^4$ Pa, and a seed fraction SF (total cesium density divided by the argon density) of 10^{-3}. Since we here only need an estimation of the contributions of the different broadening mechanisms to the line profile, in this subsection the LTE value for the electron density at a given electron temperature is used. This is of course justified when the deviation from equilibrium is small. In the analysis of the mass balance and the energy balance of the electrons (from Sec. 4.3) the deviation from equilibrium will be taken into account throughout.

For the Stark effect, the first broadening mechanism which is considered, the results of the theory of Griem (GRI64,GRI74) are used. Over a wide range of conditions the profile is Lorentzian with the FWHM given by

$$\Delta\nu_S = \left[1 + 1.75a \left[\frac{n_e}{10^{22}}\right]^{1/4} \left[1 - 0.75 \frac{\rho_i}{\rho_D}\right]\right] \times \Delta\nu_e \times \left[\frac{n_e}{10^{22}}\right] \qquad (4.10)$$

The electron density, n_e, has to be given in m^{-3}. The parameters a and $\Delta\nu_e$ which are weak functions of the electron temperature are tabulated by Griem (GRI74). The broadening by electrons is given by the term $\Delta\nu_e \times (n_e/10^{22})$ and the term containing a gives the contribution of the ions. For this contribution the ratio of the mean ion-ion separation $\rho_i = (4\pi n_e/3)^{-1/3}$ and the Debye radius $\rho_D = (n_e e^2/\epsilon_0 k T_e)^{-1/2}$ is important.

Eq. (4.10) is valid provided (GRI74)

$$A = \alpha \left[\frac{n_e}{10^{22}}\right]^{1/4} \leq 0.5$$

$$\frac{\rho_i}{\rho_D} \leq 0.8$$

$$\sigma = \frac{\Delta\nu_e \rho_i}{\pi \bar{v}_i} > 1$$

Here $\bar{v}_i$ is the mean relative velocity between the perturbing ion and the perturbed atom. In Table 4.3 the values of the parameters taken from Griem are given for the two lowest resonance transitions. For the electron temperatures and electron densities considered here the above mentioned conditions are fulfilled. The resulting widths are given in Table 4.4.

TABLE 4.3. Stark effect parameters for the $6P_{1/2}$-$6S_{1/2}$ (a) and $6P_{3/2}$-$6S_{1/2}$ (b) lines of cesium according to Griem (GRI74).

	T_e (K)	$\Delta\nu_e$ (s^{-1})	α
(a)	2500	5.47×10^9	0.044
	5000	6.52×10^9	0.038
(b)	2500	5.67×10^9	0.047
	5000	6.90×10^9	0.041

TABLE 4.4. Stark broadening of the $6P_{1/2}$-$6S_{1/2}$ (a) and $6P_{3/2}$-$6S_{1/2}$ (b) lines of cesium at the standard conditon for the heavy particles.

T_e (K)	$n_{e,LTE}$ (m^{-3})	ρ_i/ρ_D	$\Delta\nu_S^a$ (s^{-1})	$\Delta\nu_S^b$ (s^{-1})
2000	1.11×10^{19}	0.300	5.90×10^6	6.25×10^6
3000	5.93×10^{20}	0.476	3.45×10^8	3.65×10^8
4000	2.68×10^{21}	0.530	1.68×10^9	1.78×10^9
5000	3.50×10^{21}	0.496	2.35×10^9	2.49×10^9

The second broadening mechanism causing a Lorentzian profile is resonance broadening. The FWHM in frequency is given by (GRI74)

$$\Delta\nu_R = \frac{3e^2}{4\pi^2\epsilon_0 m_e}\,(g_l/g_u)^{1/2}\,\frac{f\,n_{CsI}}{\nu_0} \tag{4.11}$$

For the absorption oscillator strength, f, values of Fabry (FAB76) are used. In Eq. (4.11) N_{CsI} is the density of neutral cesium. The resonance broadening only depends directly on this density and not on other plasma parameters. Therefore, the resonance broadening is small for high electron temperatures at which the cesium is largely ionized. The resulting widths are given in Table 4.5.

TABLE 4.5. Resonance broadening of the $6P_{1/2}$-$6S_{1/2}$ (a) and $6P_{3/2}$-$6S_{1/2}$ (b) lines of cesium at the standard condition for the heavy particles.

T_e (K)	$n_{e,LTE}$ (m^{-3})	n_{CsI} (m^{-3})	$\Delta\nu_R^a$ (s^{-1})	$\Delta\nu_R^b$ (s^{-1})
2000	1.11×10^{19}	3.61×10^{21}	9.12×10^{8}	1.26×10^{9}
3000	5.93×10^{20}	3.03×10^{21}	7.64×10^{8}	1.06×10^{9}
4000	2.68×10^{21}	9.43×10^{20}	2.34×10^{8}	3.30×10^{8}
5000	3.50×10^{21}	1.23×10^{20}	3.10×10^{7}	4.30×10^{7}

The third broadening mechanism is the Van der Waals broadening caused by collisions of excited cesium neutrals with neutral argon. The FWHM is given by (GRI64)

$$\Delta\nu_W = 2\pi \left[\frac{9\pi\hbar^5 R_u^2}{16 m_e^3 E_p^2}\right]^{0.4} \left[\frac{8kT}{\pi}\left[\frac{1}{M_{Ar}} + \frac{1}{M_{Cs}}\right]\right]^{0.3} n_{Ar} \tag{4.12}$$

E_p is the energy of the first excited level of argon. The matrix element R_u^2 is well estimated by

$$R_u^2 = \frac{1}{2}\,\frac{E_H}{E_{Cs} - E_u}\left[5\,\frac{z^2 E_H}{E_{Cs} - E_u} + 1 - 3l_u(l_u + 1)\right] \tag{4.13}$$

E_H and E_{Cs} are the ionization energies of hydrogen and cesium respectively, E_u is the excitation energy of the upper state of the line, and l_u is its orbital quantum number. The effective charge, z, acting on the electron is 1 because neutral lines are considered here. The Van

der Waals broadenings of the two lines considered in this subsection are almost equal for a broad range of gasdynamical conditions. The difference is caused by the slightly different values of the matrix element R_u^2. Moreover, the broadening is constant for a fixed heavy particle condition. For the standard condition used above, the Van der Waals broadening for both lines is respectively

$$\Delta\nu_W^a = 1.579 \times 10^{10}\ s^{-1} \tag{4.14}$$

and

$$\Delta\nu_W^b = 1.618 \times 10^{10}\ s^{-1} \tag{4.15}$$

Note that these values are upper limits. Provided that the pressure remains the same, heating of argon by electrons causes the Van der Waals broadening to become smaller due to the lower argon neutral density (see Eq. (4.12)).

For the lines considered here the Lorentzian widths and their sum are given in Fig. 4.7 as a function of the electron density. The Van der Waals broadening is dominant. Resonance broadening gives a small

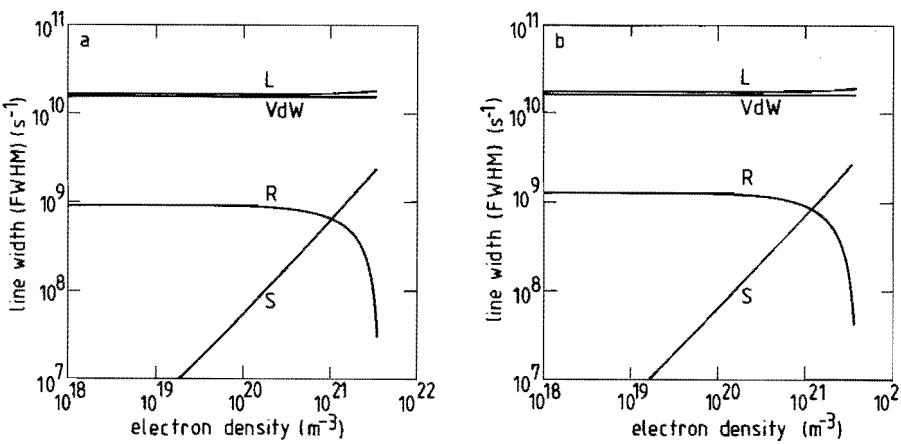

FIG. 4.7. Line width of the $6P_{1/2}$-$6S_{1/2}$ (a) and $6P_{3/2}$-$6S_{1/2}$ (b) lines of cesium at the standard condition for the heavy particles as a function of the electron density. The total Lorentzian width is denoted by L; the other curves denote the contributions of Van der Waals broadening (VdW), resonance broadening (R), and Stark broadening (S).

contribution. Stark broadening has to be taken into account at high electron densities ($n_e > 10^{21}$ m^{-3}). The Gaussian width (see Table 4.2) is small compared with the Lorentzian width. For the standard heavy particle condition the parameter α as given by Eq. (4.5) is about 20. This means that the line profile can be considered to be Lorentzian in calculating the escape factor (DRA73C). In Fig. 4.8 the values of k_0 are drawn as a function of the electron density. For the calculation of the escape factor a certain radius R has to be assumed. Here the values of 10^{-3} and 10^{-4} m are used as an upper and a lower limit. In the Lorentzian limit the escape factor is given by (BAT81,KLE69)

$$\Lambda = \exp\left[-\frac{1}{2}(k_0)_L R\right] \times I_0\left[\frac{1}{2}(k_0)_L R\right] \tag{4.16}$$

I_0 is the modified Bessel function of the order zero.

In the collisional radiative model the upper levels of the two lines considered here are combined to one effective level. An effective transition probability A_{21} is used. Also an effective escape factor Λ_{21} has to be used. This is given by (ROS81)

$$A_{21}\Lambda_{21} = \frac{g_u^a A^a \Lambda^a + g_u^b A^b \Lambda^b}{g_u^a + g_u^b} \tag{4.17}$$

Here g_u, A, and Λ denote the statistical weight, the transition probability, and the escape factor of the sublevels $6P_{1/2}$ (a) and $6P_{3/2}$ (b) of the effective level 2. With the transition probabilities calculated from the oscillator strengths given by Fabry (FAB76) this leads to

$$\Lambda_{21} = 0.306\ \Lambda^a + 0.694\ \Lambda^b \tag{4.18}$$

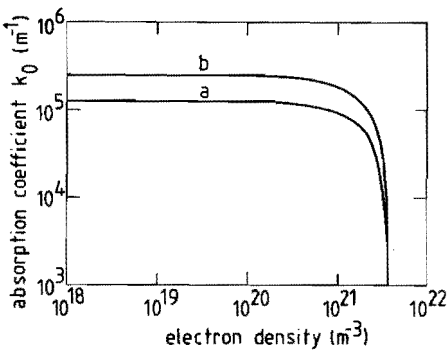

FIG. 4.8. The absorption coefficient in the middle of a profile of the $6P_{1/2}$-$6S_{1/2}$ (a) and the $6P_{3/2}$-$6S_{1/2}$ (b) lines of cesium at the standard condition for the heavy particles as a function of the electron density.

The resulting effective escape factor is given in Fig. 4.9 as a function of the electron density. The escape factor is almost constant for electron densities up to 10^{21} m^{-3} because the main broadening mechanism (Van der Waals broadening) is not influenced by the electron density. The strong rise of the escape factor for large values of the electron density is mainly caused by the low density of the absorbing cesium ground level.

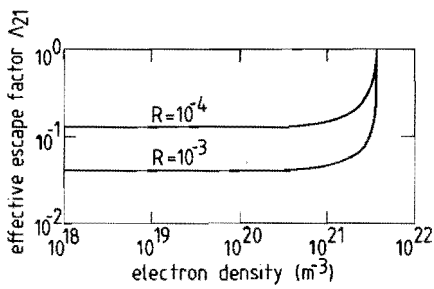

FIG. 4.9. The escape factor for resonance radiation from effective level two (transition 6P-6S) of cesium at the standard condition for two different values of the radius R of a filament as a function of the electron density.

4.2.2 *Results of a model with three levels*

A collisional radiative model taking three levels into account will be considered in this subsection. Assuming the fourth and higher levels to be in LTE ($\delta b_q = 0$, $q \geq 4$), one can derive rather simple analytical expressions for the overpopulations of the second and third level. In this way the effects of the different collisional and radiative processes on the overpopulations of the lowest levels can be made clear. Also the net source term in the mass balance of the electrons can be evaluated. The consequences of the assumption that only a few levels are not in equilibrium will be examined in the next subsection.

The balance equations given by Eq. (2.25) for $q = 2$ and $q = 3$ have to be solved to get δb_2 and δb_3 as a function of δb_1. The overpopulations for q greater than or equal to 4 are assumed to be zero ($N = 3$). The plasma is optically thin for radiation of non-resonance lines and of radiative recombination. The corresponding escape factors are equal to one. Only the resonance radiation from level 2 is partially trapped. The escape factor Λ_{21} is calculated according to the theory presented in the previous subsection. The resulting equations

read

$$- (n_e K_2 + A_{21}\Lambda_{21})\delta b_2 + (n_e k_{23} + B_{32}A_{32})\delta b_3$$

$$= - n_e k_{21}\delta b_1 - S_{2+}k^{(2)}_{+2} + A_{21}\Lambda_{21} - B_{32}A_{32} \qquad (4.19a)$$

and

$$(n_e k_{32} \qquad)\delta b_2 - (n_e K_3 + \quad A_{32})\delta b_3$$

$$= - n_e k_{31}\delta b_1 - S_{3+}k^{(2)}_{+3} + A_{32} \qquad (4.19b)$$

These equations can also be written in the matrix notation as given in Subsec. 2.3.2. The factors preceding δb_2 and δb_3 in Eq. (4.19) are the elements of the matrix **Y**. The determinant of this matrix is given by

$$D_Y = n_e^2 K_2 K_3 \left[1 + \frac{A_{21}\Lambda_{21}}{n_e K_2}\right]\left[1 + \frac{A_{32}}{n_e K_3}\right]$$

$$- n_e^2 k_{23} k_{32}\left[1 + \frac{B_{32}A_{32}}{n_e k_{23}}\right] \qquad (4.20)$$

The main terms of this determinant are given by the collisional rate coefficients of the levels 2 and 3 (K_2, K_3, k_{23}, and k_{32}). The radiative terms are corrections. The solution of Eq. (4.19) is given by

$$\delta b_2 = \frac{n_e^2}{D_Y}\left\{\left[K_3 k_{21}\left[1 + \frac{A_{32}}{n_e K_3}\right] + k_{23}k_{31}\left[1 + \frac{\gamma}{n_e k_{23}}\right]\right]\delta b_1\right.$$

$$\left. + \left[\frac{\alpha K_3}{n_e}\left[1 + \frac{A_{32}}{n_e K_3}\right] + \frac{\beta k_{23}}{n_e}\left[1 + \frac{\gamma}{n_e k_{23}}\right]\right]\right\} \qquad (4.21a)$$

and

$$\delta b_3 = \frac{n_e^2}{D_Y}\left\{\left[K_2 k_{31}\left[1 + \frac{A_{21}\Lambda_{21}}{n_e K_2}\right] + k_{32}k_{21} \qquad\right]\delta b_1\right.$$

$$\left. + \left[\frac{\alpha k_{32}}{n_e} \qquad + \frac{\beta K_2}{n_e}\left[1 + \frac{A_{21}\Lambda_{21}}{n_e K_2}\right]\right]\right\} \qquad (4.21b)$$

The symbols α, β, and γ in Eq. (4.21) represent radiative terms:

$$\alpha = S_{2+}k^{(2)}_{2+} - A_{21}\Lambda_{21} + B_{32}A_{32} \qquad (4.22a)$$

$$\beta = S_{3+} k_{3+}^{(2)} - A_{32} + B_{43} A_{43} \qquad (4.22b)$$

$$\gamma = B_{32} A_{32} \qquad (4.22c)$$

The solution is similar to that given by Timmermans et al. (TIM85). The differences are caused by the omission of some terms in (TIM85) that are negligible in the atmospheric argon plasma at 1 eV which Timmermans considered.

To evaluate the influence of the different processes on the overpopulation of excited levels, the LTE value for the electron density, $n_{e,LTE}$, will be used in this section (see also Subsec. 2.3.2). The overpopulations of the excited levels then obey Eq. (2.28):

$$\delta b_q = r_q \delta b_1 + \rho_q$$

By the use of $n_{e,LTE}$ the parameters r_q and ρ_q depend only on the electron temperature T_e and the escape factor Λ_{21}. For this escape factor the values obtained in the previous subsection will be used. For comparison also the results for r_q and ρ_q calculated with $\Lambda_{21} = 0$ ($R = \infty$) will be given.

The parameters r_q give the relation between the overpopulation of the excited levels q and the overpopulation of the ground level. These parameters are given by the terms containing δb_1 in Eqs. (4.21a) and (4.21b). In the Ar-Cs plasma under consideration it is mainly determined by collisional processes. For an evaluation of the importance of the resonance radiation radiation one has to compare the term $A_{21}\Lambda_{21}$ with $n_e K_2$ or $n_e k_{21}$ in Eqs. (4.20) and (4.21). At low values of the electron temperature the product of n_e and K_2 or k_{21} is small and resonance radiation has to be taken into account. At high values of the electron temperature resonance radiation can be neglected even when Λ_{21} reaches its maximum value of 1. This can be seen in Fig. 4.10 where the parameter r_2 is drawn as a function of the electron temperature for different values of R. For r_3 the same dependencies are found but the values for r_3 are 10 to 20% smaller than those for r_2. From Fig. 4.10 it follows that the parameter r_2 becomes smaller for smaller radii. The coupling between level 2 and level 1, which is mainly determined by collisional processes, gets weaker when more radiation escapes.

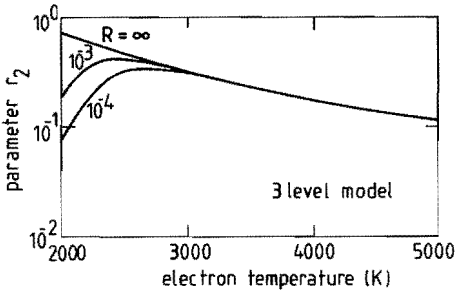

FIG. 4.10. The parameter r_2, which gives the proportionality between the overpopulation of the second level and the overpopulation of the ground level, as a function of the electron temperature. These values are given for different radii R of a filament. The curve with $R = \infty$ corresponds with the situation in which no resonance radiation from level two escapes ($\Lambda_{21} = 0$). The fourth and higher levels are assumed to be in equilibrium.

The parameters ρ_q give the overpopulation of excited level q when the ground level is in equilibrium. These parameters are given by Eqs. (4.21a) and (4.21b) for $\delta b_1 = 0$. The parameters ρ_q depend much more on radiative processes than the parameters r_q because of the radiative terms α and β. In particular resonance radiation is important. For small radii the loss by resonance radiation of level 2 is greater than the gain by cascade radiation from higher levels. This results in negative values for α (see Eq. (4.22a)) and consequently also for ρ_2 and ρ_3. At low temperatures ρ_2 tends to -1 which corresponds with a very small population of level 2. When all resonance radiation is trapped, ρ_2 is positive because of the population by radiative recombination and cascade radiation ($\alpha > 0$). The parameter ρ_2 is drawn in Fig. 4.11 as a function of the electron temperature for different values of R. The values of the parameter ρ_3 are comparable.

The most important feature of these results is the magnitude of the parameters r_2, r_3, ρ_2, and ρ_3. These parameters are two to three orders larger than the corresponding parameters for argon (see the example at the end of Subsec. 2.3.2). This is mainly caused by the various contributions of the (de-)excitation rates of the levels 2 and 3 to the total rate coefficient of these levels. As can be seen in Fig. 4.4, the excitation from level 2 to level 3 (k_{23}) is the most important contribution to the total rate coefficient for collisions of level 2 (K_2). For level 3 the situation is quite different. According to Fig. 4.5 the total rate coefficient for collisions (K_3) is mainly

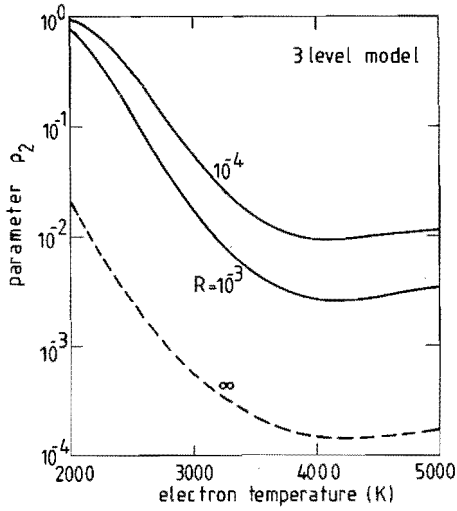

FIG. 4.11. The absolute value of the overpopulation of level two when $\delta b_1 = 0$ (ρ_2) for different radii R of a filament as a function of the electron temperature. This overpopulation is positive for $R = \infty$ (dashed curve) and negative for $R = 10^{-3}$ m and $R = 10^{-4}$ m (solid curves). The fourth and higher levels are assumed to be in equilibrium.

determined by the rate coefficient for de-excitation to level 2 (k_{32}). The products K_2K_3 and $k_{23}k_{32}$ are almost equal and the determinant D_Y is small. Therefore the parameters r_2 and r_3 are large in general. Consequently step-wise ionization is small and the overpopulations of the levels 2 and 3 are strongly coupled. In argon the situation is different because excitation to higher levels is dominant for level 3. The radiative terms in the determinant D_Y are of minor importance except for low electron temperatures and small radii which lead to large values of A_{21}).

The magnitudes of the parameters r_2, r_3, ρ_2, and ρ_3 have important consequences for the applicability of a three level model to the cesium neutral system. The assumption that the overpopulation of the fourth and higher levels is zero becomes questionable. The calculated overpopulation of the lower levels is too small because de-excitation from higher levels has not been accounted for. Besides that the overpopulation of excited levels is not negligible in comparison with that of the ground level. The de-excitation annuls an important part of the excitation in the net source term for the electrons as given by Eq. (2.24). Because the overpopulations of the excited levels are too small, the net source term calculated with these overpopulations is too large. A model taking more levels into account which are not in equilibrium is necessary to describe the overpopulations of excited levels and the resulting non-equilibrium ionization properly.

4.2.3 *Results of a model with many levels*

A collisional radiative model can be applied to more levels in a similar way as described in the previous subsection. Again the balance equations for the levels taken into account have to be solved. In this subsection the results of a model with ten levels will be discussed. In the next subsection the resulting source term will be discussed as a function of the number of levels considered.

For a model with ten levels the set of equations given by Eq. (2.25) for $q = 2$ up to $q = 10$ has to be solved. This set consists of nine linear equations in the overpopulations δb_2, δb_3, ... , δb_{10}. Analytical expressions for these overpopulations can be derived but are very complicated. To simplify the evaluation, the LTE value of the electron density, $n_{e,LTE}$, is used and the overpopulations of excited levels obey Eq. (2.28). The parameters ρ_q directly result from the solution of the set of equations given by Eq. (2.25) with $\delta b_1 = 0$. The coefficients ρ_q are given by the differences between the overpopulations calculated with $\delta b_1 = 1$ and $\delta b_1 = 0$. The parameters r_q and ρ_q depend on the escape factor Λ_{21}. The values of Λ_{21} calculated for filament radii of 10^{-3} and 10^{-4} m are used (Subsec. 4.2.1). Also the results for $\Lambda_{21} = 0$ ($R = \infty$) are given in Figs. 4.12 and 4.13 where r_q and ρ_q are plotted as a function of the electron density. These figures have to be compared with Figs. 4.10 and 4.11 respectively where the same quantities are given for a model with three levels out of equilibrium.

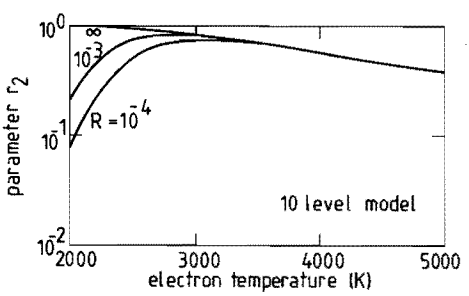

FIG. 4.12. The parameter r_2, which gives the proportionality between the overpopulation of the second level and the overpopulation of the ground level, as a function of the electron temperature. These values are given for different radii R of a filament. The curve with $R = \infty$ corresponds with the situation in which no resonance radiation from level two escapes ($\Lambda_{21} = 0$). The 11th and higher levels are assumed to be in equilibrium.

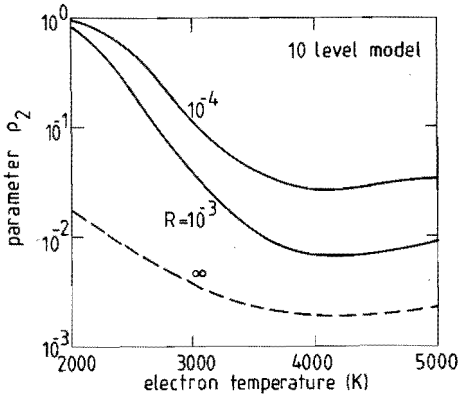

FIG. 4.13. The absolute value of the overpopulation of level two when $\delta b_1 = 0$ (ρ_2) for different radii R of a filament as a function of the electron temperature. This overpopulation is positive for $R = \infty$ (dashed curve) and negative for $R = 10^{-3}$ m and $R = 10^{-4}$ m (solid curves). The 11th and higher levels are assumed to be in equilibrium.

The parameter r_2 calculated with the ten level model is greater than calculated with the three level model. For a broad range of electron temperatures, r_2 is greater than 0.4 which implies that a large part of the excitation from the ground level to level 2 is annulled by de-excitation. The parameter ρ_2 is smaller when ten levels are taken into account (mind the negative sign of ρ_2 for $R = 10^{-3}$ m and $R = 10^{-4}$ m). This is caused by the smaller population of higher excited levels. For level 3 the situation is similar (not shown in the figures). The conclusion is that the number of levels assumed to be out of equilibrium in the previous subsection was too small. Our main interest is the net source term in the mass balance of the electrons. Therefore the influence of the number of levels considered on the overpopulation of the excited levels is not extensively described here. The influence on the net source term is given in the next subsection.

In Figs. 4.14 and 4.15 the parameters for the overpopulation of the second up to the tenth level are given for some values of the electron temperature. The quantity at the horizontal axis is the effective quantum number p_q which is defined by

$$p_q = \left[\frac{Ry}{E_{qII}}\right]^{1/2} \tag{4.23}$$

Here Ry is the Rydberg energy (13.6 eV) and E_{qII} is the ionization energy of level q (see Table 4.1). The overall behaviour of the parameters is fairly good represented by a proportionality with p_q^{-6} (straight dashed-dotted lines in Figs. 4.14 and 4.15). This is in accordance with the results obtained by Van der Mullen for the elec-

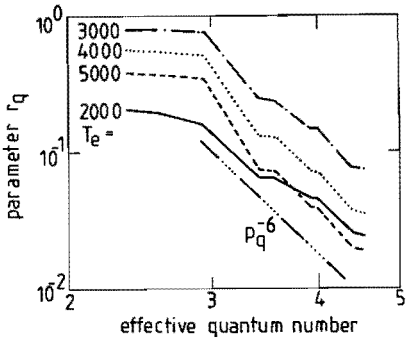

FIG. 4.14. The parameters r_q, which give the proportionality between the overpopulation of level q and the overpopulation of the ground level, as a function of the effective quantum number for four different electron temperatures (left-hand top corner). The line -•••-••• gives a dependence on the effective quantum number p proportional to p^{-6}. The values in this figure are calculated for a radius of 10^{-3} m.

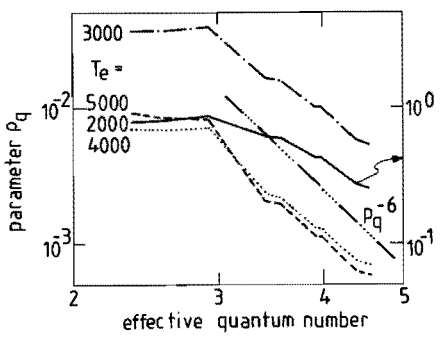

FIG. 4.15. The absolute value of the overpopulation of level q when $\delta b_1 = 0$ (ρ_2) as a function of the electron density for four different electron temperatures (left-hand top corner). The line -•••-••• gives a dependence on the effective quantum number p proportional to p^{-6}. The values in this figure are calculated for a radius of 10^{-3} m.

tron saturation balance (ESB) model (MUL86). ESB occurs when collisional transitions to the next higher and lower levels are much more important than radiative transitions or collisonal transitions to more remote levels. The parameters for the levels 2 and 3 are smaller than the p_q^{-6} dependency of the higher levels. This is caused by the radiative transitions from level 3 to level 2 and from level 2 to the ground level.

Another important feature in both Fig. 4.14 and Fig. 4.15 is the existence of groups of levels for which the parameters are almost the same. The explanation for this phenomenon can be found in the collisional (de-)excitation rates. In Table 4.6 the contributions of the excitation to the total collisional rate coefficients of the levels 2

TABLE 4.6. The contributions of excitation and de-excitation to the total collisional rate coefficient of the levels two to ten given in per cent. The electron temperature is 4000 K. The arrows indicate the predominant direction of collisional transitions.

q	exc. (%)	de-exc. (%)	
10	14.8	85.2	⇓
9	91.5	8.5	⇑
8	6.0	94.0	⇓
7	98.9	1.1	⇑
6	15.6	84.4	⇓
5	98.1	1.9	⇑
4	8.5	91.5	⇓
3	20.7	79.3	⇓
2	95.9	4.1	⇑

to 10 are given. The values in this table apply to an electron temperature of 4000 K but they are comparable for other values of the electron temperature. The effective levels can be divided into groups. For the lower levels of a group the excitation dominates whereas for the higher levels de-excitation dominates (see the arrows at the right hand side of Table 4.6). A similar division into groups is observed in the way level populations relaxate after a sudden change in electron temperature (WET80,BOR82).

4.2.4 *The net source term*

In this subsection the net source term for the electrons in the mass balance will be evaluated. The influence of the number of levels taken into account in the collisional radiative model is considered. The net source term for the electrons is given by Eq. (2.24):

$$\left[\frac{\partial n_e}{\partial t}\right]_{CR} = n_e n_{1,s} K_1 \delta b_1 - n_e n_{1,s} \sum_{q=2}^{M} (k_{1q} \delta b_q) - n_e n_{II} k_{+1}^{(2)} A_{+1}$$
$$- \sum_{q=2}^{N} (n_{q,s} A_{q1} A_{q1}) - \sum_{q=2}^{L} (n_{q,s} \delta b_q A_{q1} A_{q1})$$

The overpopulations of the excited levels (δb_q, $q \geq 2$) are linearly dependent on the overpopulation of the ground level δb_1 as in the two previous subsections. So the source term also consists of a part which changes linearly with δb_1 and a part which is independent of δb_1:

$$\left[\frac{\partial n_e}{\partial t}\right]_{CR} = n_e \nu_1 \delta b_1 - n_e \nu_0 \qquad (4.24)$$

ν_1 is the frequency associated with the rate of collisional processes from and to the ground level. ν_0 is the frequency associated with the rate of radiative processes to the ground level. The collisional term in Eq (4.24) leads to ionization for $\delta b_1 > 0$ and to recombination for $\delta b_1 < 0$. The radiative term always leads to recombination and therefore the minus sign has been used in Eq. (4.24). The frequencies ν_1 and ν_0 can be determined by substituting the overpopulations of the different levels calculated for $\delta b_1 = 0$ and $\delta b_1 = 1$ in Eq. (2.24). The results for models with different numbers of levels out of equilibrium are given in Figs. 4.16 and 4.17 for a radius of a filament of 10^{-3} m.

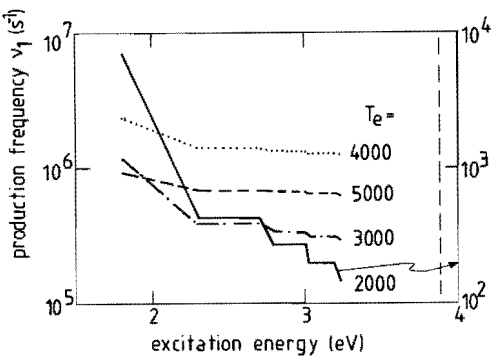

FIG. 4.16. The frequency ν_1 as a function of the excitation energy of the highest level taken into account in the CR model. The vertical dashed line denotes the ionization energy. The curves give the values of ν_1 at different electron temperatures (right-hand side)

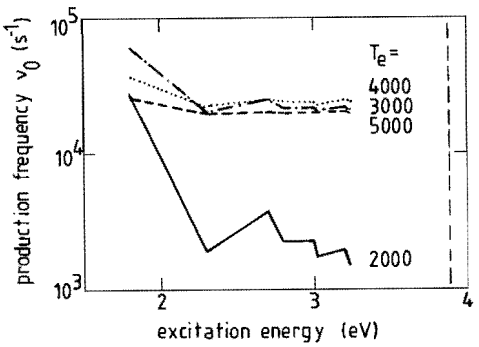

FIG. 4.17. The frequency ν_0 as a function of the excitation energy of the highest level taken into account in the CR model. The vertical dashed line denotes the ionization energy. The curves give the values of ν_0 at different electron temperatures (right-hand).

In these figures the frequencies ν_1 and ν_0 are plotted against the energies of the highest level which is assumed to be not in equilibrium. When more levels are taken into account these frequencies become smaller because the de-excitation from excited levels becomes larger.

Extrapolation of the curves in Figs. 4.16 and 4.17 towards the ionization energy (vertical dashed line) should give the correct source term (all levels taken into account in the CR model). For high electron temperatures the frequencies hardly change when eight or more levels are taken into account. For low electron temperatures the frequencies still change with the number of levels taken into account. Nevertheless the results of the 10 level model will be used. For other values of the radius R the dependency on the number of levels taken into account is comparable.

The frequency ν_1 is drawn in Fig. 4.18 as a function of the electron density for three different values of the radius of a filament. The excitation from the ground level ($n_{1,s}K_1$), which is the leading term in the expression for ν_1, is also given. A large part of the excitation is annulled by de-excitation and radiative transitions given by the second, fourth, and fifth term of the right-hand side of Eq. (2.24). For high electron densities the net source term is only determined by collisional processes and does not depend on the radius of the filament. For low electron densities also the escape of resonance radiation is important and therefore the net source term depends on the radius. Radiative recombination is negligible for all values of the electron density.

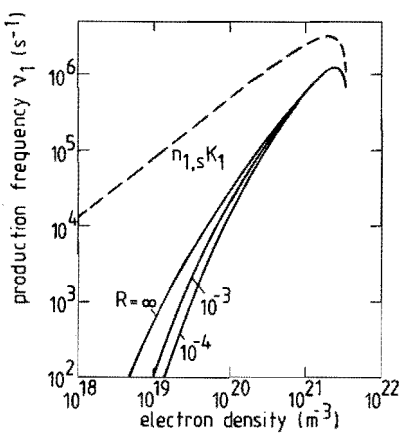

FIG. 4.18. The frequency ν_1 as a function of the electron density. The quantity R is the radius of a filament. The dashed curve with $n_{1,s}K_1$ gives the excitation part of ν_1.

The loss term of the frequency ν_1 (de-excitation and resonance radiation) is drawn in Fig. 4.19 as a function of the electron density for three different values of the radius of a filament. For a radius $R = \infty$ ($A_{21} = 0$) the loss term only consists of de-excitation. For finite radii and low electron densities the losses caused by resonance radiation are dominant. These losses almost equal the excitation ($n_{1,s}K_1$ in Fig. 4.18). For high electron densities de-excitation is dominant. The sum of both loss processes is about equal to the excitation. Consequently the frequency ν_1 is given by the small difference between excitation on the one hand and de-excitation and resonance radiation on the other hand.

The frequency ν_0 is drawn in Fig. 4.20 as a function of the electron density. For $R = 10^{-3}$ m and $R = 10^{-4}$ m, the resonance radiation is the most important term. As a result of the loss caused by the resonance radiation, the excited levels become underpopulated compared to the ground level. Therefore the resonance radiation is largely annulled by collisional processes. Radiative recombination is negligible. So like ν_1, ν_0 is given by the difference between two large quantities. Without escape of resonance radiation ($R = \infty$), ν_0 is determined by radiative recombination to excited levels. Radiative recombination to the ground level is negligible for all values of the radius. In contrast with the situation for ν_1, the influence of the radius is only important for high electron densities.

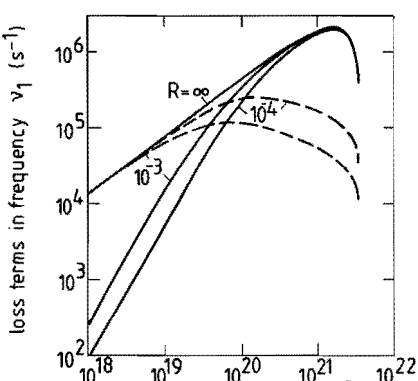

FIG. 4.19. The negative contributions to the frequency ν_1 caused by de-excitation (solid curves) and resonance radiation (dashed curves) as a function of the electron density.

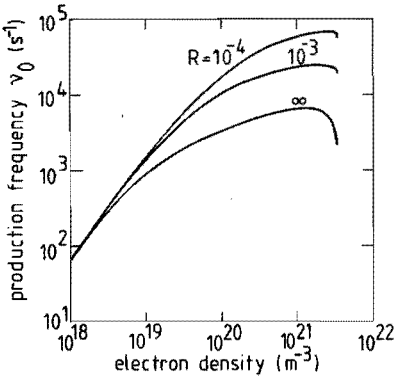

FIG. 4.20. The frequency ν_0 as a function of the electron density. The quantity R is the radius of a filament.

4.3 The electron mass balance

4.3.1 The contribution of transport

In the previous section the overpopulation of excited levels and the net source term of the electrons in the mass balance are discussed for given values of the overpopulation of the ground level. To calculate the overpopulation of the ground level the mass balance has to be used.

In a filament locally a high electron density exists. Electrons disappear by ambipolar diffusion. To maintain the electron density neutral cesium has to be ionized. The gain of electrons by ionization has to balance the loss of electrons by ambipolar diffusion. This is expressed by the electron mass balance Eq. (2.57). In a stationary case Eq. (2.57) reads

$$- \nabla\cdot(D_a \nabla n_e) = \left[\frac{\partial n_e}{\partial t}\right]_{CR} \tag{4.25}$$

As before a filament is assumed to be a cylinder with infinite length. For an approximation of the term $\nabla\cdot(D_a \nabla n_e)$ on the axis, one has to specify a certain radial profile for the electron density. In this work a Gaussian profile will be used:

$$n_e = n_{e0} \exp\left[-\left(\frac{r}{R_n}\right)^2\right] \tag{4.26}$$

Here n_{e0} is the value of n_e at the axis and R_n is the $1/e$ radius. In cylindrical coordinates the left-hand side of Eq. (4.25) becomes

$$- \nabla\cdot(D_a \nabla n_e) = - \frac{1}{r} \frac{\partial}{\partial r} \left[r D_a \frac{\partial n_e}{\partial r} \right]$$

$$= - D_a \frac{\partial^2 n_e}{\partial r^2} - \frac{D_a}{r} \frac{\partial n_e}{\partial r} - \frac{\partial D_a}{\partial r} \frac{\partial n_e}{\partial r}$$

To analyse of this term in a certain area around the axis we assume

$$D_a = D_{a0} \left[\frac{n_e}{n_{e0}} \right]^{\alpha}$$

where D_{a0} is the value of D_a for $n_e = n_{e0}$. This leads to

$$- \nabla\cdot(D_a \nabla n_e) = \frac{4 D_a n_e}{R_n^2} \left[1 - \left[\frac{1 + \alpha}{2} \right] \left[\frac{r}{R_n} \right]^2 \right] \tag{4.27}$$

The dependence of D_a on n_e is weak ($\alpha < 1$) so for $r \ll R_n$

$$- \nabla\cdot(D_a \nabla n_e) = \frac{4 D_a n_e}{R_n^2} \tag{4.28}$$

For simplicity the radius R_n will be taken equal to the radius R used before. The mass balance of the electrons for $r \ll R$ is given by Eqs. (4.24), (4.25), and (4.28):

$$\frac{4 D_a n_e}{R^2} = n_e \nu_1 \delta b_1 - n_e \nu_0 \tag{4.29}$$

Remember that ν_1 and ν_0 depend on the radius R of the filament. The overpopulation of the ground level for a filament with a certain radius R is given by

$$\delta b_1 = \frac{(4 D_{a0}/R^2) + \nu_0}{\nu_1} \qquad (r \ll R) \tag{4.30}$$

The quantities ν_1 and ν_0 are plotted in Figs. 4.18 and 4.20 respectively. So δb_1 is positive for all values of R.

For $R \longrightarrow \infty$ (no diffusion and no escape of resonance radiation) the source term has to be equal to zero and δb_1 is given by the ratio of ν_0 and ν_1. For finite values of R the magnitude of the normalized diffusion term $4 D_{a0}/R^2$ has to be considered. This term is only slightly dependent on the electron density. For $R = 10^{-3}$ m and

10^{19} $m^{-3} \leq n_e \leq 3.6 \times 10^{21}$ m^{-3} it varies between 2.54×10^2 s^{-1} and 4.66×10^2 s^{-1}. Comparison with ν_0 as given in Fig. 4.20 shows that diffusion is negligible in Eq. (4.30) for electron densities greater than 10^{20} m^{-3}. For these high electron densities δb_1 is again determined by the condition that the net source term, $\nu_1 \delta b_1 - \nu_0$, has to be zero. For $R = 10^{-4}$ m the diffusion term $4D_{a0}/R^2$ is a factor 100 larger than for $R = 10^{-3}$ m. This means that diffusion is important in Eq. (4.30) for all values of the electron density.

4.3.2 *Deviation from equilibrium*

The overpopulation of the ground level in the centre of a filament can be calculated by using Eq. (4.30). It was concluded that diffusion is only important for small radii ($R = 10^{-4}$ m) or for low electron densities when $R = 10^{-3}$ m. In other cases δb_1 depends on R by means of the escape factor Λ_{21} only. The results are given in Fig. 4.21 as a function of the electron density. The solid curves denote

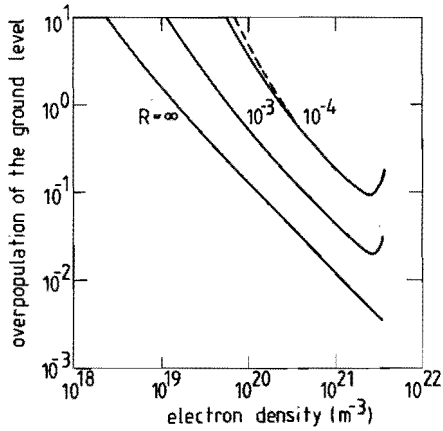

FIG. 4.21. The overpopulation of the ground level calculated by means of the mass balance as a function of the electron density for three different radii R of a filament. In the calculation of the solid curves the production frequencies as given in Figs. 4.16 and 4.17 are used (with $n_e = n_{e,LTE}$). The dashed curve has been calculated with production frequencies which are derived using the values for n_e resulting from the collisional radiative model.

the values of δb_1 calculated for electron temperatures coupled to the electron density by the Saha expression according to Eq. (2.16). The resulting values of δb_1 strongly depend on the radius R also when the diffusion term is negligible.

The non-equilibrium relation between δb_1 and n_e can be found by solving Eqs. (2.15) and (4.30) simultaneously. The value of δb_1 calculated with $n_e = n_{e,LTE}$ in Eq. (4.30) is used in the right-hand side of Eq. (2.15) to calculate a non-equilibrium value of n_e. This value is used in the right-hand side of Eq. (4.30) to calculate a new (higher) value of δb_1 and so on. After a few interations this procedure converges. The results are given in Fig. 4.21 by dashed curves. Note that for $R \longrightarrow \infty$ and $R = 10^{-3}$ m the differences between the values of δb_1 calculated with $n_e = n_{e,LTE}$ and those of δb_1 calculated by iteration are too small to be seen in this figure. For the same value of the electron density the electron temperatures are different for both curves. This compensates for the differences in δb_1 calculated with $n_{e,LTE}$ or those calculated after iteration. For $R = 10^{-4}$ m only differences occur for $\delta b_1 \geq 1$.

4.4 The electron energy balance

4.4.1 Source and transport terms

In this subsection the source and transport terms in the electron energy balance will be discussed. Numerical values are given which are calculated for the standard condition of the heavy particles as used before ($T_h = 1000$ K, $p = 5 \times 10^4$ Pa, and $SF = 10^{-3}$). The same sequence as in the right-hand side of Eq. (2.58) is used. Some of the terms depend on the radius of the filament considered. This dependence will be discussed in the next subsection.

For a calculation of the ohmic dissipation the electrical conductivity, σ, is needed. The electrical conductivity calculated according to Eq. (2.49) is plotted in Fig. 4.22 as a function of the electron density. For low electron densities σ is about proportional to n_e and for high electron densities σ is about proportional to $\sqrt{n_e}$. The dependence on the overpopulation of the ground level is small at a fixed value of n_e: for values of δb_1 between 0 and 1 and the corresponding value of T_e the maximum deviation in electrical conductivity is 2%

(not visible in Fig. 4.22). So the electrical conductivity can be considered to be a function of the electron density only. The ohmic dissipation reaches values up to 2×10^8 W/m^3 for a current density of 4×10^5 A/m^2 (WET84).

The term which gives the energy loss for the electrons caused by inelastic collisions (Q^e_{inel}) depends strongly on δb_1. In Fig. 4.23 this term is given as a function of the electron density for several values of δb_1. The radius of the filament is taken equal to 10^{-4} m. For larger values of the radius the absolute value of the inelastic source term is smaller due to the smaller escape of resonance radiation. Note that the reduced inelastic source term, viz. the inelastic source term divided by the electron density, is plotted. In this sub-

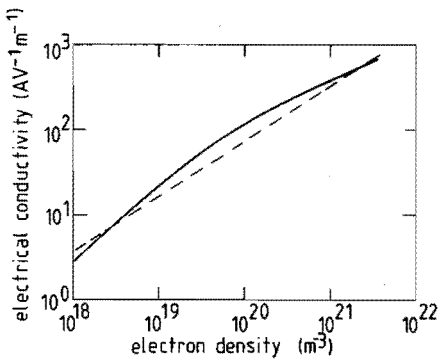

FIG. 4.22. The electrical conductivity, σ, as a function of the electron density at the standard condition for the heavy particles and $\delta b_1 = 0$. The dashed line gives the approximation as used in Eq. (4.54).

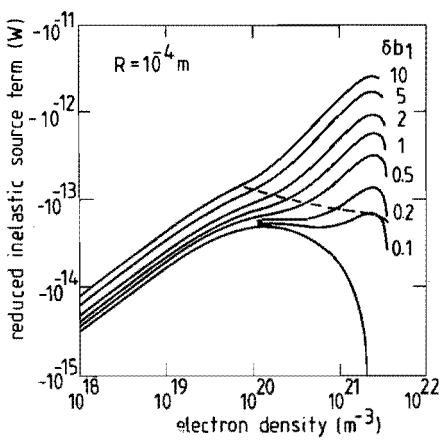

FIG. 4.23. The reduced inelastic source term (Q^e_{inel}/n_e) as a function of the electron density for different values of the overpopulation of the ground level δb_1 (solid curves). The values of δb_1 corresponding to each curve are given in the right-hand side of the figure. The data in this figure are calculated for a radius R = 10^{-4} m. The dashed curve gives the reduced inelastic source term as a function of the electron density calculated for the values of δb_1 which result from the mass balance.

section often the reduced values of a quantity are plotted to avoid figures with seven or eight decades along the ordinate. Use of the relation between δb_1 and n_e following from the mass balance for a radius $R = 10^{-4}$ m (Fig. 4.21) gives the dashed line in Fig. 4.23. The inelastic source term is then about proportional to $n_e^{0.8}$ and ranges between -7.0×10^6 W/m^3 and -1.7×10^8 W/m^3 for electron densities between 5.5×10^{19} m^{-3} and 3.6×10^{21} m^{-3}. So the inelastic source term is important for high values of the electron density and small radii. The dependence on the radius of this term is worked out in the next subsection.

The next term in the right-hand side of Eq. (2.58) is the energy loss of the electrons due to radiative recombination ($Q^e_{rad.rec}$). As is explained in Subsec. 2.3.3, a part of this term is already accounted for in the inelastic loss term Q^e_{inel}. The remaining part is given by Eq. (2.35). Because ten levels are taken into account in the CR model used to calculate Q^e_{inel}, the first summation in Eq. (2.35) goes up to $M = 10$. The escape factor for radiative recombination is 1 (see Subsec. 2.3.4). The result for the reduced radiative recombination term ($Q^e_{rad.rec}/n_e$) is given in Fig. 4.24 as a function of the electron density. This term is hardly influenced by δb_1 as can be expected. The maximum difference between values calculated with $\delta b_1 = 0$ and $\delta b_1 = 1$ is 4% which is not visible in Fig. 4.24. The reduced radiative recombination term is about proportional to $n_e^{1.08}$ (see Fig. 4.24). Therefore the radiative recombination term itself is about proportional to $n_e^{2.08}$. As can be seen in Eq. (2.35), the dependence of $Q^e_{rad.rec}$ on

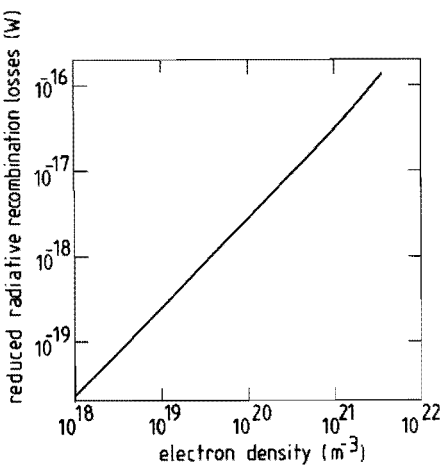

FIG. 4.24. The reduced radiative recombination losses ($Q^e_{rad.rec}/n_e$) as a function of the electron density at the standard condition for the heavy particles and $\delta b_1 = 0$.

n_e is mainly determined by the factor n_e^2 in front of the summations. The absolute value of this term is however small: 5×10^5 W/m^3 for the maximum possible electron density (fully ionized seed). This means that the energy loss of the electrons due to radiative recombination is negligible for all values of the electron density.

The situation is for the energy loss of the electrons due to line radiation ($Q^e_{line\ rad}$) similar to that of the loss due to radiative recombination. A part of this term is already accounted for in the inelastic loss term. The difference between both loss processes is that $Q^e_{line\ rad}$ contains no terms with $(3/2)kT_e$ like $Q^e_{rec.rad}$ does. The remaining part, which is given by Eq. (2.36), is of the same order of magnitude as the error made in the calculation of Q^e_{inel} by using a CR model with only ten levels. Because the parameters r_q and p_q do not change much when 9 or 10 levels are taken into account, also the inelastic loss term does not change much. Therefore the error in this term will be relatively small and consequently $Q^e_{line\ rad}$ will be neglected.

The loss caused by free-free radiation is also negligible. This is demonstrated by the calculation of this loss for electron temperatures of 2000 K and 5000 K which correspond with electron densities of 1.11×10^{19} m^{-3} and 3.50×10^{21} m^{-3} respectively. The energy loss of the electrons due to free-free radiation in collisions between electrons and ions (Q^{ei}_{ff}) is given by Eq. (2.39). Assuming $\xi_{eff} = 1$ and substituting the electron temperatures and electron densities mentioned above in Eq. (2.39) leads to values for Q^{ei}_{ff} of 7.80×10^{-1} W/m^3 and 1.23×10^5 W/m^3 respectively. The energy loss of the electrons due to free-free radiation emitted in collisions between electrons and neutrals (Q^{eo}_{ff}) is given by Eq. (2.40). The approximations for the cross sections for electron-neutral collisions as given by Mesland (MES82) have been used. For the above mentioned electron temperatures and electron densities this leads to values for Q^{eo}_{ff} of 1.43×10^1 W/m^3 and 2.81×10^4 W/m^3 respectively. So both the losses which are caused by free-free radiation are much smaller than the inelastic losses Q^e_{inel} and are negligible.

The reduced transfer of heat from electrons to heavy particles (P_{eh}/n_e) is plotted in Fig. 4.25 as a function of the electron density for $\delta b_1 = 0$. P_{eh} has been calculated according to Eq. (2.56) with the approximations for the cross sections as given by Mesland (MES82). The

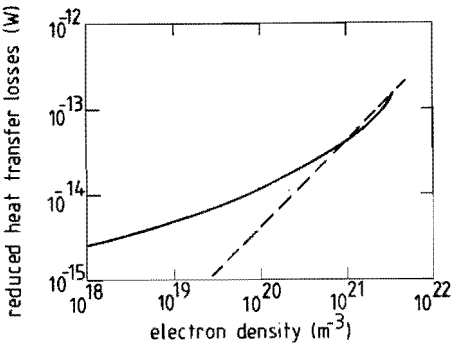

FIG. 4.25. The reduced heat transfer losses caused by collisions of electrons with heavy particles (P_{eh}/n_e) as a function of the electron density at the standard condition for the heavy particles and $\delta b_1 = 0$.

dependence of P_{eh} on δb_1 is again rather small. For $\delta b_1 = 1$ the values of P_{eh} are 9 to 12% higher than for $\delta b_1 = 0$ at the same value of the electron density. This is caused by the higher electron temperature for $\delta b_1 = 1$ than for $\delta b_1 = 0$. In fact P_{eh} is about proportional to $(1 + \delta b_1)^{0.12}$ for all values of n_e. For high values of n_e, P_{eh} is important (e.g. $P_{eh} = -5.23 \times 10^8$ W/m^3 for $n_e = 3.50 \times 10^{21}$ m^{-3} and $\delta b_1 = 0$). Though it depends somewhat on the standard condition and on the radius, P_{eh} is negligible for low values of n_e because of the strong dependence on n_e. Therefore an approximation for P_{eh} which is only accurate for $n_e \geq 5 \times 10^{20}$ m^{-3} will be used (dashed line in Fig. 4.25):

$$P_{eh} = -4.27 \times 10^5 \, (1 + \delta b_1)^{0.12} \, \hat{n}_e^2 \quad \text{W/m}^3 \tag{4.31}$$

Here $\hat{n}_e$ denotes the electron density in 10^{20} m^{-3}.

The electron heat conductivity according to Eq. (2.55) is given in Fig. 4.26 as a function of the electron density. Again the approximations for the cross sections for collisions between electrons and heavy particles as given by Mesland (MES82) have been used. The dependence on the overpopulation of the ground state, δb_1, is again rather small. The values for λ_e are somewhat higher for $\delta b_1 = 1$ than for $\delta b_1 = 0$. The difference is 1.5% for low electron densities and 7.5% for high electron densities. Over the total range of electron densities λ_e is about proportional to $n_e^{0.8}$. The magnitude of the heat conductivity term depends very much on the radius of the filament considered. At the axis this term is (see Subsec. 4.3.1)

$$\nabla \cdot (\lambda_e \nabla T_e) = -\frac{4 \lambda_e T_e}{R_T^2} \qquad (r \ll R_T) \tag{4.32}$$

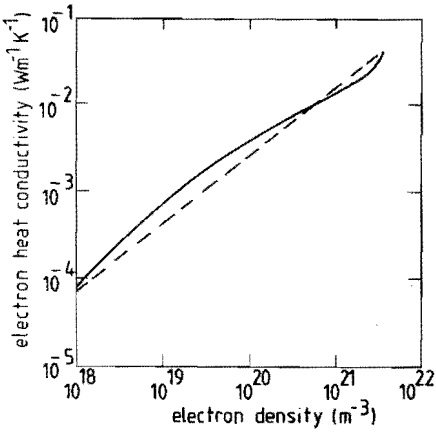

FIG. 4.26. The electron heat conductivity, λ_e, as a function of the electron density at the standard condition for the heavy particles and $\delta b_1 = 0$. The dashed line is the approximation given by Eq. (4.38).

In Eq. (4.32), R_T is the $1/e$ radius of a Gaussian electron temperature profile. The influence of the radius on $\nabla\cdot(\lambda_e \nabla T_e)$ and other terms in the mass and energy balances will be discussed in the next subsection.

The last term in the right-hand side of Eq. (2.58) is the heat production by viscosity. This term has been estimated by Schenkelaars (SCH84) for cylindrical structures with radii in the submillimeter range. The theory as given by Braginskii (BRA65) has been used. This term turns out to be small for all values of the electron density and all radii considered here. Therefore this term is neglected.

4.4.2 *Dependence on the radius*

In the previous subsection the different terms in the right-hand side of Eq. (2.58) have been evaluated. The terms Q^e_R, Q^e_{inel}, P_{eh}, and $\nabla\cdot(\lambda_e \nabla T_e)$ proved to be important. Only the inelastic loss term and the electron heat conductivity term depend on the radius of a filament in different ways. These dependences are analyzed in this subsection.

The radii R and R_n are important in the evaluation of Q^e_{inel}. This term depends on the radius R by means of the escape factor Λ_{21}. The radius R is the distance over which emitted resonance radiation has to travel to leave the plasma. For a radius $R = 10^{-4}$ m this leads to Fig. 4.23. Other values of R will result in similar figures. The overpopulation of the ground level, δb_1, is still a parameter in Fig. 4.23 and has to be determined by the solution of the mass balance given by Eq. (4.29). The radius which occurs in Eq. (4.29) is related to the diffusion and is determined by $(1/n_e)/(\partial^2 n_e/\partial r^2)$ near the axis according

to Eqs. (4.26) to (4.28). To distinguish this radius from the radius R used above it is called R_n. The radii R and R_n need not be the same. The relation between R and R_n can only be found by a numerical evaluation of the solution of the combined balances, which will be given in Sec. 4.5. Here we will assume R that is equal to R_n. In the same way as has been applied in the previous subsection, one can combine the values for δb_1 from the mass balance and the values for Q^e_{inel}/n_e (see Fig. 4.23). The results for different values of the radius R are given in Fig. 4.27. Note that the upper curve in Fig. 4.27 is the same as the dashed curve in Fig. 4.23. The dependence on R and n_e is represented quite well by

$$\left[\frac{Q^e_{inel}}{n_e}\right] = 1.27 \times 10^{-13}\, \hat{n}_e^{-0.2}\, \hat{R}^{-0.7} \quad \mathrm{W/m^3} \tag{4.33}$$

Here $\hat{n}_e$ is the electron density in 10^{20} $\mathrm{m^{-3}}$ and $\hat{R}$ is the radius in 10^{-4} m.

The term $\nabla\cdot(\lambda_e \nabla T_e)$ also depends on the radius of a filament. Like R_n, R_T is defined as the $1/e$ width of a Gaussian approximation of the temperature profile around the axis. More generally, R_n and R_T can be defined by

$$-\frac{1}{n_{e0}}\left[\frac{\partial^2 n_e}{\partial r^2}\right]_0 = \frac{2}{R_n^2} \tag{4.34}$$

and

$$-\frac{1}{T_{e0}}\left[\frac{\partial^2 T_e}{\partial r^2}\right]_0 = \frac{2}{R_T^2} \tag{4.35}$$

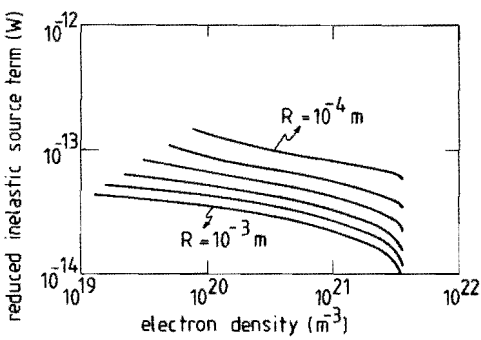

FIG. 4.27. The reduced inelastic source term (Q^e_{inel}/n_e) as a function of the electron density for different values of the radius R. The values for δb_1 resulting from the mass balance for $R_n = R$ have been used. The curves have been calculated for R = 1, 1.6, 2.5, 4.0, 6.3, and 10 × 10^{-4} m (from above downward).

According to the results presented in Fig. 4.21, the overpopulation of the ground level is small and therefore the electron temperature can be written as a function of the electron density only. So

$$\left[\frac{\partial^2 T_e}{\partial r^2}\right] = \frac{\partial}{\partial r}\left[\frac{\partial T_e}{\partial n_e}\frac{\partial n_e}{\partial r}\right] = \left[\frac{\partial T_e}{\partial n_e}\right]\frac{\partial^2 n_e}{\partial r^2} + \frac{\partial n_e}{\partial r}\frac{\partial}{\partial r}\left[\frac{\partial T_e}{\partial n_e}\right]$$

For $r = 0$ this leads to

$$\left[\frac{\partial^2 T_e}{\partial r^2}\right]_0 = \left[\frac{\partial T_e}{\partial n_e}\right]_0 \left[\frac{\partial^2 n_e}{\partial r^2}\right]_0 \qquad (4.36)$$

Combining Eqs. (4.34) to (4.36) gives

$$\frac{2}{R_T^2} = \frac{n_{e0}}{T_{e0}}\left[\frac{\partial T_e}{\partial n_e}\right]_0 \frac{2}{R_n^2}$$

The ratio between R_n and R_T, which is plotted in Fig. 4.28 as a function of the electron density, is given by

$$\frac{R_n}{R_T} = \left[\frac{n_{e0}}{T_{e0}}\left[\frac{\partial T_e}{\partial n_e}\right]_0\right]^{1/2} \qquad (4.37)$$

The ratio R_n/R_T is 0.3 to 0.4 for electron densities below 10^{21} m^{-3}. For larger electron densities R_n/R_T increases very fast especially for $n_e > 3 \times 10^{21}$ m^{-3}. This is caused by the fact that the cesium is almost fully ionized (for $n_e = 3 \times 10^{21}$ m^{-3} the degree of ionization is 80%). For high electron densities the radial profile of the electron density is much flatter than that of the electron temperature. The flattening of the electron density profile leads to a diminished diffusion and hence to a smaller value for deviation from equilibrium. The numerical approximation for Q^e_{inel} given by Eq. (4.33) is an upper limit because R_n is taken equal to R.

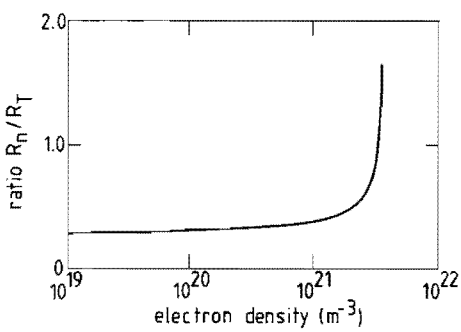

FIG. 4.28. The ratio R_n/R_T as a function of the electron density at the standard condition for the heavy particles and $\delta b_1 = 0$.

The electron heat conductivity λ_e is approximated fairly well by

$$\lambda_e \approx 2.50 \times 10^{-3}\ \hat{n}_e^{0.8}\ \frac{W}{mK} \tag{4.38}$$

The term $\nabla\cdot(\lambda_e \nabla T_e)$ is for $r \ll R_T$ approximated by

$$\frac{4\lambda_e T_e}{R_T^2} = 1.00 \times 10^9\ \frac{\hat{n}_e^{0.8}\ \hat{T}_e}{\hat{R}_T^2}\ W/m^3 \tag{4.39}$$

Here $\hat{T}_e$ is the electron temperature in 10^3 K and $\hat{R}_T$ is the radius R_T in 10^{-4} m. Equations (4.33) and (4.39) are used to estimate the relative importance of the terms Q^e_{inel} and $\nabla\cdot(\lambda_e \nabla T_e)$. There ratio, α, is given by

$$\alpha = \frac{1.27 \times 10^{-2}}{\hat{T}_e}\ \frac{\hat{R}_T^2}{\hat{R}_n^{0.7}} \tag{4.40}$$

For high values of the electron density $\hat{R}_n \geq \hat{R}_T$ and $\hat{T}_e$ is 4 to 5. As will be shown in the next subsection this is the important parameter range. This leads to

$$\alpha \leq 3 \times 10^{-3}\ \hat{R}_T^{1.3}$$

The radius $\hat{R}_T$ considered here is smaller than 10 and therefore Q^e_{inel} can be neglected. So the energy balance mainly depends on the radius by means of the electron heat conductivity term $\nabla\cdot(\lambda_e \nabla T_e)$.

4.5 The combined balances for the electrons

In the previous sections the mass balance for the electrons has been considered separately. Only in the evaluation of Q^e_{inel}, which appears in the right-hand side of the energy balance, the results of the mass balance have been used. In this section also the left-hand side of the energy balance will be considered. Substitution of the mass balance in a rewritten version of the energy balance leads to one equation which describes the non-stationary behaviour of the electrons. The analysis of this equation on the axis of a cylindrical structure leads to a condition for a stable solution of this equation. Numerical results, including the behaviour off axis will be presented.

We start with the left-hand side of the energy balance for the electrons (*LHS*) as given by Eq. (2.58):

$$LHS \equiv \frac{\partial}{\partial t}\left(\frac{3}{2} n_e k T_e\right) + \nabla\cdot\left(\frac{3}{2} n_e k T_e \mathbf{w}_e\right) + n_e k T_e \nabla\cdot\mathbf{w}_e \tag{4.41}$$

This identity is rewritten to

$$LHS \equiv \frac{3}{2} kT_e \frac{\partial n_e}{\partial t} + \frac{3}{2} n_e \frac{\partial}{\partial t}(kT_e) + \frac{5}{2} kT_e \nabla\cdot(n_e \mathbf{v}_e)$$

$$+ \frac{3}{2} n_e \mathbf{v}_e \cdot \nabla kT_e - kT_e \mathbf{v}_e \cdot \nabla n_e \qquad (4.42)$$

Now the mass balance for the electrons as given by Eq. (2.1) is rewritten:

$$\nabla\cdot(n_e \mathbf{v}_e) = \left[\frac{\partial n_e}{\partial t}\right]_{CR} - \frac{\partial n_e}{\partial t} \qquad (4.43)$$

Substituting Eq. (4.43) in Eq. (4.42) gives

$$LHS \equiv \frac{3}{2} n_e \frac{\partial}{\partial t}(kT_e) - kT_e \frac{\partial n_e}{\partial t} + \left[\frac{\partial n_e}{\partial t}\right]_{CR} \times \frac{5}{2} kT_e$$

$$+ \frac{3}{2} n_e \mathbf{v}_e \cdot \nabla(kT_e) - kT_e \mathbf{v}_e \cdot \nabla n_e \qquad (4.44)$$

The last two terms in Eq. (4.44) are zero on the axis of a cylindrical structure. The third term is algebraic and is shifted to the right-hand side of the equation. Furthermore we will use that according to Subsec. 4.3.2 the overpopulation of the ground level is small. Consequently the electron temperature is a function of the electron density only and the term $\partial(kT_e)/\partial t$ can be replaced by

$$k \frac{\partial T_e}{\partial n_e} \frac{\partial n_e}{\partial t}$$

This results in the following combined mass and energy balance of the electrons:

$$\left[\frac{3}{2} n_e \frac{\partial T_e}{\partial n_e} - T_e\right] k \frac{\partial n_e}{\partial t}$$

$$= Q_R^e + P_{eh} + \nabla\cdot(\lambda_e \nabla T_e) - \left[\frac{\partial n_e}{\partial t}\right]_{CR} \times \frac{5}{2} kT_e \qquad (4.45)$$

From here on f will be used for the factor preceding $\partial n_e/\partial t$ in Eq. (4.45) and Q_T for the total energy gain for the electrons which is given by right-hand side of Eq. (4.45). This leads to

$$f \frac{\partial n_e}{\partial t} = Q_T \qquad (4.46)$$

Note that under the assumptions made above f depends only on n_e and Q_T

depends on n_e, the radius and slightly on δb_1. A stationary solution of Eq. (4.46) is given by

$$Q_T = 0 \tag{4.47a}$$

$$f \neq 0 \tag{4.47b}$$

For a stationary solution to be stable also the following equation has to be valid:

$$\frac{\partial}{\partial n_e}\left[\frac{Q_T}{f}\right]_{Q_T=0} < 0 \tag{4.48}$$

This condition can be rewritten to

$$\frac{\partial}{\partial n_e}\left[\frac{Q_T}{f}\right]_{Q_T=0} = \frac{1}{f}\left[\frac{\partial Q_T}{\partial n_e}\right]_{Q_T=0} - \frac{Q_T}{f^2}\left[\frac{\partial f}{\partial n_e}\right]_{Q_T=0}$$

The second term in the right-hand side of this equation is zero according to Eqs. (4.47a) and (4.47b). Note that $(\partial f/\partial n_e)$ is finite for all values of n_e. So Eq. (4.48) can be replaced by

$$\frac{1}{f}\left[\frac{\partial Q_T}{\partial n_e}\right]_{Q_T=0} < 0 \tag{4.49}$$

The term Q_T contains one positive term viz. Q_R^e and three negative terms viz. P_{eh}, $\nabla\cdot(\lambda_e \nabla T_e)$, and $-(\partial n_e/\partial t)_{CR} \times (5/2)kT_e$. The terms P_{eh} and $-(\partial n_e/\partial t)_{CR} \times (5/2)kT_e$ will be compared with $\nabla\cdot(\lambda_e \nabla T_e)$ for high electron densities. This will give an upper limit for the importance of these terms.

The ratio β of the terms P_{eh} and $\nabla\cdot(\lambda_e \nabla T_e)$ at the axis is obtained from Eqs. (4.31) and (4.39):

$$\beta = \frac{4.27 \times 10^{-4}\ (1 + \delta b_1)^{0.12}\ \hat{n}_e^{1.2} \hat{R}_T^2}{\hat{T}_e} \tag{4.50}$$

β reaches its maximum value for high electron densities. We will use $\hat{n}_e = 36.2$ (fully ionized seed). Then $(1 + \delta b_1)^{0.12}$ is about 1 and $\hat{T}_e$ is between 4 and 5 so an upper limit for β is given by

$$\beta \leq 7.9 \times 10^{-3}\ \hat{R}_T^2 \tag{4.51}$$

Therefore P_{eh} is negligible except for values of $\hat{R}_T \geq 5$.

The ratio γ of the term $(\partial n_e/\partial t)_{CR} \times (5/2)kT_e$ and $\nabla\cdot(\lambda_e \nabla T_e)$ is at the axis given by

$$\gamma \approx \frac{3.45\ (\nu_1 \delta b_1 - \nu_0)\ \hat{n}_e \hat{T}_e}{1.00 \times 10^9\ \hat{n}_e^{0.8} \hat{T}_e\ \hat{R}_T^{-2}}$$

$$= 3.45 \times 10^{-9}\ (\nu_1 \delta b_1 - \nu_0)\ \hat{n}_e^{0.2}\ \hat{R}_T^2 \qquad (4.52)$$

For high electron densities and for 10^{-4} m $\leq R_n \leq 10^{-3}$ m the values for ν_1, ν_0, and δb_1 are given in the Figs. 4.18, 4.20, and 4.21 respectively. The total production frequency $\nu_1 \delta b_1 - \nu_0$ varies between 3×10^4 s^{-1} for $R = 10^{-3}$ m and 3×10^5 s^{-1} for $R = 10^{-4}$ m. An upper limit for γ is given by

$$\gamma \leq 1.10 \times 10^{-3}\ \hat{n}_e^{0.2}\ \hat{R}_T^2 \qquad (4.53)$$

So $\gamma \leq 0.1$ for the parameter range considered here Therefore the term $(\partial n_e/\partial t)_{CR} \times (5/2)kT_e$ is negligible except for values of $\hat{R}_T \geq 5$.

For the analysis of the condition given by Eq. (4.49) we will use

$$Q_T = \sigma E^2 + \nabla\cdot(\lambda_e \nabla T_e)$$

The electrical conductivity σ can be approximated by

$$\sigma \approx 7.21 \times 10^1\ \hat{n}_e^{0.645}\ \mathrm{AV^{-1}m^{-1}}$$

With the electrical field $\hat{E}$ in 10^3 V/m this leads to

$$\sigma E^2 \approx 7.21 \times 10^7\ \hat{E}^2\ \hat{n}_e^{0.645}\ \ \mathrm{W/m^3} \qquad (4.54)$$

The term $\nabla\cdot(\lambda_e \nabla T_e)$ is for $r \ll R_T$ approximated by Eq. (4.39). Combining Eqs. (4.39) and (4.54) leads to the following approximation for Q_T near the axis:

$$\left[Q_T\right]_{r \ll R_T} = 7.21 \times 10^7\ \hat{E}^2 \hat{n}_e^{0.645} - \frac{1.00 \times 10^9\ \hat{n}_e^{0.8} \hat{T}_e}{\hat{R}_T^2} \qquad (4.55)$$

For fixed values of $\hat{E}$ and $\hat{R}_T$ the derivative

$$\left[\frac{\partial Q_T}{\partial n_e}\right]_{Q_T=0}$$

is negative. This is because the exponent of $\hat{n}_e$ in the second term of the right-hand side of Eq. (4.55) is larger than that of the first term. Moreover $\hat{T}_e$ also increases with $\hat{n}_e$. Because the exponents depend

on the approximations used for σ and λ_e, these two quantities are plotted in Fig. 4.29. The electron density varies between 10^{18} m^{-3} and 3.6×10^{21} m^{-3}. The slope of the curve in Fig. 4.29 is for all values of the electron density smaller than 1. Therefore the conclusion that

$$\left[\frac{\partial Q_T}{\partial n_e}\right]_{Q_T=0}$$

is negative for $r \ll R_T$ is not a consequence of the approximations made above. So the condition for a stable solution as given by Eq. (4.49) can be replaced by the condition $f > 0$.

The function $f = [(3/2)n_e(\partial T_e/\partial n_e) - T_e)k]$ is drawn in Fig. 4.30 as a function of the electron density. For electron densities smaller than about 3×10^{21} m^{-3}, f is negative and for electron densities greater than 3×10^{21} m^{-3}, f is positive. So for a stable solution of

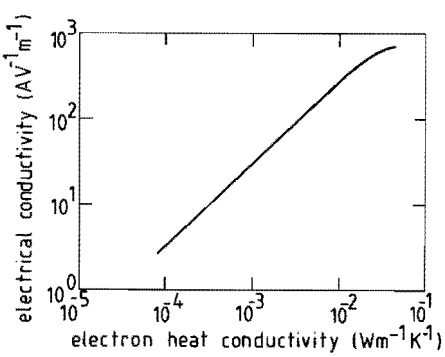

FIG. 4.29. The electrical conductivity versus the electron heat conductivity at the standard condition for the heavy particles. The electron density varies between 10^{18} m^{-3} and 3.6×10^{21} m^{-3}. The dependence on δb_1 is very small and the relation between σ and λ_e is covered by one curve for all values of δb_1 between 0 and 1.

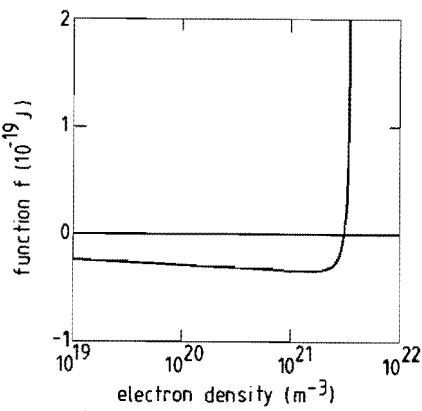

FIG. 4.30. The function f versus the electron density at the standard condition for the heavy particles.

Eq. (4.45) the electron density has to be larger than 3×10^{21} m^{-3} (more than 86% of the cesium is ionized). The corresponding minimum electron temperature is about 4300 K. The value of the electron density at which $f = 0$ depends only on the total cesium density n_{Cs}. For values of n_{Cs} between 5×10^{20} m^{-3} and 5×10^{21} m^{-3} the degree of ionization at $f = 0$ varies between 88% and 85%.

So far only the combined balances near the axis of a filament have been considered. The solution off the axis is given by

$$\sigma E^2 + \frac{1}{r}\frac{\partial}{\partial r}\left[r\lambda_e \frac{\partial T_e}{\partial r}\right] = 0 \qquad (4.56)$$

Because the overpopulation of the ground level is small the equilibrium relation between n_e and T_e is used. The differential equation given by Eq. (4.56) is numerically integrated starting at $r = 0$. The initial conditions are the electron temperature at the axis T_{e0} and the condition that $\partial T_e/\partial r = 0$ for $r = 0$ which is a consequence of the cylindrical geometry. The results for $T_{e0} = 5000$ K and $T_{e0} = 4300$ K are given in Figs. 4.31 and 4.32 respectively. The profiles are nor-

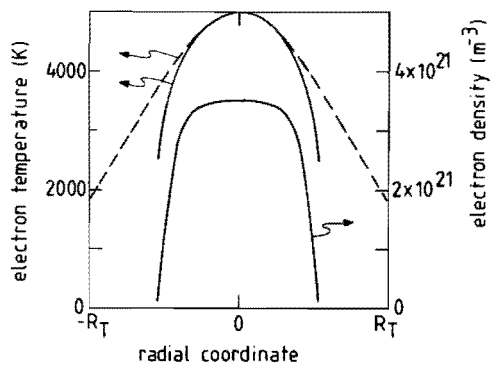

FIG. 4.31. The calculated electron temperature and electron density profiles (solid curves) as a function of the radial distance for an electron temperature at the axis of 5000 K. For the heavy particles the standard condition (T_h = 1000 K, $p = 5 \times 10^4$ Pa, and SF $=10^{-3}$) has been used. The profiles are normalized in the radius with respect to R_T. The corresponding Gaussian profile for the electron temperature is given by the dashed curve.

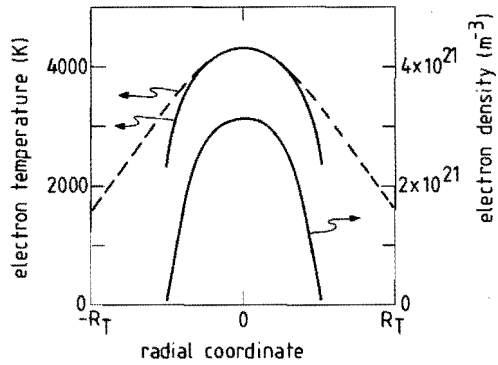

FIG. 4.32. The calculated electron temperature and electron density profiles (solid curves) as a function of the radial distance for an electron temperature at the axis of 4000 K. For the heavy particles the standard condition (T_h = 1000 K, p = 5 × 10^4 Pa, and SF = 10^{-3}) has been used. The profiles are normalized in the radius with respect to R_T. The corresponding Gaussian profile for the electron temperature is given by the dashed curve.

malized in the radius with respect to R_T. The electrical field is chosen to fulfill Eq. (4.56) for r = 0. The numerical solution is given by solid curves in both figures. For comparison also Gaussian electron temperature profiles with the same values of E and R_T are given (dashed curves). This profile has been used to estimate the electron heat conductivity at the axis. The electron temperature profile resulting from Eq. (4.56) falls off much faster because the electron heat conductivity decreases rapidly. Consequently the actual $1/e$ width of the electron temperature profile is smaller than R_T. For high values of the electron density the corresponding profile is flattened in the middle because the cesium is almost fully ionized (Fig. 4.31). For lower values of the electron density the decrease appears much faster (Fig. 4.32). This corresponds with the ratio between R_n and R_T as given in Fig. 4.28. For the electron profile the actual $1/e$ width is smaller than the radius R_n. The calculated (half) $1/e$ width of the electron density profile will be called Lx as in Chapter 5 where an experimental determination of Lx is described.

Throughout the calculation of the profiles, δb_1 is assumed to be zero. From the estimates given above it follows that $\delta b_1 \ll 1$ in the middle of the profile. At the sides of the profile this is not necessarily the case. An overpopulation of the ground level leads to lower values for the electron density at the same electron temperature. On the other hand the electron temperature gradient will be smaller and the electron temperature itself will be smaller when the inelastic energy loss gets important. Consequently the electron density profile is not very much influenced by the assumption that $\delta b_1 = 0$. Moreover the profile is rather steep at the sides and the resulting error in the calculated value of *Lx* is small. The steepness of the profile is also the reason to stop the numerical integration when the electron density becomes smaller than 2×10^{20} m^{-3}. For lower values of the electron density the computing time needed to get a reasonable accuracy is very large. In addition the *1/e* width of the electron density profile *Lx* is already determined.

From the calculation of the profiles as shown in Figs. 4.31 and 4.32 a value for the product *ExLx* results. *ExLx* is between 0.38 and 0.53 V for electron densities greater than 3×10^{21} m^{-3}. The corresponding electron temperatures are greater than 4300 K. When for *Lx* the experimental value of 1.3×10^{-4} m is used (see Chapter 5) values between 3000 and 4000 V/m are found for the electrical field. The corresponding current density at the axis of the filament varies between 1.8×10^{6} and 4.5×10^{6} A/m^2. The averaged current density (total current through a filament divided by πLx^2) is 3.0×10^{5} A/m^2 for $n_e = 3 \times 10^{21}$ m^{-3} and 4.5×10^{5} A/m^2 for $n_e = 3.5 \times 10^{21}$ m^{-3}. This agrees rather well with values resulting from line emission and continuum emission measurements with a partial resolution of a few millimetres (WET84).

4.6 Conclusions

A theoretical description of the filaments observed in the Ar–Cs plasma of a closed cycle MHD generator is given. The mass and energy balances for the electrons in a filament with a radius between 0.1 and 1 millimetre are analysed for a specific condition for the heavy particles (T_h = 1000 K, $p = 5 \times 10^{4}$ Pa, and $SF = 10^{-3}$). The overpopulations of the excited levels and the source term in the mass balance

(ionization and recombination) are evaluated by means of a collisional radiative (CR) model for the neutral cesium system. The overpopulation of excited level q is given in the form $\delta b_q = r_q \delta b_1 + \rho_q$, in which r_q and ρ_q depend on the electron temperature, the escape of resonance radiation, and the number of levels taken into account. The source term in the mass balance is given by $n_e(\upsilon_1 \delta b_1 - \upsilon_0)$, in which υ_1 and υ_0 depend on the same quantities. Different broadening mechanisms of resonance lines are considered (Doppler, Stark, Resonance, and Van der Waals broadening). The Van der Waals broadening is dominant. Therefore the escape of resonance radiation depends mainly on the temperature and the density of the heavy particles. The excited levels can be divided in groups. The overpopulations of the different levels of a group are about equal to each other. A CR model with 10 levels suffices to obtain a good description of the deviation from equilibrium and the resulting non-equilibrium ionization. The filament radius is important because it determines the escape of resonance radiation. This analysis yields small deviations from equilibrium, even at the small radii considered. A number of source terms in the energy balance have been analysed. The ohmic dissipation and the electron heat conductivity constitute the most important terms close to the axis of the filament. The combined balances close to the axis yield that a stable stationary solution is only possible for electron densities greater than 3×10^{21} m^{-3} and electron temperatures greater than 4300 K (85% of the cesium has to be ionized). Using the measured value of the radius of the electron density profile results in electric fields between 3000 and 4000 V/m and current densities averaged over a filament of 3.0×10^5 to 4.5×10^5 A/m^2. These values correspond well with values obtained by others from measurements of line and continuum emission.

Collective CO_2 laser scattering on moving discharge structures in the submillimeter range in a magnetohydrodynamic generator

J. C. M. de Haas, H. J. W. Schenkelaars, P. J. van de Mortel, D. C. Schram, and A. Veefkind[a)]

Eindhoven University of Technology, Department of Physics, P. O. Box 513, 5600 MB Eindhoven, The Netherlands

(Received 15 August 1985; accepted 14 January 1986)

Collective scattering of CO_2 laser light on electrons is used to determine the radial scale length of the discharge structures occurring in a closed cycle magnetohydrodynamic generator. Heterodyne detection of scattered radiation is used to obtain a spatial resolution in the submillimeter range and to increase the signal to noise ratio. A discharge model is formulated to interpret the measured signals. The scale length of the electron density fluctuations is found to be $(2.5 \pm 0.5) \times 10^{-4}$ m.

I. INTRODUCTION

Collective scattering of CO_2 laser light is a technique commonly employed to study electron density fluctuations, e.g., in tokamak and arc plasmas.[1-5] In the present experiment the technique is used to determine the scale length of the discharge structures occurring in a magnetohydrodynamic (MHD) generator. In a MHD generator an electrically conductive gas flows through a channel, positioned in a strong magnetic field perpendicular to the flow direction of the gas. Because of the Lorentz forces, electrons and ions are separated and an electric field E is generated in the channel (Fig. 1). When electrodes are installed to collect the current, the electric power can be supplied to an external load. In the case when alkali seeded noble gases are used as the active medium of the generator, an inhomogeneous discharge structure is observed. Measurements with low spatial resolution show that the current is concentrated in discharges with a diameter of 2 to 6 cm, the so-called streamers.[6] Fast photography with better resolution shows the existence of substructures of much smaller dimension (called filaments) in the streamer. In order to determine the scale length of these filaments collective CO_2 laser scattering is used in the present experiments.

In our case the gas flow (cesium seeded argon) is generated by a shock tube. Stationary flow conditions can be obtained for intervals up to 5 msec. After the reflection of the shock at the end of the tube, a small part of the gas passes through a nozzle into a diverging channel. Important parameters are listed in Fig. 1.

II. THE HETERODYNE MIXING TECHNIQUE

Collective scattering of CO_2 laser radiation by electrons is used to study the plasma fluctuations. Mixing of the scattered radiation by heterodyne detection, using a part of the incident beam as local oscillator, increases the sensitivity by several orders of magnitude. Another important effect of the mixing is the interference caused by the phase difference of the scattered and the local oscillator radiation (the scattered and the local oscillator radiation have the same frequency). The scattered and local oscillator beams are aligned so that in the detection volume in the plasma an interference pattern is effectively obtained with fringes almost parallel with the yz plane (Fig. 2). An interference signal can be measured when an electron density perturbation moves through the fringes. The k spacing of the interference pattern can be changed by varying the angle between the incident and the scattered beam. Although the neutral particle density is three to four orders of magnitude higher than the electron density, the Rayleigh scattering by argon atoms can be neglected because of the long wavelength of the radiation used. The ratio of the Rayleigh cross section for argon to the Thomson cross section is 2.5×10^{-8}.

Since the characteristic scale length of the interference pattern is much larger than the Debye length, only collective phenomena are observed. A sketch of the experimental setup

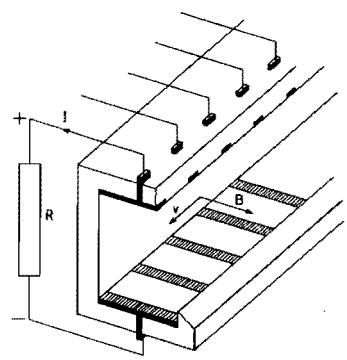

FIG. 1. The MHD generator channel. Important parameters are the magnetic field $B = 3$ T, flow speed $v = 1000$ m/sec, gas temperature 1000 K, pressure 5×10^4 Pa, main gas Argon, Cesium seed fraction 2/1000, channel cross section in the middle 8×11 cm, channel length 80 cm, and channel divergence 2° for left and right wall.

[a)] Department of Electrotechnical Engineering.

 0031-9171/86/051725-06$01.90 © 1988 American Institute of Physics

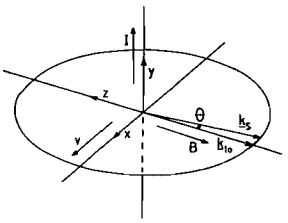

FIG. 2. The scattering geometry in the detection volume. Here $\mathbf{k}_s$ is the propagation vector of the scattered beam, $\mathbf{k}_{lo}$ the propagation vector of the local oscillator, and θ the scattering angle.

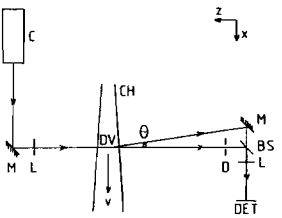

FIG. 3. The experimental setup; C = laser, M = mirror, L = lens, CH = channel, DV = detection volume, D = diaphragm, BS = beamsplitter, and DET = detector.

is presented in Fig. 3.

The CO_2 laser is operated in one single longitudinal TEM mode. The laser beam, with a wavelength of 10.6 μm, passes the channel through flush mounted ZnSe windows with antireflection coatings. A diaphragm is used to adjust the local oscillator power. A secondary effect of the diaphragm is that at the detector surface the local oscillator is not a Gaussian beam. It is, however, calculated that the antenna condition[1] remains fulfilled. A helium cooled Ge:Cu photoconductive detector is used. The signal is processed by means of high pass filters and two broad band amplifiers (total gain G) and is eventually stored in an 8 k-transient recorder with a maximum sampling rate of 32 MHz.

III. THEORY

In this paper we use the analysis of Holzhauer and Massig.[7] They determine the detector current caused by a specified electron density perturbation and the electric field pattern of the radiation in the detection volume by calculating backwards along the optical path from the detector to the detection volume. In this way the interference at the detector is projected in the detection volume. For the electron density distribution we assume a cylindrical Gaussian profile, moving with a velocity v through the detection volume (Fig. 2):

$$n_e = n_{e0} \exp[-(x - vt)^2/Lx^2 - z^2/Lz^2], \tag{1}$$

where Lx and Lz are half the $1/e$ widths of the Gaussian electron density profile in the x and z directions, respectively. Using Gaussian profiles simplifies the calculation and gives a clear relationship between the scale length and the scattered signal. Substitution of the assumed profile in the formalism of Holzhauer and Massig[7] leads to the following expression for the interference term of the detector current:

$$i_{if}(t) = j\lambda_i \frac{\eta e}{h\nu} r_0 m \underbrace{\frac{2(P_s \times P_{lo})^{1/2}}{\pi La^2}}_{\mathrm{A}} \int dr^3 \Big[\underbrace{n_{e0} \exp\Big(-\frac{(x-vt)^2}{Lx^2} - \frac{z^2}{Lz^2}\Big)}_{\mathrm{B}} \underbrace{\exp\Big(-\frac{(x^2+y^2)}{La^2}\Big)}_{\mathrm{C}} \times \underbrace{[\exp(jkx) - \exp(-jkx)] \times \exp j\Delta\phi}_{\mathrm{D}} \Big], \tag{2}$$

where j represents the imaginary unit, λ_i the laser wavelength (10.6 μm), $\eta e/h\nu$ the detector responsivity, r_0 the classical electron radius, m the mixing efficiency, P_s the incident scattered laser power, P_{lo} the local oscillator power, La the laser beam radius [$(1/e)^2$ intensity drop], $k = |\mathbf{k}| = |\mathbf{k}_{lo} - \mathbf{k}_s|$ (Fig. 2), and $\Delta\phi$ the phase difference between local oscillator and scattered power.

In Eq. (2), A describes the power density of the interference part of the signal, B describes the electron density profile moving through the detection volume, C describes the intersection of the local oscillator with the scattered beam, determining the detection volume, and D describes the interference pattern in the detection volume. Note that k is the inverse scale length of the interference pattern. In this term the wave vector $\mathbf{k}$ is assumed to be parallel to the x direction. For a fixed laser wavelength k is a function of the scattering angle Θ only. For a wavelength of 10.6 μm and $\Theta < 30°$ we obtain $k = 10^4 \Theta m^{-1}$ with Θ in degrees. It is clear that the diagnostic is resonant for waves with wave vectors close to $\mathbf{k}$. For moving density perturbations the diagnostic is only sensitive for perturbations with scale lengths less than or equal to π/k. In other words, in this setup the method provides a spatial filter. Carrying out the integrations in Eq. (2) gives

$$i_{if} = C_{opt} n_{e0} LzLa(\pi^{3/2}/p) \exp[-(k^2/4p^2)] \times \exp[-(vt/Lg)^2] \times \sin\{kvt/[1 + (Lx/La)^2]\} \exp(j\Delta\phi), \tag{3}$$

where

$$C_{opt} = 2\lambda_i(\eta e/h\nu) r_0 m [2(P_s P_{lo})^{1/2}/\pi La^2],$$
$$p^2 = 1/Lx^2 + 1/La^2,$$
$$Lg^2 = Lx^2 + La^2.$$

The detector voltage can be written as

TABLE I. The corrections of the high pass filter for some values of the scattering wavenumber.

k (m^{-1})	$C_{hl}(k)$
5.42×10^3	1.3
9.97×10^3	1.1
$>14.2\times10^3$	1.0

$$v_{if}(t) = G\times Rl\times C_{hl}(k)\times i_{if}(t), \tag{4}$$

where G represents the gain of the amplifiers, Rl the load resistance, and $C_{hl}(k)$ the correction function for the high pass filter (Table I). In the following expressions the detector voltage is divided by this correction function. These corrected voltages are represented by $v_{if}(k,t)$. By substituting $P_s = 0.52$ W (1.5 W with a transmission of 35%), $P_{so} = 1.4\times10^{-3}$ W, $La = 2\times10^{-3}$ m, $m = 0.7$, $\eta e/h\nu = 0.10$ A/W, $G = 350$, and $Rl = 600\ \Omega$ we get[1]

$$v_{if}(k,t) = 2.9\times10^{-14}n_{e0}\frac{Lz}{p}\exp\left(-\frac{k^2}{4p^2}\right)\exp\left[-\left(\frac{vt}{Lg}\right)^2\right]\times\sin\left(\frac{kvt}{1+(Ln/La)^2}\right)\exp(j\Delta\phi)\ \text{V} \tag{5}$$

(all constants in this and the following equations are in SI units). This signal is the product of a sine function with constant frequency and a Gaussian function. The most interesting feature, however, is the exponential decay with k^2. If the signals are measured for different values of k, Lx can be determined. Thus we only have to compare the values of the peaks of the Gaussian envelopes as a function of k:

$$v_{if}(k,t=0) = 2.9\times10^{-14}n_{e0}\frac{Lz}{p}\exp\left(-\frac{k^2}{4p^2}\right)\text{V}. \tag{6}$$

If $Lx \ll La$, which applies for these experiments, this equation simplifies to

$$v_{if}(k,t=0) = 2.9\times10^{-14}n_{e0}LxLz\exp(-k^2Lx^2/4)\ \text{V}. \tag{7}$$

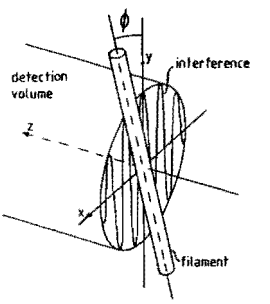

FIG. 4. The filament inclination.

All this however is only valid provided the signals caused by the individual filaments do not overlap. If the signals of N different filaments overlap, we obtain

$$v_{if}(k,t=0) = 2.9\times10^{-14}N^{1/2}n_{e0}LxLz\times\exp(-k^2Lx^2/4)\ \text{V}. \tag{8}$$

Another problem is the strong dependence of the signal on the angle of the filament with the yz plane. When a filament crosses the yz plane at an angle ϕ, it simultaneously crosses different fringes (Fig. 4), giving positive and negative contributions to the signal at the same time. This leads to a significant decrease of the signal. The reduction of the signal caused by this effect can be calculated by rotating the cylindrical electron density profile of Eq. (1) in the xy plane over an angle of ϕ:

$$n_e = n_{e0}\exp\left(-\frac{[(x-vt)\cos\phi + y\sin\phi]^2}{Lx^2} - \frac{z^2}{Lz^2}\right). \tag{9}$$

Substitution of this distribution in the expression of Holzhauer and Massig and again carrying out the integration gives

$$v_{if}(k,t,\phi) = 2.9\times10^{-14}n_{e0}(Lz/p)\exp[-(vt\cos\phi/Lg)^2]\exp(-k^2/4p^2)\times\exp\{-La^2\sin^2\phi\,k^2/[4(1+(Lx/La)^2]\}\sin\{kvt\cos^2\phi/[1+(Lx/La)^2]\}\ \text{V}. \tag{10}$$

At $t = 0$ and with $Lx \ll La$ this simplifies to

$$v_{if}(k,t=0,\phi) = 2.9\times10^{-14}n_{e0}LxLz\times\exp(-k^2Lx^2/4)\times\exp[-(k^2/4)La^2\sin^2\phi]\ \text{V}. \tag{11}$$

IV. EXPERIMENTAL RESULTS

Measurements are carried out for four different values of k (Table II). These k values have been measured with the aid of Rayleigh scattering on acoustic waves generated by a ceramic crystal in argon at 1 bar. Simultaneously with the scattering measurement a Cs neutral line intensity is measured 7.85 cm downstream in the channel, so that a correlation between the two signals can be carried out. In Fig. 5 the scattering signal (a) and the line intensity signal (b), measured simultaneously at different positions, are presented. A careful study of this figure and similar ones shows that the scattering signal has its maxima when a streamer enters and when it leaves the detection volume. This feature will be used in formulating a streamer model. The line intensity signal has been drawn shifted in time to show the correlation with the scattering signal. The involved time difference is

TABLE II. The limiting angles as a function of the scattering wavenumber.

	k (m^{-1})	ϕ_0(°)
(a)	5.42×10^3	7.5
(b)	9.97×10^3	4.0
(c)	14.28×10^3	2.8
(d)	22.05×10^3	1.8

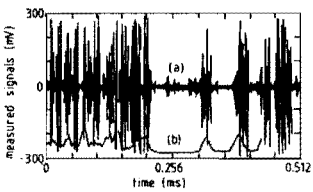

FIG. 5. The correlation of the scattering signal (a) and the line intensity signal (b). The line intensity signal is shifted to correct for the time difference caused by the distance between the measuring sites.

7.5×10^{-5} sec. The distance between the two diagnostics and this time difference lead to a velocity of the streamer of 1050 m/sec. This is in agreement with other experiments in which the time delay between two line emission signals is measured along two parallel axes perpendicular to the flow direction.[6] The velocities derived from these experiments were between 950 and 1100 m/sec. In Fig. 6, four scattering measurements for different k values are presented. Note the strong decrease of the magnitude of the signal with increasing k. The time duration for a filament to cross the detection volume is given by $2Lg/v$ [see Eq. (3)]. If $Lx \ll La$, this can be replaced by $2La/v$. With $La = 2.0\times10^{-3}$ m and

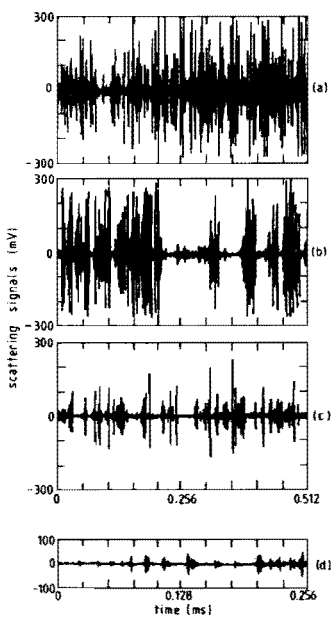

FIG. 6. The scattering signals (values of the wavenumber corresponding to Table II).

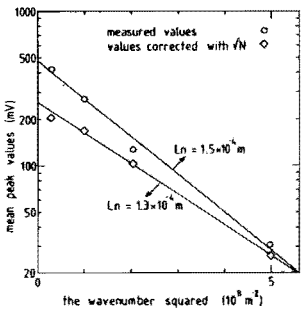

FIG. 7. The mean peak values of the scattering signals corrected for the high pass filter.

$v = 1050$ m/sec this time is 3.8×10^{-6} sec. The time duration of a burst in the scattering signal corresponding to one streamer is about five times as large. Enlargement of the signal of a burst shows a sinusoidal signal with jumps in phase. This means that the bursts in the scattering signals are caused by several filaments and that the signals of the individual filaments may overlap especially at lower k's. For larger scattering k values, the selectivity in inclination angle is better and the chance of overlap is smaller. By neglecting the effect of overlap, a first estimate of the scale length of the filaments can be determined by plotting the mean peak value of each scattering signal logarithmically against k^2 as is done in Fig. 7. The scale length is determined by the slope. The result is that $Lx = 1.5\times10^{-4}$ m. The magnitude of the scattering signal is influenced by overlap of the signals of individual filaments and because the axes of the filaments are not parallel to the interference pattern. These effects will be estimated by using a streamer model.

V. THE STREAMER MODEL

To investigate the scattered signal caused by a number of filaments clustered together in a streamer, a computer model has been used. The maximum scattering at entering and leaving of the detection volume by a streamer can be simulated through the assumption of a large number of filaments twisted into a helix structure: the filaments at the front and back of a streamer (related to the flow) have no inclination in the xy plane, contrary to the filaments at the sides (Fig. 8). As a consequence the scattered signal will be diminished when the center of the streamer passes the detection volume. This model of filament structure is supplied by the photographs made with the high speed camera, where indeed a helix structure can be recognized.[6] The effect will be somewhat enhanced when there are fewer filaments in the inner part of the streamer. For the model some assumptions have to be made. Based on the mentioned photographs, a streamer radius is used of 1×10^{-2} m and a spiraling angle increasing linearly with r and a value of 20° at the outside of the streamer. Measured averaged streamer properties have been translated to properties of a streamer consisting of a number of filaments.[6] The results yield a number between 10

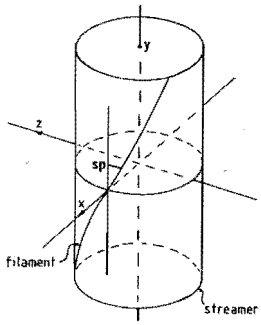

FIG. 8. The helix structure of the streamers; sp = spiraling angle.

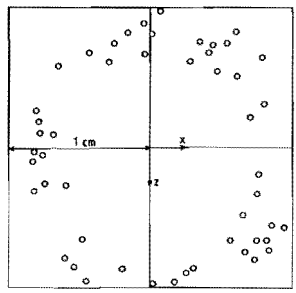

FIG. 10. The filament distribution in a streamer simulation.

and 100. Here 50 will be used. The characteristic radius of all these filaments is assumed to be the same (1.3×10^{-4} m). Finally no filaments are allowed in the center of the streamer in agreement with the observation that the scattering signal has maxima when a streamer enters and leaves the detection volume. This last assumption will not have a large influence on the results of the model because the area in the center is relatively small.

To obtain an estimation of the effects on the total signal we will make a calculation in which, for simplicity, only those filaments are taken into account that fulfill

$$\exp[-(k^2/4)La^2\sin^2\phi] > \exp(-0.5)$$

[compare Eq. (7)]. This means that the inclination angle of a filament has to fulfill

$$\phi < \arcsin(700/k).$$

This results in a limiting angle for each k value as shown in Table II.

If we assume the filaments to be distributed as described above we can calculate how many filaments are seen simultaneously as a function of time when a streamer passes the detection volume. The results are presented in Fig. 9. Complete signals are calculated by computer simulation as follows. First, filaments are randomly distributed over the streamer. The distance between two filaments is at least one filament diameter (Fig. 10). Afterward, the spiraling angles and the angles of the filaments with the yz plane are calculated. Finally, the signals created by the individual filaments are summed. The resulting signals caused by such a streamer for the four different k values are presented in Fig. 11. To determine the scale length we again use the peak values (Fig. 12). We have to correct the calculated signals with $N^{1/2}$ as estimated before (Fig. 9). When we carry out this correction, the calculated scale length agrees with the input value of the computer simulation, and only the absolute values of the signals are spread relative to the estimated signals (Fig.

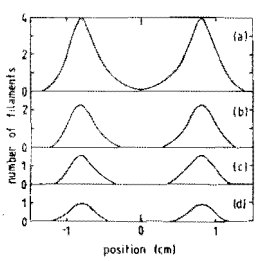

FIG. 9. The number of filaments seen simultaneously by the scattering diagnostic as a function of the position of the detection volume in the streamer (values of the wavenumber corresponding to Table II).

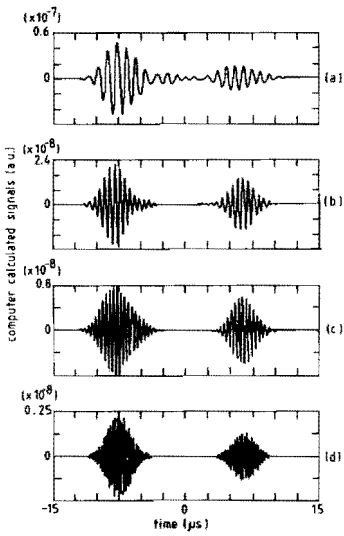

FIG. 11. The scattering signals caused by the streamer simulation (values of the wavenumber corresponding to Table II).

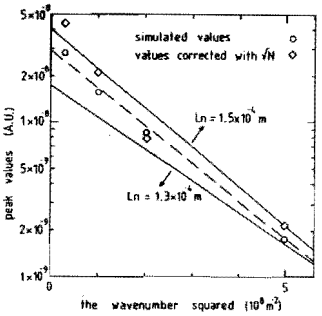

FIG. 12. The peak values of the simulated scattering signals.

12). This effect is caused by the inhomogeneous distribution of the filaments in the streamer. The calculated corrections to the real signals result in the dashed line in Fig. 7. We find

$$Lx = 1.3 \times 10^{-4} \text{ m}.$$

It is important to note that the estimate of the scale length does not depend on the total number of filaments in the streamer. The dependence on the spiraling angle is weak. For larger spiraling angles the correction remains nearly constant. For angles smaller than seven degrees the correction decreases.

By substituting the estimated scale length both for Lx and Lz in Eq. (8), we obtain a value of the electron density of about 5×10^{20} m^{-3}. This value is about a factor of 5 to 10 smaller than experimental and theoretical values in literature.[6,8] Possible explanations are the neglect of the inclination of the total streamer in the xy plane (this effect is seen in some runs) and an inaccurate calibration of the detector or other components of the experimental setup. Note that Lz is the scale length of a filament in the direction of the magnetic field. The filament may be somewhat larger in this direction. This leads to a smaller value for the electron density.

VI. CONCLUSIONS AND REMARKS

Here CO_2 laser scattering has been used to determine the scale length of the electron density fluctuations in an MHD generator. The measured value is

$$Lx = (1.3 \pm 0.2) \times 10^{-4} \text{ m}.$$

The result is only weakly dependent on the different assumptions made for the streamer model. Simultaneously a maximum value for the electron density of 5×10^{20} m^{-3} is found, which is a factor of 5 to 10 smaller than that found in other experiments. There are three effects causing an uncertainty in the determined electron density:

(1) the calculated electron density is strongly dependent on the assumed streamer features,

(2) a possible inclination of the total streamer in the xy plane,

(3) and finally the uncertainty about the calibration of the detector or other components in the experimental setup.

ACKNOWLEDGMENTS

We wish to thank Professor Dr. L. H. Th. Rietjens and the staff running the Shock Tube MHD Project of the Division of Direct Energy Conversion of the Eindhoven University of Technology (Department of Electrotechnical Engineering).

The work was supported by the Eindhoven University of Technology and by the Foundation for Fundamental Research on Matter ("Fundamental Onderzoek der Materie," abbreviated FOM).

[1]B. F. M. Pots, Ph.D. thesis, Eindhoven University of Technology, The Netherlands, 1979.
[2]B. F. M. Pots, J. J. H. Coumans, and D. C. Schram, Phys. Fluids **24**, 517 (1981).
[3]D. C. Schram, H. W. H. van Andel, G. Le Clair, and P. Brodeur, Plasma Phys. **25**, 1133 (1983).
[4]D. E. Evans, M. von Hellermann, and E. Holzhauer, Plasma Phys. **24**, 819 (1982).
[5]R. E. Slusher and C. M. Surko, Phys. Fluids **23**, 472 (1980).
[6]J. M. Wetzer, Ph.D. thesis, Eindhoven University of Technology, The Netherlands, 1984.
[7]E. Holzhauer and J. H. Massig, Plasma Phys. **20**, 867 (1978).
[8]H. J. Flinsenberg, Ph.D. thesis, Eindhoven University of Technology, The Netherlands, 1984.

6. THE PLASMA IN AN ARGON CASCADE ARC

6.1 Introduction

In cascade arcs stable plasmas can be generated under well defined conditions at preset values of current and pressure. These thermal plasmas are characterized by large densities, high degrees of ionization, and moderate temperatures. The electron and heavy particle temperatures range from less than 1 eV to several eV's at pressures between 1 and 1000 bar. Electric currents up to 500 A are involved.

Since the introduction by Maecker (MAE56) the cascade arc has been applied in a number of investigations of scientific interest. Different gases have been subject of research. Among them hydrogen, nitrogen, and the noble gases helium, neon, argon, and krypton received the most attention. The investigations concern the study of optical properties, radiation, and transport phenomena such as particle and energy transport. The research of all these plasma properties made the investigations of small deviations from local thermal equilibrium possible (KAF79,ROS81,NIC82,TIM85). Moreover at high pressures the non-ideal plasma behaviour has been studied (BAU76, TIM84).

Thermal plasmas are not only of scientific interest but are also applied in a large number of technological processes. These include e.g. plasma spraying, welding and cutting, high pressure light sources and high temperature chemistry. Other applications are high pressure circuit breakers and atomic emission spectroscopy with inductively coupled plasmas. The gases hydrogen and argon are most widely used. In these applications the knowledge of thermal plasmas acquired by means of cascade arcs can be used. Recently the supersonic expansion of a cascade arc has been used for plasma deposition (KRO85).

6.2 Cascade arc construction

The plasma is produced in a cascade arc as sketched in Fig. 6.1. The arc channel with a diameter of 5 mm is formed by the central bore of a series of copper plates. Each plate contains a channel system through which water flows to cool the region around the bore (ROS81). The plates are isolated from each other by means of silicon spacers.

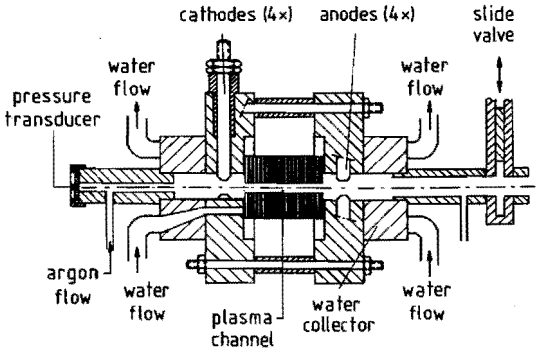

FIG. 6.1. Schematic drawing of the cascade arc.

The plate thickness is 1.6 mm, the interspacing between the plates is about 0.2 mm. The plates are pressed together by water collectors thus forming a channel with a length of 50 mm. These water collectors also contain the eight electrodes. Each electrode, consisting of a hollow copper shaft and a tungsten tip, is individually cooled. The arc current is provided by a current regulated DC power supply. A stabilizing resistor is placed in series with the arc. The part of the apparatus described so far has been used to investigate arcs without flow. In these experiments pressure pulses up to 10 bar and current pulses of 2 kA during 1 ms have been applied without causing technical problems (ROS81,TIM84).

The investigation of flowing thermal plasmas is the subject of this part of this work. To this end a flow controller has been installed at the cathode side. The mass flow through the arc can be regulated up to a value of about 1 g/s. A pressure transducer mounted at this side of the arc is used to measure the inlet pressure. At the outlet side (near the anodes) the plasma expands into a background of 1 bar. Here a slide valve has been installed. This valve is opened just before the flow through the arc is started and is closed as soon as possible after the flow is stopped. In this way the surrounding air is prevented to enter the plasma channel.

6.3 Non-equilibrium in an atmospheric argon plasma

The cascade arc has been used previously to investigate the deviations from equilibrium in atmospheric argon plasmas without flow

(ROS81,TIM84). The plasma parameters are determined under the assumption of PLTE by means of different spectroscopic techniques. Because of the small deviations from LTE present in thermal plasmas it is necessary to achieve a high accuracy. The measured PLTE and the calculated LTE relation between the electron density and the electron temperature are drawn in Fig. 6.2 for an argon plasma with a pressure of one bar (TIM84). The values for the different electron temperatures are achieved by varying the current through the arc and by measuring at different radial positions. The temperatures of neutrals and ions are only slightly lower than the temperature of the electrons.

The deviation from equilibrium can be expressed by the overpopulation of the ground level (δb_1). The overpopulations of other neutral levels are much smaller than δb_1 according to the results of a three level collisional radiative model (see Subsec. 2.3.2). The experimentally determined values of δb_1 (δb_1^{exp}) corresponding to the measurements plotted in Fig. 6.2 are given in Fig. 6.3. The solid curve in this figure denotes the theoretical values δb_1^{mod} which follow from the three level model described in Chapter 2. The main causes for the overpopulation of the ground level are diffusion at the lower temperatures and radiative recombination at the higher temperatures.

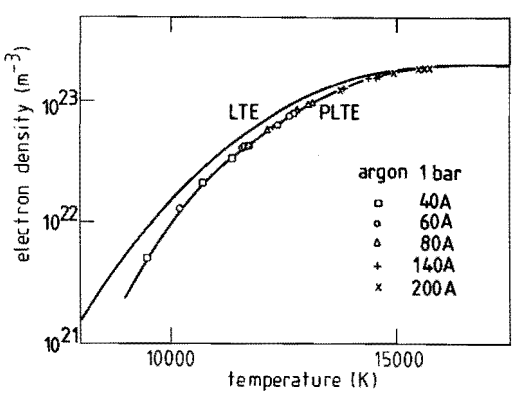

FIG. 6.2. The electron density as a function of the electron temperature in an argon plasma at 1 bar. The curve denoted by PLTE represents experimentally determined values of T_e and n_e under the assumption of PLTE. The curve denoted by LTE results from LTE calculations of the plasma composition.

From Figs. 6.2 and 6.3 it follows that at a constant pressure the plasma approaches the LTE composition more and more for higher values of the electron temperature and the electron density. The electron density is the most important parameter in this respect as can be concluded from measurements at different pressures. While the arc current is kept constant, the temperature decreases and the electron density increases when the pressure is raised. The higher electron density causes the overpopulation of the ground level to decrease. For an arc with an electric current of 60 A the overpopulation goes from 0.6 to 0.2 when the pressure is raised from 1 to 2 bar (values at the axis of the arc).

6.4 Present work

The behaviour of an argon plasma flowing through a cascade arc is the main subject of this part of this work. Theoretical and experimental results are given in the Chapters 7 and 8 respectively.

A simplified theoretical description is given in Chapter 7. The different balances for neutrals, ions, and electrons are combined to the mass, the momentum, and the energy balances for the total plasma. These balances include friction and ohmic heating. The resulting set

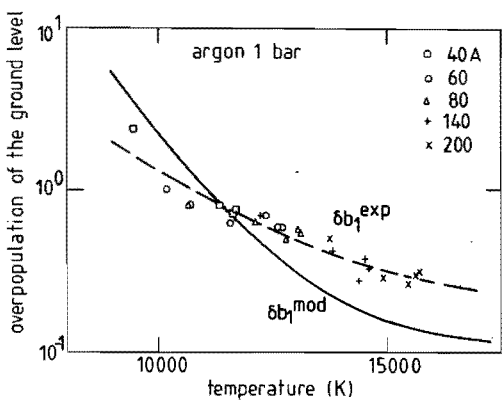

FIG. 6.3. The temperature dependence of the overpopulation of the ground state. The experimental values δb_1^{exp} correspond with the values plotted in Fig. 6.2. The curve with δb_1^{mod} represent values calculated with a three level model.

of differential equations resembles the gasdynamical formulation of the conservation of mass, momentum, and energy for an ideal gas. The thermodynamic properties of a plasma, which are quite different from those of an ideal gas, will be discussed. The equilibrium values of the thermodynamic properties will be used. The set of differential equations is solved numerically with experimentally determined values for the boundary conditions.

Experimental results for a cascade arc with a constant electric current of 60 A will be given in Chapter 8. Because of the axial gradients which are present in an arc with flow no "end-on" spectroscopic measurements can be used like in the experiments described in the previous subsection. The most important diagnostic is the measurement of the cascade plate voltages. The flow speed of the plasma and the plasma temperature can be determined from this as a function of the axial position in the arc. Furthermore the mass flow through the arc and the pressure at the cathode side of the arc are measured.

During the experiments the cascade arc has proven to be a reliable source of atmospheric flowing plasma. Theoretical and experimental results will be compared. Though the model calculations do not take the non-equilibrium into account, theoretical and experimental results agree reasonably well.

7. THEORETICAL DESCRIPTION OF A CASCADE ARC WITH FLOW

7.1 Introduction

In this chapter a theoretical model for a cascade arc with flow will be presented. Former investigations (ROS81,TIM84,TIM85) on an atmospheric argon plasma without flow showed this plasma to be close to local thermal equilibrium (LTE). The employment of a plasma flow will lower the temperature because cold argon gas enters the plasma channel. Therefore the deviation from equilibrium will be larger in a cascade arc with flow than in an arc without flow. Nevertheless the assumption that the plasma is in LTE will be used throughout. Consequently the model given here has to be considered as a first attempt to describe the plasma flow.

In this chapter the balance equations are worked out in a thermodynamic way. The thermodynamic properties occurring in the balance equations are discussed for a plasma which is in equilibrium. A comparison with the corresponding properties for an ideal gas is made. The differences between the thermodynamic properties of a plasma and those of an ideal gas are mainly determined by the degree of ionization. For a plasma which is not in equilibrium, the degree of ionization is lower than for a plasma which is in equilibrium. So the values of the thermodynamic properties of a non-equilibrium plasma will deviate somewhat from those of an equilibrium plasma in the direction of those of an ideal gas.

The thermodynamic properties calculated for a plasma in equilibrium are used in the formulation of a one-dimensional model. The boundary conditions needed to solve the resulting system of differential equations are derived from experimental data. Therefore in this chapter only the way in which these boundary conditions are obtained is described. Numerical results will be given in the next chapter together with the experimental results.

7.2 Balance equations

The equations we will use to describe a flowing plasma are the mass balance, the momentum balance, and the energy balance. These balances are given in Sec. 2.1. In this section the balances for the

various species are combined to obtain the mass balance, the momentum balance, and the energy balance for the total plasma. Furthermore one needs the equation of state.

Equation (2.1) gives the continuity equation for species α. Multiplying this equation with the mass m_α of a particle of species α and summing over all species gives

$$\frac{\partial}{\partial t}\left[\sum_\alpha (m_\alpha n_\alpha)\right] + \nabla\cdot\left[\sum_\alpha (m_\alpha n_\alpha \mathbf{w}_\alpha)\right] = \sum_\alpha \left[m_\alpha \left[\frac{\partial n_\alpha}{\partial t}\right]_{CR}\right] \tag{7.1}$$

The first term in Eq. (7.1) is the time derivative of the mass density ρ defined by

$$\rho = \sum_\alpha (m_\alpha n_\alpha) \tag{7.2}$$

The second term can be rewritten by assuming a one-dimensional flow in the x direction and by the definition of the mean one-dimensional flow speed:

$$u = \frac{1}{\rho}\sum_\alpha \left[n_\alpha m_\alpha (\mathbf{w}_\alpha)_x\right] \tag{7.3}$$

The collisional term at the right-hand side of Eq. (7.1) is zero because of the conservation of mass during a collision. All this leads to the one-dimensional mass balance for the total plasma:

$$\frac{\partial \rho}{\partial t} + \frac{\partial}{\partial x}(\rho u) = 0 \tag{7.4}$$

The momentum balance for particles of species α is given by Eq. (2.5). Summing over all species and using the above defined quantities leads to

$$\rho \frac{\partial u}{\partial t} + \rho u \frac{\partial u}{\partial x} + \frac{\partial p}{\partial x} + (\nabla\cdot\Pi)_x = \sum_\alpha M_\alpha \tag{7.5}$$

In Eq. (7.5), p denotes the total pressure (the sum of the partial pressures of all species according to Dalton's law). The contribution of the electrical field to the total momentum balance is zero because of quasi-neutrality. The influence of the magnetic field on the pressure by means of Lorentz forces is negligible (VAL84). $\sum_\alpha M_\alpha$ is zero in the plasma because of the conservation of momentum during a collision. The total momentum of the particles of a certain species may change as a result of collisions but the sum of the total momentum of the particles of all species does not change. In our one-dimensional model for the plasma flow all quantities are used averaged over the cross

section of the flow channel. The viscosity term, $(\nabla \cdot \Pi)_x$, leads to friction with the wall and is represented by a friction term. So the momentum balance becomes

$$\rho \frac{\partial u}{\partial t} + \rho u \frac{\partial u}{\partial x} + \frac{\partial p}{\partial x} = - \tfrac{1}{2} \rho u^2 \frac{f}{D} \tag{7.6}$$

The friction factor f represents the friction with the wall and D is the diameter of the flow channel. This formulation of the friction term is commonly used in gas dynamics (BOBSO) though the friction factor is often defined as $f' = \frac{1}{4} f$ (OWC64). The value of the friction factor will be discussed later.

The energy balance for particles of species a is given by Eq. (2.6). Again this equation is summed over all species. The total energy of a unit mass, ϵ_t, is used in the resulting energy balance. In one dimension this leads to (OWC64)

$$\frac{\partial \epsilon_t}{\partial x} + u \frac{\partial \epsilon_t}{\partial x} + \frac{1}{\rho} \frac{\partial}{\partial x} (pu) = q \tag{7.7}$$

In the energy balance Eq. (7.7), the source term q represents the net power added to the plasma per unit mass, e.g. as a result of ohmic heating and energy losses by radiation. The total energy is the sum of the internal energy and the kinetic energy. The total energy per unit mass can be expressed by (OWC64)

$$\epsilon_t = \epsilon + \tfrac{1}{2} u^2 = h - \frac{p}{\rho} + \tfrac{1}{2} u^2 \tag{7.8}$$

Here h is the specific enthalpy (enthalpy of a unit mass). In this work the specific enthalpy h will be used as main thermodynamic property. It will be discussed in the next section. Combining Eqs. (7.7) and (7.8) leads to the formulation of the energy balance as used henceforth:

$$\frac{\partial h}{\partial t} + u \frac{\partial h}{\partial x} + u \frac{\partial u}{\partial t} + u^2 \frac{\partial u}{\partial x} - \frac{1}{\rho} \frac{\partial p}{\partial t} = q \tag{7.9}$$

The last equation needed is the equation of state. Summing the partial pressures of all species one obtains the pressure of the plasma (Dalton's law):

$$p = \sum_a n_a k T_a \tag{7.10}$$

Atmospheric argon plasmas up to temperatures of about 20,000 K consist

of electrons, singly ionized atoms and neutral particles. The temperatures of these particles are almost equal to each other. Therefore we will use

$$T = T_e = T_i = T_n \tag{7.11}$$

So the total pressure is given by

$$p = (n_e + n_i + n_n)kT \tag{7.12}$$

Using quasi-neutrality ($n_e \approx n_i$) and the definition of the degree of ionization $\alpha = n_i/(n_i + n_n)$ this leads to

$$p = \rho RT(1 + \alpha) \tag{7.13}$$

Here R is the specific gas constant for argon. Note that Eq. (7.13) with $\alpha = 0$ expresses the ideal gas law.

7.3 Thermodynamic properties

In the previous section the basic equations for the description of a flowing plasma have been derived. In this section the quantities α (degree of ionization) and h (specific enthalpy), which occur in these equations, are considered.

The assumptions made in the previous subsection were

a) quasi-neutrality;

b) applicability of Dalton's law;

c) the temperatures of all particles are equal;

d) the atoms in the plasma are singly ionized;

e) the plasma flow is considered one-dimensional and flowing through a duct with a constant cross section.

For the evaluation of α and h we need another important assumption, namely that the plasma is in equilibrium. Now we can determine the electron density, the degree of ionization, and the specific enthalpy. These values are given for pressures between 1 and 5 bar.

For the calculation of the electron density we need Eq. (7.12) (Dalton's law) and quasi-neutrality ($n_e = n_i$). Furthermore the difference between the degeneracy of the neutral ground level and the partition function of neutral argon is neglected ($n_n = n_i$). The Saha equation gives the relation (in equilibrium) between the electron density, the ion density, and the density of ground level neutrals:

$$\frac{n_e n_i}{n_1} = S_{1+} \tag{7.14}$$

Combining Eqs. (7.12) and (7.14) leads to

$$\frac{p}{kT} = \frac{n_e^2}{S_{1+}} + 2n_e \tag{7.15}$$

Solving this quadratic equation in the electron density gives

$$n_e = \frac{\frac{p}{kT}}{\sqrt{1 + p/(kTS_{1+})} + 1} \tag{7.16}$$

Equations (7.15) and (7.16) are similar to Eqs. (2.14) and (2.15) but here the pressure p is the independent parameter whereas in Eqs. (2.14) and (2.15) the total heavy particle density is the independent parameter. For high temperatures Eq. (7.16) yields $n_e = p/(2kT)$ whereas Eq. (2.15) yields $n_e = n_x$. The electron density according to Eq. (7.16) is plotted in Fig. 7.1 as a function of the temperature for some values of the pressure. For higher values of the pressure the electron density is also higher.

The degree of ionization can be obtained by using Eqs. (7.12) and (7.16) in the definition of α:

$$\alpha = \frac{1}{\sqrt{1 + p/(kTS_{1+})}} \tag{7.17}$$

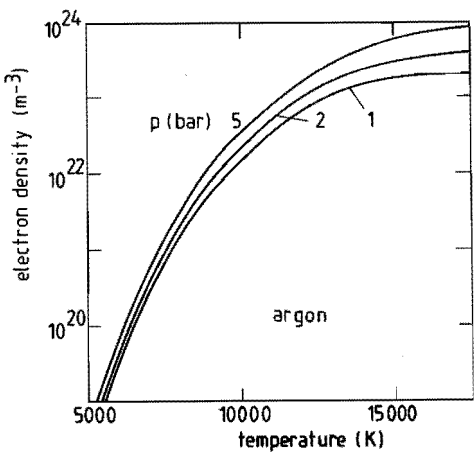

FIG. 7.1. The electron density, n_e, of an equilibrium argon plasma as a function of the temperature for some values of the pressure.

The degree of ionization, α, is lower for higher pressures. For high (electron) temperatures, α tends to 1. This can be seen in Fig. 7.2 where α is plotted as a function of the temperature for some values of the pressure. For temperatures smaller than 10,000 K, α is very small. This means that for these temperatures some expressions in which α occurs, e.g. Eq. (7.13), can be simplified. As will be shown later this is not always possible.

The specific enthalpy can be obtained by using the methods of statistical mechanics (HSU84):

$$h = \frac{1}{\rho}\left\{\frac{5}{2}kT(n_n + n_i + n_e) + kT^2\left[n_n\frac{\partial(\ln Z_n)}{\partial T} + n_i\frac{\partial(\ln Z_i)}{\partial T}\right] + n_i(E_{1+} - \Delta E)\right\} \tag{7.18}$$

Here Z_n and Z_i denote the partition functions of the neutrals and the ions respectively. So this equation includes the translational energy, the excitational energy, and the chemical energy (ionization). The excitational energy is negligible (OLS63). The remaining part of Eq. (7.18) can be simplified by using the expression for the degree of ionization, α, and $\theta = (E_{1+} - \Delta E)/k$. For argon $\theta \approx 1.82 \times 10^5$ K. This results in

$$h = \frac{5}{2}RT(1 + \alpha) + \alpha R\theta \tag{7.19}$$

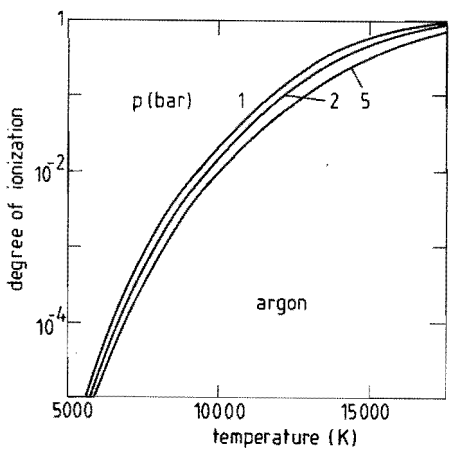

FIG. 7.2. The degree of ionization, α, of an equilibrium argon plasma as a function of the temperature for some values of the pressure.

The values of h according to Eq. (7.19) are plotted in Fig. 7.3 as a function of the temperature. For an ideal gas $h^o = (5/2)RT$ which is obtained from Eq. (7.19) with $\alpha = 0$ and given in Fig. 7.3 by a dotted line. For temperatures greater than about 8000 K the enthalpy of an argon plasma is greater than the ideal gas value. This is mainly due to the energy needed for ionization (note the large value of θ relative to $(5/2)T$). The contribution of the translational energy of the electrons and the ions to the enthalpy is small. At 10,000 K the degree of ionization α is a few per cent and the presence of electrons and ions is negligible in the equation of state given by Eq. (7.13). The energy needed to make these electrons and ions is however already about 20% of the enthalpy.

In the energy balance given by Eq. (7.9) only the derivatives of the specific enthalpy h to time and place do occur. Later on the balance equations will be written as a function of T, p, and u. Therefore the derivatives of h to T and p are needed. Differentiating the expression for h given by Eq. (7.19) to the temperature at a constant pressure gives

$$c_p = \left[\frac{\partial h}{\partial T}\right]_p = \frac{5}{2} R\left[(1 + \alpha) + \alpha_p T\right] + R\alpha_p\theta \qquad (7.20)$$

Here $\alpha_p = \left[\frac{\partial \alpha}{\partial T}\right]_p$ and can be rewritten by using Eqs. (7.17) and (2.9):

$$\alpha_p = \left[\frac{\partial \alpha}{\partial T}\right]_p = \frac{1}{T}\left[\frac{5}{2} + \frac{\theta}{T}\right] \frac{(1 - \alpha^2)\alpha}{2} \qquad (7.21)$$

The quantity α_p has a maximum for $\alpha \approx (1/3)\sqrt{3}$. This follows from

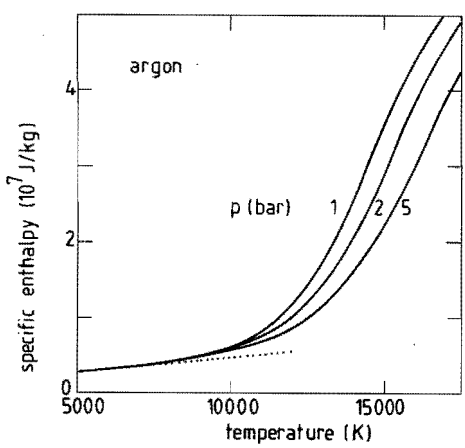

FIG. 7.3. The specific enthalpy, h, of an equilibrium argon plasma as a function of the temperature for some values of the pressure. The dotted line gives the values for an ideal monatomic gas ($h^o = (5/2)RT$).

differentiating the term $(1 - \alpha^2)\alpha$ in Eq. (7.21) to α because of the strong dependence of α on T. This maximum occurs for temperatures of about 15,000 K. The term $R\alpha_p\theta$ is the most important term in Eq. (7.20) for temperatures greater than 10,000 K and consequently c_p has also a maximum at 15,000 K. This can be seen in Fig. 7.4 where the specific heat at constant pressure, c_p, is plotted as a function of the temperature for some values of the pressure. For higher pressures the maximum occurs for higher temperatures because the ionization also becomes important for higher temperatures (see Fig. 7.2). The value of c_p for an ideal gas (c_p^o) is (5/2)R which is given by a dotted line in Fig. 7.4. This corresponds with Eq. (7.20) with $\alpha = 0$ and consequently $\alpha_p = 0$ according to Eq. (7.21). Again for temperatures greater than 8000 K deviations from the ideal gas value occur. At 10,000 K, $\alpha = 2\%$ but c_p is already 3 times the ideal gas value. So the electrons and the ions are negligible in the equation of state but are very important in the energy balance. Substitution of Eq. (7.21) into Eq. (7.20) gives

$$c_p = \frac{5}{2} R(1 + \alpha) + R\left[\frac{5}{2} + \frac{\theta}{T}\right]^2 \frac{(1 - \alpha^2)\alpha}{2} \qquad (7.22)$$

The specific heat c_p should decrease to the value $5R \approx 1.04 \times 10^3$ J/kg for α tending to 1. This situation is never reached because for temperatures above 17,500 K also double ionized argon becomes important. Consequently c_p goes up again (not shown in Fig. 7.4).

The dependence of the enthalpy on the pressure can be evaluated

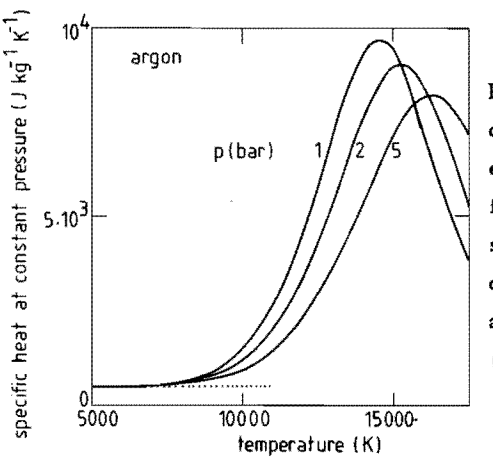

FIG. 7.4. The specific heat at constant pressure, c_p, of an equilibrium argon plasma as a function of the temperature for some values of the pressure. The dotted line gives the value for an ideal monatomic gas ($c_p^o = (5/2)R$).

in a similar way. Differentiating the expression for the specific enthalpy, h, given by Eq. (7.19) to the pressure at a constant temperature gives

$$c_T = \left[\frac{\partial h}{\partial p}\right]_T = \frac{5}{2} RT\alpha_T + R\theta\alpha_T \tag{7.23}$$

Here $\alpha_T = \left[\frac{\partial \alpha}{\partial p}\right]_T$ and can be rewritten by using Eq. (7.17):

$$\alpha_T = \left[\frac{\partial \alpha}{\partial T}\right]_p = -\frac{1}{p}\frac{\alpha(1-\alpha^2)}{2} \tag{7.24}$$

Note that α_T is negative ($0 < \alpha < 1$) and consequently c_T is also negative. Comparison of Eqs. (7.21) and (7.24) gives

$$\alpha_p T = -\left[\frac{5}{2} + \frac{\theta}{T}\right]\alpha_T p \tag{7.25}$$

So α_T and c_T have minima at about the same temperatures at which α_p and c_p have maxima. Because θ/T is large in the temperature range considered here, $\alpha_p T \gg |\alpha_T p|$ and consequently also $c_p T \gg |c_T p|$ as can be deduced from Eqs. (7.20) and (7.23). For low temperatures both α_T and c_T are equal to zero. In Fig. 7.5 the differential enthalpy at constant temperature, c_T, is plotted as a function of the temperature for some values of the pressure. The dependence on the pressure can be made clear by substituting Eq. (7.24) into Eq. (7.23):

$$c_T = -\frac{RT}{p}\left[\frac{5}{2} + \frac{\theta}{T}\right]\frac{\alpha(1-\alpha^2)}{2} \tag{7.26}$$

This dependence is caused by the factor T/p in Eq. (7.26). Moreover Eq. (7.26) shows that c_T should go to zero for α tending to 1. Like for c_p this situation is never reached because for temperatures above

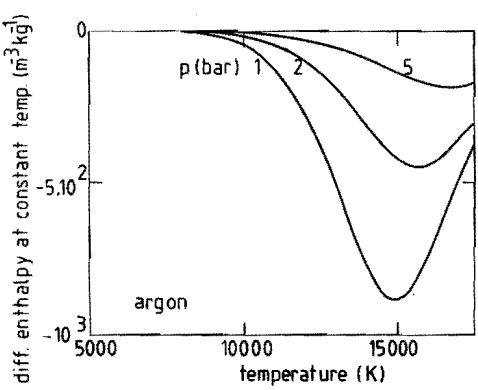

FIG. 7.5. The differential enthalpy at constant temperature, c_T, of an equilibrium argon plasma as a function of the temperature for some values of the pressure. The value for an ideal gas is zero because the enthalpy of an ideal gas is independent of the pressure.

17,500 K also double ionized argon becomes important (not shown in Fig. 7.5).

The specific enthalpy h as occuring in Eq. (7.9) can be written as a function of T and p by means of the quantities c_p and c_T:

$$dh = c_p dT + c_T dp \tag{7.27}$$

Remind c_p and c_T are also functions of α which is given as a function of T and p by Eq. (7.17).

In the previous section the mass, momentum, and energy balances are given as differential equations in ρ, u, p, and T. The explicit dependence of h as a function of p and T has been worked out above. The mass density ρ can be removed from the differential equations describing the plasma flow by using the equation of state. The last variable which has to be considered is the flow speed u. Like in all gas dynamic problems its value in relation to the speed of sound is important. Therefore the speed of sound will be considered here before the differential equations are rewritten into the form used to solve them numerically (next section).

The speed of sound, a, is both for an ideal gas and for an nonideal gas in equilibrium defined by (OWC64)

$$a^2 = \left[\frac{\partial p}{\partial \rho}\right]_{s,c} \tag{7.28}$$

Here the subscripts s and c denote that the entropy and the composition of the plasma (degree of ionization) are held constant during the differentiation. Because the composition is considered to be constant during the differentiation, the speed of sound given by Eq. (7.28) is often called the frozen speed of sound. Sound waves are (small) disturbances propagating in a reversible adiabatic (isentropic) manner. The frozen speed of sound can be evaluated using the ratio of the specific heats c_p and c_V in which $c_V = (\partial \epsilon / \partial T)_V$ is the specific heat at constant volume. Keeping the volume constant during the differentiation is the same as keeping the mass density constant during the differentiation. So c_V can be rewritten according to

$$c_V = \left[\frac{\partial \epsilon}{\partial T}\right]_V = \left[\frac{\partial h}{\partial T}\right]_\rho - \frac{1}{\rho}\left[\frac{\partial p}{\partial T}\right]_\rho = c_p + \left[c_T - \frac{1}{\rho}\right]\left[\frac{\partial p}{\partial T}\right]_\rho \tag{7.29}$$

The derivative $(\partial p/\partial T)_\rho$ can be analysed by using the equation of state given by Eq. (7.13). Using Eqs. (7.22) and (7.26) for c_p and c_T leads

to c_V as a function of α and T:

$$c_V = \frac{3}{2} R(1 + \alpha) + R\left[\frac{3}{2} + \frac{\theta}{T}\right]^2 \frac{\alpha(1-\alpha)}{2-\alpha} \tag{7.30}$$

The specific heat at constant volume, c_V, is given in Fig. 7.6 as a function of the temperature for some values of the pressure. The value of c_V for a monatomic ideal gas is (3/2)R which is given by a dotted line in Fig. 7.6. According to fundamental thermodynamic laws the ratio c_p/c_V can be written as (OWC64)

$$\frac{c_p}{c_V} = \frac{(\partial p/\partial \rho)_{s,c}}{(\partial p/\partial \rho)_T} = \frac{a^2}{(\partial p/\partial \rho)_T} \tag{7.31}$$

This leads to

$$a^2 = \frac{c_p}{c_V}\left[\frac{\partial p}{\partial \rho}\right]_T = \frac{c_p}{c_V}\left[\left[\frac{\partial \rho}{\partial p}\right]_T\right]^{-1}$$

The derivative in the right-hand side of this equation can be analysed by using the equation of state given by Eq. (7.13):

$$\left[\frac{\partial p}{\partial \rho}\right]_T = \left[\frac{\partial}{\partial \rho}\left[\frac{p}{RT(1+\alpha)}\right]\right]_T = \frac{1}{RT(1+\alpha)} - \frac{\alpha_T p}{RT(1+\alpha)^2}$$

$$= \frac{1 - \frac{1}{2}\alpha}{RT} \tag{7.32}$$

Here Eq. (7.24) has been used for $\alpha_T p$. All this leads to the following equation for the frozen speed of sound:

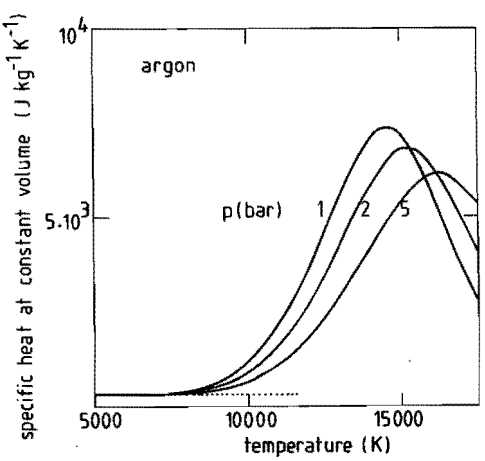

FIG. 7.6. The specific enthalpy at constant volume, c_V, of an equilibrium argon plasma as a function of the temperature for some values of the pressure. The dotted line gives the value for an ideal monatomic gas ($c_V^0 = (3/2)R$).

$$a = \left[\frac{c_p}{c_V}\,\frac{RT}{1 - \tfrac{1}{2}\alpha}\right]^{\tfrac{1}{2}} \tag{7.33}$$

The ratio c_p/c_V is given in Fig. 7.7 as a function of the temperature for some values of the pressure. The value of c_p/c_V for a monatomic ideal gas ($c_p^o/c_V^o = 5/3$) is given by a dotted line. The ratio c_p/c_V shows a deviation from the ideal gas value for temperatures greater than 6000 K. The behaviour of c_p/c_V for higher temperatures is caused by the maxima in c_p and c_V occuring for different temperatures. The factor $1 - \tfrac{1}{2}\alpha$ is important for the frozen speed of sound according to Eq. (7.33) at temperatures greater than 13,000 K. The resulting values for the frozen speed of sound are given in Fig. 7.8 as a function of

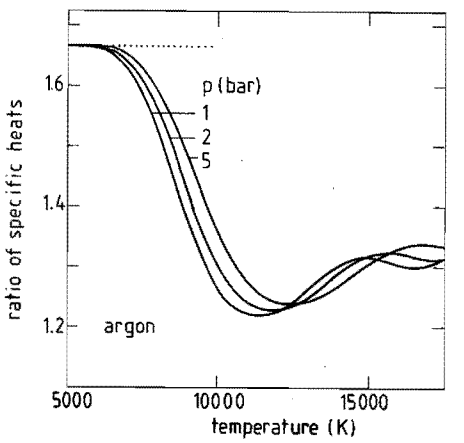

FIG. 7.7. The ratio of specific heats, c_p/c_V, of an equilibrium argon plasma as a function of the temperature for some values of the pressure. The dotted line gives the value for an ideal monatomic gas ($c_p^o/c_V^o = 5/3$).

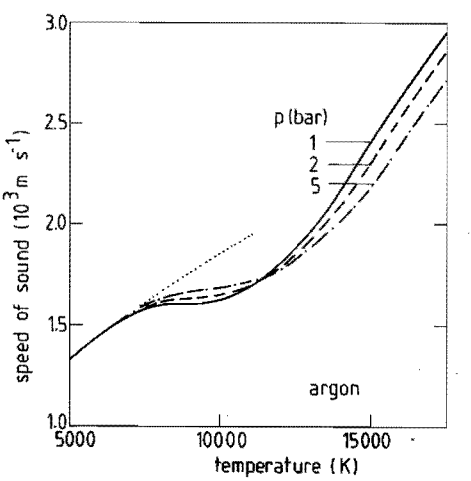

FIG. 7.8. The speed of sound, a, of an equilibrium argon plasma as a function of the temperature for some values of the pressure. The dotted curve gives the values for an ideal monatomic gas ($a^o = \sqrt{(5/3)RT}$).

the temperature for different values of the pressure. The value for a monatomic ideal gas $a^o = \sqrt{(5/3)RT}$ is given by a dotted curve. The strong decrease of c_p/c_V causes the frozen speed of sound, a, to be nearly constant between 8000 and 10,000 K. For temperatures greater than 11,500 K the frozen speed of sound also increases because of the higher degree of ionization.

7.4 One-dimensional model

7.4.1 *Basic formulation*

In this section the balance equations and the equation of state derived in Sec. 7.2 will be used. The thermodynamic properties described in Sec. 7.3 are substituted in these equations. The resulting equations are three first order differential equations in the variables p, u, and T.

From the equation of state given by Eq. (7.13) one can derive

$$d\rho = d\left[\frac{p}{RT(1+\alpha)}\right] = \frac{\rho}{p}\left[1 - \frac{\alpha_T p}{1+\alpha}\right]dp - \frac{\rho}{T}\left[1 + \frac{\alpha_p T}{1+\alpha}\right]dT \qquad (7.34)$$

Equation (7.34) and the definitions of α_p and α_T are used in the mass balance Eq. (7.4). Dividing by the mass density ρ leads to the mass balance expressed in p, u, and T:

$$\frac{1}{p}\left[1 - \frac{\alpha_T p}{1+\alpha}\right]\frac{\partial p}{\partial t} - \frac{1}{T}\left[1 + \frac{\alpha_p T}{1+\alpha}\right]\frac{\partial T}{\partial t}$$

$$+ \frac{u}{p}\left[1 - \frac{\alpha_T p}{1+\alpha}\right]\frac{\partial p}{\partial x} + \frac{\partial u}{\partial x} - \frac{u}{T}\left[1 + \frac{\alpha_p T}{1+\alpha}\right]\frac{\partial T}{\partial x} = 0 \qquad (7.35)$$

The momentum balance expressed in p, u, and T can be obtained by substituting the mass density ρ in Eq. (7.6):

$$\frac{\partial u}{\partial t} + u\frac{\partial u}{\partial x} + \frac{RT(1+\alpha)}{p}\frac{\partial p}{\partial x} = -\tfrac{1}{2}u^2\frac{f}{D} \qquad (7.36)$$

The energy balance as given by Eq. (7.9) is rewrittten by using Eqs. (7.13) and (7.27) to eliminate the mass density and the specific enthalpy respectively:

$$\left[c_T - \frac{RT(1+\alpha)}{p}\right]\frac{\partial p}{\partial t} + u\frac{\partial u}{\partial t} + c_p\frac{\partial T}{\partial t}$$

$$+ uc_T\frac{\partial p}{\partial x} + u^2\frac{\partial u}{\partial x} + uc_p\frac{\partial T}{\partial x} = q \qquad (7.37)$$

Equations (7.35) to (7.37) constitute a system of three quasi-linear partial differential equations in the dependent variables p, u, and T. This means that this system is linear in the derivatives of the dependent variables but not in these variables themselves. The method of characteristics (OWC64) leads to three real solutions for the gradient $\frac{dx}{dt}$ of the characteristic curves:

$$\frac{dx}{dt} = u + a \qquad (7.38a)$$

$$\frac{dx}{dt} = u - a \qquad (7.38b)$$

$$\frac{dx}{dt} = u \qquad (7.38c)$$

This means that waves can propagate with $u + a$, $u - a$, and u. The speed a is the speed of sound as derived in the previous section.

The waves propagating with $u + a$ and $u - a$ are ordinary sound waves with amplitudes $\hat{p}$, $\hat{u}$, and $\hat{T}$ (and consequently $\hat{\rho}$). The relation between the amplitudes $\hat{p}$ and $\hat{\rho}$ is given by the isentropic exponent γ which follows from the compatibility relations corresponding to the characteristic curves (OWC64):

$$\frac{\hat{p}}{p} = \gamma\frac{\hat{\rho}}{\rho} = \frac{c_p}{c_V}\frac{1}{(1+\alpha)(1-\frac{1}{2}\alpha)}\frac{\hat{\rho}}{\rho} \qquad (7.39)$$

This expression for γ corresponds with the expression derived by Matsuzaki using thermodynamic methods (MAT82). The isentropic exponent, γ, is drawn in Fig. 7.9 as a function of the temperature for different values of the pressure. For α tending to zero one obtains the isentropic exponent for an ideal monatomic gas: $\gamma^o = c_p^o/c_V^o = 5/3$ (dotted line in Fig. 7.9). In the same way the isentropic exponent ζ relating the amplitudes p and T can be obtained:

$$\frac{\hat{p}}{p} = \zeta\frac{\hat{T}}{T} = \frac{\gamma[1 + \alpha_p T/(1+\alpha)]}{\gamma[1 + \alpha_T p/(1+\alpha)] - 1}\frac{\hat{T}}{T} \qquad (7.40)$$

The isentropic exponent ζ is given in Fig. 7.10 as a function of the temperature for different values of the pressure. For α tending to

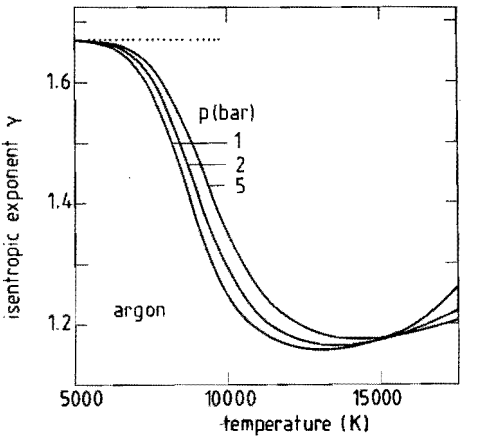

FIG. 7.9. The isentropic exponent γ of an equilibrium argon plasma as a function of the temperature for some values of the pressure. The dotted line gives the value for an ideal monatomic gas ($\gamma^o = 5/3$).

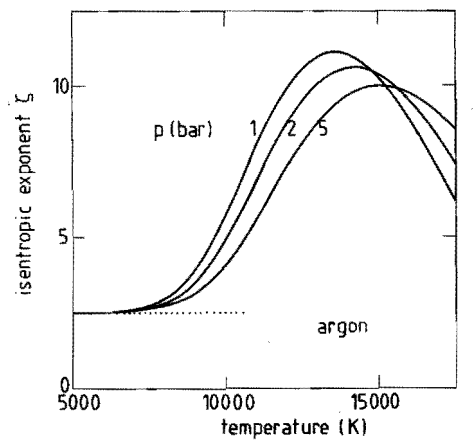

FIG. 7.10. The isentropic exponent ζ of an equilibrium argon plasma as a function of the temperature for some values of the pressure. The dotted line gives the value for an ideal monatomic gas ($\zeta^o = 5/2$).

zero the ideal gas value $\zeta^o = \gamma^o/(\gamma^o - 1) = 5/2$ is obtained (dotted line in Fig. 7.10). To shorten the notation given above we will use

$$A_p = 1 + \alpha_p T/(1 + \alpha) \tag{7.41}$$

and

$$A_T = 1 - \alpha_T p/(1 + \alpha) \tag{7.42}$$

Both A_p and A_T are one for an ideal gas. The term A_p is given in Fig. 7.11 as a function of the temperature for different values of the pressure. It reaches a maximum of about 2.8 for a temperature of about 15,000 K. The curves for A_T are similar to those for A_p. The deviation from the ideal gas value ($A_T^o = 1$) is however small: the maximum is

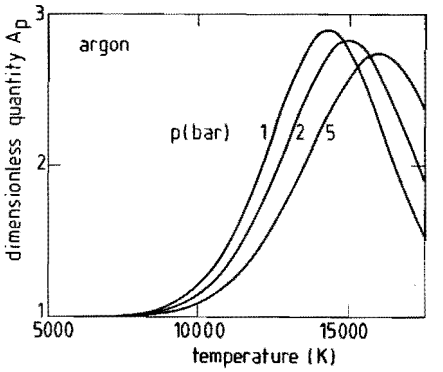

FIG. 7.11. The dimensionless quantity A_p for an equilibrium argon plasma as a function of the temperature for some values of the pressure. $A_p^o = 1$ for an ideal monatomic gas.

about 1.1. The relation between ζ and γ using A_p and A_T is represented by

$$\zeta = \frac{\gamma A_p}{\gamma A_T - 1} \tag{7.43}$$

A wave propagating with $(dx/dt) = u$ is a disturbance moving with the same speed as the plasma. The amplitudes $\hat{p}$ and $\hat{u}$ are zero along the characteristic curve $(dx/dt) = u$. The temperature is locally higher or lower ($\hat{T} \neq 0$). According to the theory presented here such a temperature deviation can exist permanently because the heat conductivity is not taken into account. We will need the description of the waves propagating along the characteristic curves given by Eq. (7.38) for the explanation of experimental observations (Chapter 8).

For a description of a stationary flow the derivatives to the time in the mass, momentum, and energy balances given by Eqs. (7.35) to (7.37) are set equal to zero. Furthermore the definition of A_p and A_T as given by Eq. (7.41) and (7.42) will be used for simplicity. This leads to the following formulation of the balances:

$$\frac{uA_T}{p}\frac{\partial p}{\partial x} + \frac{\partial u}{\partial x} - \frac{uA_p}{T}\frac{\partial T}{\partial x} = 0 \tag{7.44}$$

$$\frac{RT(1+\alpha)}{p}\frac{\partial p}{\partial x} + u\frac{\partial u}{\partial x} = -\tfrac{1}{2}u^2\frac{f}{D} \tag{7.45}$$

$$uc_T\frac{\partial p}{\partial x} + u^2\frac{\partial u}{\partial x} + uc_p\frac{\partial T}{\partial x} = q \tag{7.46}$$

The system given by Eqs. (7.44) to (7.46) represents the mass, momentum, and energy balances respectively. This system is quasi-linear in the terms $\frac{1}{p}\frac{\partial p}{\partial x}$, $\frac{1}{u}\frac{\partial u}{\partial x}$, and $\frac{1}{T}\frac{\partial T}{\partial x}$ and can be written in vector notation:

$$\begin{bmatrix} uA_T & u & -uA_p \\ RT(1+\alpha) & u^2 & 0 \\ uc_T p & u^3 & uc_p T \end{bmatrix} \begin{bmatrix} \frac{1}{p}\frac{\partial p}{\partial x} \\ \frac{1}{u}\frac{\partial u}{\partial x} \\ \frac{1}{T}\frac{\partial T}{\partial x} \end{bmatrix} = \begin{bmatrix} 0 \\ -\tfrac{1}{2}u^2\frac{f}{D} \\ q \end{bmatrix} \tag{7.47}$$

The determinant, *Det*, of the matrix in Eq. (7.47) is given by:

$$Det = u^2\left\{\left[A_T c_p T + A_p c_T p - A_p RT(1+\alpha)\right]u^2 - c_p RT^2(1+\alpha)\right\} \tag{7.48}$$

The determinant is zero for

$$u = u' := \left[\frac{c_p RT^2(1+\alpha)}{A_T c_p T + A_p c_T p - A_p RT(1+\alpha)}\right]^{1/2} \tag{7.49}$$

With the expressions for c_p, c_V, and c_T it can be proven that the speed u' occurring in Eq. (7.49) is equal to the frozen speed of sound, a, as given by Eq. (7.33). Instead of the ratio of specific heats one can also use the isentropic exponent γ given by Eq. (7.39). This leads to

$$a = \sqrt{\gamma RT(1+\alpha)} \tag{7.50}$$

The determinant can be simplified by introducing the Mach number:

$$M = \frac{u}{a} \tag{7.51}$$

Using the isentropic exponent, γ, and the Mach number, M, leads to

$$Det = -\frac{u^2 a^2}{\gamma} c_p T(1 - M^2) \tag{7.52}$$

So for $M = 1$ and only for $M = 1$ the determinant is zero and the system of equations (7.47) has no solution. For $M^2 \neq 1$ the system (7.47) can be rewritten to

$$\frac{1}{p}\frac{\partial p}{\partial x} = \frac{-\gamma M^2}{1 - M^2}\left[\left(1 + \frac{\gamma}{\zeta} M^2\right) \times \tfrac{1}{2}\frac{f}{D} + \frac{\gamma}{\zeta a^2} \times \left[\frac{q}{u}\right]\right] \qquad (7.53a)$$

$$\frac{1}{u}\frac{\partial u}{\partial x} = \frac{-\gamma M^2}{1 - M^2}\left[\left[\frac{1}{\gamma} + \frac{1}{\zeta}\right] \times \tfrac{1}{2}\frac{f}{D} + \frac{1}{\zeta u^2} \times \left[\frac{q}{u}\right]\right] \qquad (7.53b)$$

$$\frac{1}{T}\frac{\partial T}{\partial x} = \frac{-\gamma M^2}{1 - M^2}\left[\frac{\gamma A_T M^2 + A_p - 1}{\zeta A_p} \tfrac{1}{2}\frac{f}{D} - \frac{1}{\zeta A_p}\left[\frac{1}{u^2} - \frac{\gamma A_T}{a^2}\right]\left[\frac{q}{u}\right]\right] \qquad (7.53c)$$

The first part of the term between the brackets gives the influence of the friction, the second part gives the influence of the net power added to the plasma. The factor

$$\left[\frac{1}{u^2} - \frac{\gamma A_T}{a^2}\right]$$

in the power term in Eq. (7.53c) is positive for

$$u^2 < \frac{a^2}{\gamma A_T} = \frac{RT}{1 - \frac{1}{2}\alpha} \qquad (7.54a)$$

or equivalently

$$M^2 < \frac{c_V}{c_p} \qquad (7.54b)$$

For larger values of u^2 or M^2 this factor is negative. All the other factors preceding the terms $\frac{1}{2}f/D$ and q/u are positive for all values of the pressure, the temperature, and the flow speed. The Mach number is in the cascade arc always smaller than 1 (see the next subsection). Therefore the factor $\gamma M^2/(1 - M^2)$, which occurs in Eqs. (7.53a) to (7.53c), is positive. This leads to the following conclusions for a stationary flow:

a) both for high values of the friction and for high values of the net power input, the pressure difference over the arc is relatively large while the pressure at the entrance is greater than the pressure at the exit,

b) both for high values of the friction and for high values of the net power input, the difference between the flow speed at the entrance and at the exit is relatively large (the flow speed at the entrance is smaller than the flow speed at the exit),

c) the temperature difference over the arc is relatively small:

the friction part of Eq. (7.53c) is negative while the power part of Eq. (7.53c) is positive (the latter not for $M^2 > c_v/c_p$).
So numerical solutions of the model will show rather large pressure and flow speed gradients and relatively small temperature gradients.

7.4.2 *Boundary conditions*

In the previous subsection a description of the plasma flow is given by means of a system of three first order differential equations in the variables p, u, and T. For a numerical evaluation one needs three boundary conditions. These will be derived from the experiments. Furthermore we will need the friction factor, f, and the source term in the energy balance, q.

The pressure at the entrance of the channel (cathode side) and the mass flow through the arc are measured directly (see Chapter 6). The temperature of the plasma in the channel can be determined from plate voltage measurements (see Chapter 8). For the model we only need the temperature at the entrance of the channel ($x = 0$). The flow speed at the entrance can be calculated from the pressure and the temperature at the entrance and the measured mass flow.

The source term in the energy balance is difficult to evaluate but its influence is estimated. The source term is at most equal to the ohmic dissipation which is derived from the measurement of the electrical field. The ohmic dissipation is however far too small to explain the pressure difference over the arc which is therefore determined by the friction. To know the pressure difference over the arc one has to consider the situation at the exit of the plasma channel. For a flow through a channel with a constant cross section there are two possibilities: either the Mach number is less than one and the pressure equals the pressure of the surrounding air (1 bar in our case), or the Mach number equals one and the pressure is greater than one bar (OWC64). The Mach number as a function of pressure, temperature, and mass flow ($\phi = \rho u A$) is given by

$$M = \left[\frac{RT(1 + \alpha)}{\gamma}\right]^{\frac{1}{2}} \times \frac{\phi}{pA} \qquad (7.55)$$

In Fig. 7.12 the Mach number at a pressure of one bar is plotted as a function of the temperature for different values of the mass flow. For

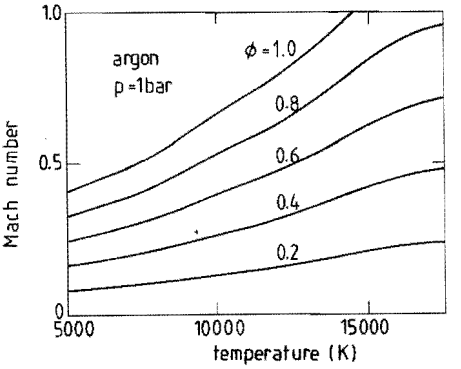

FIG. 7.12. The Mach number for an equilibrium argon plasma flowing through a channel with a diameter of 5 mm as a function of the temperature for different values of the mass flow. The pressure is taken equal to that of the surrounding air (1 bar).

A the cross section of the plasma channel, which has a diameter of 5 mm, has been used. In our experiments (Chapter 8) the maximum mass flow is about 1 g/s. From Fig. 7.12 it can be concluded that $M = 1$ corresponds with temperatures greater than 14,500 K and mass flows between 0.8 and 1 g/s. These high temperatures are not reached with the applied electrical currents (up to 80 A) and consequently the Mach number is less than one. So the pressure at the exit of the channel is one bar. We will use a value for the friction factor to get $p = 1$ bar at the end of the channel. This is done because no data are available in literature for this type of channel wall (BOL85). The wall of the plasma channel is determined by the cascade plates which are separated by silicon spacers. The distance between the silicon spacers and the plasma is about 13 mm, whereas the diameter of the channel is 5 mm.

8. EXPERIMENTS ON A CASCADE ARC WITH FLOW

8.1 Introduction

Measurements performed at a cascade arc with an imposed argon flow are described in this chapter. The measured quantities are the mass flow, the pressure at the entrance of the channel, and the plate voltages. From the measured plate voltages the temperature and the flow speed of the arc can be determined. Experimental and theoretical results are compared.

In Sec. 8.2 we describe the measuring procedure. For a description of the construction of the cascade arc, the reader is referred to Sec. 6.2. The experiments show that, starting from an arc without flow, a stationary situation is reached within one second. The differences between the stationary situations with and without flow are used to evaluate the plasma temperature. The measured plate voltages exhibit fluctuations during the plasma flow. The speed derived from these fluctuations is compared with the different speeds at which disturbances can propagate in a plasma (see Chapter 7) and turns out to be about equal to the flow speed. The procedures used to evaluate the temperature and the flow speed are given in Sec. 8.3.

In Sec. 8.4, experimental and theoretical results for an argon arc with an electric current of 60 A and a mass flow of 0.5 g/s are compared. Applying the boundary conditions in the model gives values for the friction factor which cannot be determined theoretically (see Chapter 7). The source term in the energy balance is difficult to evaluate but its influence is estimated. The conclusions are summarized in Sec. 8.5. The theoretical and the experimental results show some discrepancies implying that further investigations should be performed.

8.2 Measuring procedure

The measurements are controlled by a PDP 11/03 computer. This computer is connected to an interface system and controls the valves in the gas flow circuit and processes the data acquired from the experiments. Each measuring signal is registrated by an 8-bit analog-digital convertor (ADC) in combination with a transient recorder. The

sampling time of the ADC's can be set between 1 μs and 0.25 s. The transient recorders can store 1024 samples each. By using the appropriate sampling time, one can measure either fast fluctuations or slow changes during the establishment of the flow. After a measurement the signals are processed by the PDP 11/03 or by the central computer of the University (B7900).

The pressure at the cathode side is measured by means of a Kistler pressure transducer (model 601A). The sensitivity is 200 mV/bar and the output signal is directly coupled to the ADC. The plate voltages are measured in two different ways which are schematically shown in Fig. 8.1. The upper part of this figure represents the measurement of the DC voltage difference between two plates which are connected with an amplifier (Tektronix O-unit). The reduced difference between the voltages is led to an ADC. Dividing the voltage difference by the distance between the plates yields the electric field in the arc. The lower part of Fig. 8.1 represents the circuit used in the measurement of the AC part of a plate voltage. The DC part is stopped by means of a capacitor and the remaining signal is weakened by a frequency-compensated voltage reducer. Signals with frequencies between 1 and 400 kHz can be measured in this way. The voltage reducer is designed to avoid phase shifts for frequencies of about 10 kHz. Each of the plates of the arc can be used in both types of measurements.

The entrance pressure and the electric field during a measurement are given as a function of time in Fig. 8.2. The measurement starts with an arc without flow. The slide valve at the anode side is still

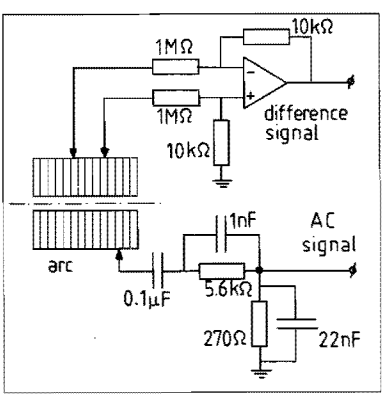

FIG. 8.1. Schematic drawing of the two different ways in which plate voltages are measured. The upper part of the figure shows the DC-voltage measurements; the lower part gives the circuit for the measurement of fluctuations between 1 and 400 kHz.

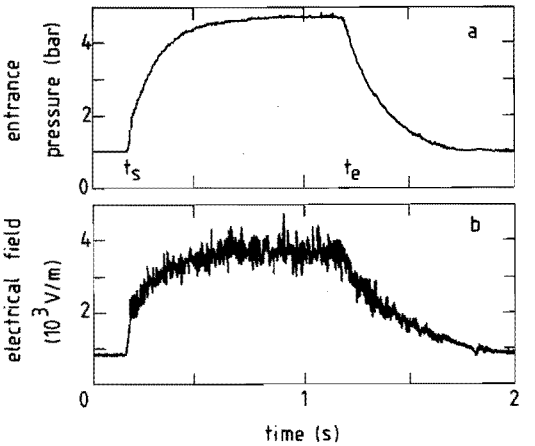

FIG. 8.2. The pressure at the cathode side (a) and the electric field in the arc (b) as a function of time during a measurement with a current I = 60 A. The valve to the high pressure reservoir is opened at time t_s and is closed at time t_e. The sampling time is 2 ms.

closed. This situation corresponds with that of previous investigations (ROS81,TIM84). Owing to these investigations, the properties of an argon cascade arc without flow are well known. This will be used in the elaboration of the plate voltage measurements. At a certain moment the slide valve is opened to provide free exit of the plasma from the anode into the surrounding air. At time t_s, the valve in the connection between the cathode side of the arc and a high pressure reservoir is opened. The pressure at the cathode side rises and the plasma starts to flow. The pressure reaches a stationary value within 0.7 s. The high pressure reservoir is shut off at time t_e (one second after t_s) and the flow stops. By closing the slide valve the initial situation is obtained again. During the entire procedure the electric current through the arc is kept constant. The electric field is given in the lower part of Fig. 8.2. The general tendency is the same as that of the pressure but the electric field shows large fluctuations. Measurements with a sampling time of 4 μs, instead of 2 ms as in Fig. 8.2, show that these fluctuations have a frequency of about 8 kHz.

In the measurements presented in Fig. 8.2, no flow controller was installed. The entrance pressure was adjusted by the reducing valve

which is mounted at the high pressure reservoir. A flow controller with a maximum mass flow of about 1 g/s has been installed in experiments performed later on. Consequently a known mass flow could be applied. In both experiments with and without flow controller, the pressure reaches a stationary value within 0.7 s and so the same measuring procedure has been applied in the two cases. The decrease of the pressure after time t_e in Fig. 8.2 is almost exponential. The mass flow can therefore be determined from the characteristic time involved in this decrease and the contents of the volume which is present at the cathode side. This yields a mass flow of about 2 g/s. For measurements with a lower entrance pressure, the values of the mass flow determined in this way correspond with the values set by the flow controller.

8.3 Temperature and flow speed determination

First we will consider the derivation of the plasma temperature from the measured voltage differences between the plates. An example of such a measurement is given in Fig. 8.3. Here the voltages of a number of plates with respect to the voltage of the plate at x = 15 mm are drawn. The entrance of the channel is at x = 0. The crosses denote voltages which are measured without flow through the arc. These measurements match a straight line rather well. This corresponds with an electric field which is independent of the axial position. The dots represent the mean voltages measured in a cascade arc with flow. The

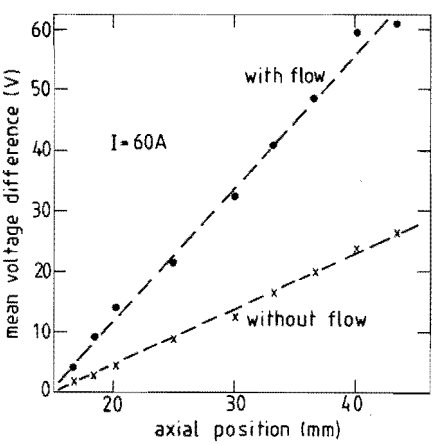

FIG. 8.3. The measured voltages of a number of plates with respect to the plate at x = 15 mm, for a cascade arc with and without flow (dots and crosses respectively). The voltage differences of the measurements with flow are averaged over the last 0.2 s before time t_e. The dashed curves are fitted to the measurements.

mean voltages are obtained by averaging the (fluctuating) voltages over the last 0.2 s before time t_e. The value of the electric field is with flow about two and a half times higher than without flow. To examine the dependence on the axial position, a curve of the second degree has been fitted to the measured plate voltages (dashed curve). This curve is differentiated with respect to the axial position to obtain the electric field. The distinction between the curve and a straight line is however small. Consequently the electric field is nearly independent of the axial position. At the left hand side of Fig. 8.3, the electric field is about 4% higher than at the right-hand side.

The differences between the electric fields measured with and without flow can be used to determine the plasma temperature. The current through the arc, I, is kept constant during the experiments. This means that also the mean current density, $\overline{J} = I/A$, is constant where A is the cross-section of the plasma channel. The mean current density is related to the electric field, E, by

$$\overline{J} = \overline{\sigma}E \tag{8.1}$$

$\overline{\sigma}$ is the electrical conductivity averaged over the cross-section. So an increase of the electric field, due to the application of the flow, corresponds with a decrease of the electrical conductivity. The electrical conductivity of an argon plasma in equilibrium is given in Fig. 8.4 as a function of the temperature for some values of the

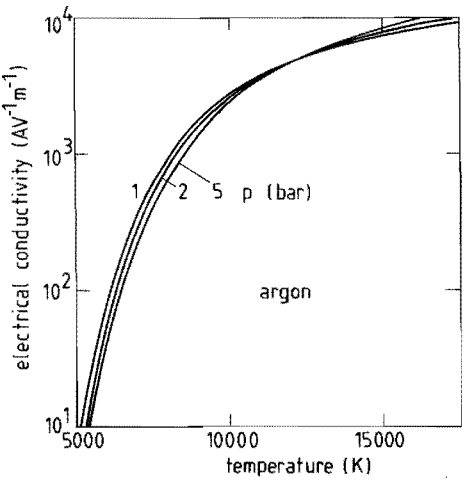

FIG. 8.4. The electrical conductivity of an argon plasma in equilibrium as a function of the temperature for some values of the pressure (AUB85).

pressure (AUB85). In an arc without flow the temperature is about 12,700 K for a current of 60 A and a pressure of one bar (TIM84). Note that for $T < 12{,}700$ K the electrical conductivity strongly depends on the temperature. In the pressure range given here ($1 \leq p \leq 5$ bar), the influence of the pressure is only small. Therefore one can deduce the temperature in the arc rather accurately from the electrical conductivity determined by using Eq. (8.1) and the measured electric field. The resulting value of the temperature is about 9500 K.

Second we consider the AC components of the plate voltages. An example of a measurement is given in Fig. 8.5. Here the AC components of the voltages of 5 different plates are given as a function of time. These measurements were made just before time t_e in Fig. 8.2, so at a constant value of the pressure. The sampling time is 4 μs, the total measuring time is 4.1 ms. The axial positions of the plates are given at the right-hand side of the figure. The dip in the middle of the figure is caused by a fault in the control mechanism of the power

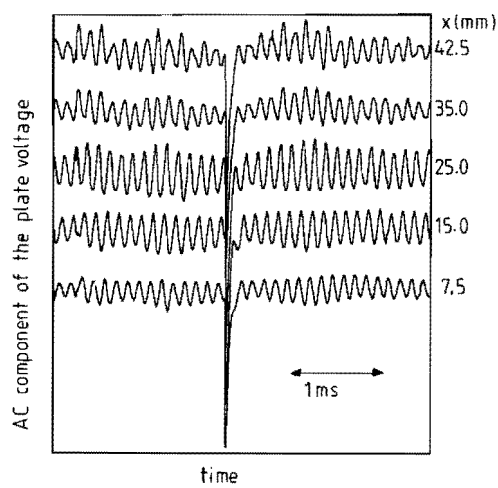

FIG. 8.5. AC components of the voltages of 5 plates as a function of time. The axial positions of the plates are given at the right-hand side of the figure. The sampling time is 4 μs, the total measuring time is 4 ms. The dip in the middle of the figure is caused by a fault in the control mechanism of the power supply. The mass flow is 0.5 g/s and the pressure at the cathode side is 1.5 bar.

supply. For all plates the frequency of the periodic fluctuations visible in Fig. 8.5 is about 8.1 kHz. The periodic fluctuations are the same as those presented in Fig. 8.2b which are recorded with a much longer sampling time. A phase difference is present between the fluctuations at succesive plates. Fluctuations measured at downstream positions in the channel are somewhat retarded with respect to the fluctuations measured on the plate at x = 7.5 mm. The differences in phase (and time) are smaller for larger values of the axial position, x. Dividing the distances between two plates by the time differences occurring in the fluctuations yields speeds between 400 and 700 m/s.

In order to explain the kind of fluctuations measured here, the magnitude of this speed can be used. To this end the theory enunciated in Chapter 7 is applied. According to Eq. (7.38), the fluctuations can propagate at three different speeds: $u + a$, $u - a$, and u. The speed of sound, a, is about 1600 m/s at a temperature of 9500 K (see Fig. 7.8). The mass flow applied in the measurement given in Fig. 8.5 is 0.5 g/s. According to Fig. 7.12 this corresponds with a Mach number, $M = u/a$, of about 0.3 and consequently the flow speed, u, is about 550 m/s. So from the measured temperature and the applied mass flow one can deduce that $u + a \approx 2150$ m/s, $u - a \approx -1050$ m/s, and $u \approx 550$ m/s. The speed given by the time differences between the fluctuations has values between 400 and 700 m/s, depending on the axial position. The fluctuations are therefore assumed to be frozen in the plasma and thus moving with the flow speed, u. An evaluation of the fluctuations in the plate voltages leads to the conclusion that the flow speed of the plasma is a function of the axial position. The speed determined in this way increases with the axial position.

The frequency of the fluctuations in Fig. 8.5 is 8.1 kHz. The frequencies measured at other experimental conditions are about the same. The fluctuations are probably connected with the geometry of the plasma channel. The plates of the arc are namely separated by silicon spacers with a larger inner diameter, thus forming cavities between the plates. In another arc, where these cavities are filled up with a ceramic material, no fluctuations where measured (KR085).

8.4 Results and discussion

The experimental techniques which are used to measure the plasma properties in a cascade arc with flow are described in the previous sections. A theoretical model has been presented in Chapter 7. In this section experimental and theoretical results are compared and discussed. All results given in this section refer to an argon cascade arc to which the following conditions apply:

a) the length of the plasma channel is 50 mm,

b) the diameter of the plasma channel is 5 mm,

c) the electric current through the arc is 60 A,

d) the mass flow through the arc is 0.5 g/s.

The measured entrance pressure is 1.5 bar. The temperature in a cascade arc at 60 A and without flow is 12,700 K. With flow this temperature is lower. Consequently the Mach number in the arc is smaller than one and the exit pressure is one bar (see Subsec. 7.4.2). These data will be needed later on in the model calculations.

The experimentally and theoretically determined temperatures and flow speeds are given in Fig. 8.6 as a function of the axial position. The upper part of this figure shows the temperature and the lower part the flow speed. First we will consider the results which are obtained experimentally.

The temperature has been determined by means of the measured electric field (see previous section). The temperature is about 9500 K at the entrance of the channel and increases a little to 9800 K at the exit. Possible faults in the determination of the temperature are caused by the assumptions involved:

a) in the calculation of the electric conductivity the equilibrium composition of the plasma is used,

b) the effective cross-section of the arc is assumed to be constant.

Nevertheless we will use the values given in Fig. 8.6.

The pressure at the entrance and at the exit of the channel are also known (1.5 and 1.0 bar respectively). This permits us to calculate the flow speed at these two places. The mass flow, ϕ, through the arc can be written as $\phi = \rho u A$ where A denotes the cross-section of the channel (1.96×10^{-5} m^2). Substituting Eq. (7.13) gives u as a function of p, T, and ϕ:

$$u = \frac{\phi}{\rho A} = \frac{\phi RT(1 + \alpha)}{pA} \tag{8.2}$$

Using the above mentioned values of the temperature and the pressure and using ϕ = 0.5 g/s gives u = 340 m/s at x = 0 mm and u = 580 m/s at x = 50 mm. These flow speeds are denoted by the dots in Fig. 8.6. The squares denote the speeds which are determined by means of the fluctuations in the plate voltages. These fluctuations are given in Fig. 8.5 for five different plates. The resulting flow speeds are assigned to axial positions just in between the axial positions of the two plates which are used in the measurements. The error bars originate from the uncertainty which is involved in the determination of the phase differences.

Now the set of differential equations given by Eq. (7.53) can be solved by numerical integration from x = 0 to x = 50 mm. At x = 0, the

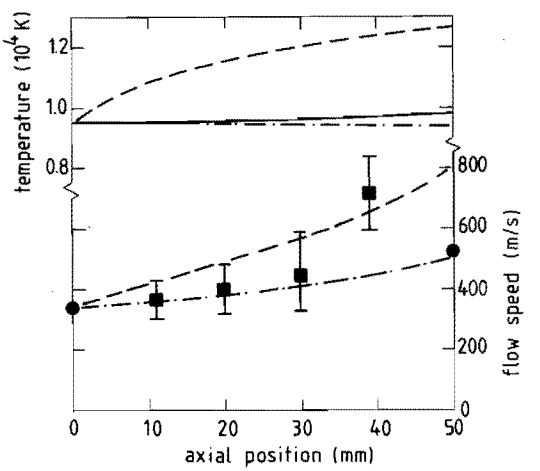

FIG. 8.6. Experimental and theoretical values of the temperature (upper part) and the flow speed (lower part) as a function of the axial position. The experimentally determined temperature is given by the solid curve, the experimentally determined flow speed by dots (obtained from the measured temperature) and by squares (obtained from the plate voltage fluctuations). The results of model calculations are given by dashed curves ($q/u = IE/\phi$) and dashed-dotted curves (q = 0).

entrance conditions p = 1.5 bar, u = 340 m/s, and T = 9500 K are used. The friction factor, f, is taken to obtain p = 1 bar at the exit of the channel. The source term, q, in the energy balance (right-hand side of Eq.(7.9)) still has to be considered This source term is the net energy transferred into the plasma being available to heat and to accelerate the flow. In an arc without flow the power input by ohmic dissipation is balanced by different energy loss processes (TIM84). The losses are, in order of importance, outward diffusion of ionized particles, radial heat conductivity, and escape of radiation. The last two processes are together only a few per cent of the ohmic dissipation. In an arc with flow, the ohmic dissipation is larger because of the higher electric field. As a consequence of the lower temperature and the accordingly lower electron density, the losses by radiation are smaller and can be neglected. The same applies to the classical heat conductivity. However, in a turbulent flow, the conduction may be enhanced by heat transport through eddies. Also the contribution from outward diffusion, which is contained in a term proportional to the deviation from equilibrium (δb_1), is difficult to evaluate. To estimate the influence of the source term in the right-hand side of the energy balance Eq (7.9), two different situations are considered here. The first one is to disregard all energy losses in q, thus assuming that the source term is equal to the ohmic dissipation. The second one is to assume that the energy losses in q, which are due to the deviation from equilibrium and turbulent heat conduction, balance the ohmic dissipation and consequently the source term, q, is zero.

In the first case the term q/u occurring in Eq. (7.53) is rewritten:

$$\frac{q}{u} = \frac{JE}{\rho u} = \frac{IE}{\rho u A} = \frac{IE}{\phi} \tag{8.3}$$

The term JE is the ohmic dissipation per unit volume, which divided by the mass density, ρ, gives the required ohmic dissipation per unit mass. Substituting I = 60 A, ϕ = 0.5 g/s, and E = 2000 V/m in Eq. (8.3) yields $q/u = 2.4 \times 10^8$ m/s^2. When for the friction factor, f, the value f = 0.56 is used, one obtains p = 1 bar at the end of the channel. The in this way calculated temperature and flow speed are given as a function of the axial position by the dashed curves in Fig. 8.6. In the second case, with q = 0, one has to use f = 0.89 to get the required exit pressure. The calculated temperature and flow speed

are given by dashed-dotted curves in the same figure.

The energy loss caused by turbulence, q_t, can be estimated by using the Reynolds analogy (MCA54). This yields

$$q_t = uc_p \Delta T(f/2D) \tag{8.4}$$

Here ΔT is the temperature difference between the bulk of the plasma and the wall. The term q_t/u should be subtracted from q/u as given by Eq. (8.3). An evaluation of this term yields $q_t/u = 7 \times 10^8$ m/s^2 for $c_p = 10^3$ J/(kgK), $\Delta T = 10^4$ K, $f = 0.7$, and $D = 5 \times 10^{-3}$ m. This value for q_t/u is probably too large because the value which is used for f was obtained by fitting f to get $p = 1$ bar at the exit of the channel. Therefore in this value of f already the contribution of the turbulence to the friction has been accounted for. Nevertheless the term q_t/u may be of the same order as the ohmic dissipation. The turbulent heat conductivity and the energy loss due to deviation from equilibrium deserve further investigastions

For both cases considered here, the friction parts and the power parts of Eq. (7.53) are given in Table 8.1 to illustrate the influence of the friction and the power input. The relative pressure gradient, given by Eq. (7.53a), is almost independent of the assumption made in the evaluation of the net power input. With respect to the gradients

TABLE 8.1. The different terms in the final set of equations given by Eq. (7.53) in m^{-1} at $x = 0$, $I = 60$ A, and $\phi = 0.5$ g/s for the two cases considered in this chapter:

a) $f = 0.56$ $(q/u) = 2.4 \times 10^8$ m/s^2

b) $f = 0.89$ $(q/u) = 0$

	a) friction part	a) power part	a) total	b) friction part
$\frac{1}{p}\frac{\partial p}{\partial x}$	- 3.42	- 1.37	- 4.79	- 5.43
$\frac{1}{u}\frac{\partial u}{\partial x}$	+ 3.31	+ 23.8	+ 27.1	+ 5.25
$\frac{1}{T}\frac{\partial T}{\partial x}$	- 0.116	+ 20.2	+ 20.1	- 0.184

in the flow speed and in the temperature, the situation is quite different. In case a) ($q > 0$) the power parts in the Eqs. (7.53b) and (7.53c) are much larger than the friction parts. In case b) ($q = 0$) the power parts are of course zero. So both the gradient of the flow speed and the gradient of the temperature depend very much on the assumption made with respect to the net power input, q. This can also be seen in Fig. 8.6. The agreement between the experimental and the theoretical result is better when $q = 0$ is used (dashed-dotted curves). The experimentallly determined flow speed at $x = 39$ mm is however too large in that case. The values of the pressure and the mass density calculated in both cases are shown in Fig. 8.7 as a function of the axial position. The two curves which give the pressure are almost the same as can be expected from the values of $(1/p)(\partial p/\partial x)$ in Table 8.1. The differences between the two curves which denote the mass density are much larger. This is caused by the large differences between the calculated temperatures in both cases. Note that the values of the friction factor mentioned above are higher than that of a turbulent flow in a rough pipe which is in the order of 0.1 (BOB80). This could be expected considering the irregular shape of the channel wall and the possible occurrence of turbulence.

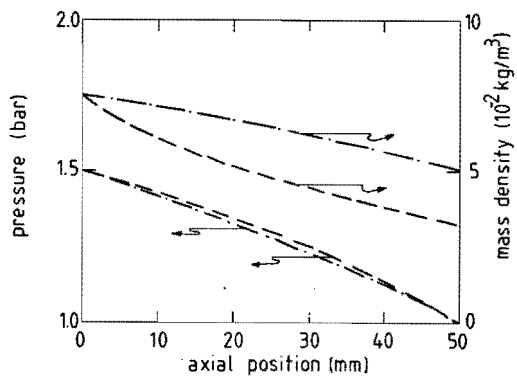

FIG. 8.7. Theoretical values of the pressure and the mass density as a function of the axial position. The dashed curves are obtained with $q/u = IE/\phi$ and the dashed-dotted curves with $q = 0$.

8.5 Conclusions

The results of both the theory described in Chapter 7 and the experiments given in this chapter have been presented in the previous section. Here the conclusions of both parts of this work concerning a cascade arc with flow are summarized.

The experiments on the cascade arc with flow have been performed at a channel with a length of 50 mm and a diameter of 5 mm. A current of 60 A and a mass flow of 0.5 g/s have been used. At these conditions, the entrance pressure of the channel is 1.5 bar. The flow of a singly ionized argon plasma through a channel with a constant cross-section has been considered theoretically. The one-dimensional formulations of the mass, momentum, and energy balances, together with the equation of state, have been used. Friction with the wall (momentum balance) and a source term in the energy balance have been taken into account. The thermodynamic properties of the plasma considered here have been worked out. The degree of ionization turns out to be an important quantity because the specific enthalpy, the specific heats, the speed of sound, and the isentropic coefficients depend very strongly on it. An analysis of the above mentioned equations shows that waves with three different speeds can propagate through the plasma: sound waves with $u + a$ and with $u - a$, and a thermal wave with the flow speed, u. For a numerical evaluation of a model of a stationary flowing plasma, one needs experimentally determined values of the boundary conditions (pressure, flow speed, and temperature at the entrance of the channel). The Mach number proves to be smaller than one (subsonic flow) at the applied experimental conditions. The exit pressure is equal to the pressure of the air into which the plasma flows (1 bar) because the flow is subsonic.

The DC parts of the measured plate voltages yield an arc temperature of about 9500 K which is almost independent of the axial position. Using this temperature, the mass flow, and the values of the entrance and the exit pressures, one can determine the flow speed at the entrance (340 m/s) and at the exit of the channel (580 m/s). The AC parts of the measured plate voltages lead to values of the flow speed between 400 and 700 m/s, depending on the axial position.

The experimentally determined values of the pressure, the flow speed, and the temperature at the entrance have been used in the the-

oretical model. The gradients of the flow speed and of the temperature turn out to be too large when the source term in the energy balance is taken equal to the ohmic dissipation. The assumption that the dissipation is balanced by energy losses due to deviation from equilibrium and turbulent heat conductivity, leads to a better agreement between theory and experiment. In a correct theoretical description, these effects should also be taken into account in the basic formulation. The friction factor has been fitted to obtain an exit pressure of 1 bar. This yields a value of 0.56 when the source term in the energy balance is taken equal to the ohmic dissipation and a value of 0.89 when the source term is assumed to be zero.

9. CONCLUSIONS

The investigations of the plasma of a closed cycle MHD generator concentrated on the filaments which form, in clusters, the highly conducting arcs (streamers) in such a plasma. Collective scattering of CO_2 laser light has been used to determine the radial scale length and the electron density of these filaments. Heterodyne detection is used to obtain a resolution in the submillimeter range. A discharge model, describing the distribution of the filaments in a streamer, is used to interpret the measured signals. The measured value of the radius of a filament is $(1.3 \pm 0.2) \times 10^{-4}$ m. This result is only weakly dependent on the different assumptions made for the discharge model. Simultaneously a maximum value for the electron density of 5×10^{20} m^{-3} is found. This is a factor 5 to 10 smaller than that found in other experiments. The determined electron density strongly depends on the assumed streamer features and in particular on the inclination of a streamer with respect to the scattering diagnostic.

The mass and energy balances for the electrons in a filament with a radius between 0.1 and 1 millimetre are analysed for a specific condition for the heavy particles (with T_h = 1000 K, $p = 5 \times 10^4$ Pa, and $SF = 10^{-3}$). The overpopulations of the excited levels and the source term in the mass balance (ionization and recombination) are evaluated by means of a collisional radiative (CR) model for the neutral cesium system. The overpopulation of an excited level q is given in the form $\delta b_q = r_q \delta b_1 + \rho_q$, in which r_q and ρ_q depend on the electron temperature, the escape of resonance radiation, and the number of levels taken into account. The source term in the mass balance is given by $n_e(\upsilon_1 \delta b_1 - \upsilon_0)$, in which υ_1 and υ_0 depend on the same quantities. Different broadening mechanisms of resonance lines are considered (Doppler, Stark, Resonance, and Van der Waals broadening). The Van der Waals broadening is dominant. Consequently the escape of resonance radiation depends mainly on the temperature and the density of the heavy particles. The excited levels can be divided in groups. The overpopulations of the different levels of a group are about equal to each other. A CR model with 10 levels suffices to obtain a good description of the deviation from equilibrium and the resulting non-equilibrium ionization. The filament radius is important because it determines the escape of resonance radiation. This analysis yields

small deviations from equilibrium, even at the small radii considered. A number of source terms in the energy balance have been analysed. Close to the axis of the filament, the ohmic dissipation and the electron heat conductivity constitute the most important terms. The combined balances, analysed close to the axis, yield that a stable stationary solution is only possible for electron densities greater than 3×10^{21} m^{-3} and electron temperatures greater than 4300 K (85% of the cesium has to be ionized). Using the measured value of the radius of the electron density profile results in electric fields between 3 and 4 kV/m and current densities averaged over a filament of 3.0×10^{5} to 4.5×10^{5} A/m^2. These values correspond well with values obtained by others from measurements of line and continuum emission.

The experiments on the cascade arc with flow have been performed at a channel with a length of 50 mm and a diameter of 5 mm. A current of 60 A and a mass flow of 0.5 g/s have been used. The entrance pressure of the channel is 1.5 bar at these conditions. The flow of a singly ionized argon plasma through a channel with a constant cross-section has been considered theoretically. The one-dimensional formulations of the mass, momentum, and energy balances, together with the equation of state, have been used. Friction with the wall (momentum balance) and a source term in the energy balance have been taken into account. The degree of ionization turns out to be an important quantity with respect to the thermodynamic properties: the specific enthalpy, the specific heats, the speed of sound, and the isentropic coefficients depend very strongly on it. An analysis of the above mentioned equations shows that waves with three different speeds can propagate through the plasma: sound waves with speeds $u + a$ and $u - a$, and a thermal wave with the flow speed, u. For a numerical evaluation of a model of a stationary flowing plasma, one needs experimentally determined values of the boundary conditions (pressure, flow speed, and temperature at the entrance of the channel). The Mach number proves to be smaller than one (subsonic flow) at the applied experimental conditions. The exit pressure is equal to the pressure of the air into which the plasma flows (1 bar) because the flow is subsonic.

The DC parts of the measured plate voltages yield an arc temperature of about 9500 K which is almost independent of the axial position. Using this temperature, the mass flow, and the values of the entrance and the exit pressures, one can determine the flow speed at

the entrance (340 m/s) and at the exit of the channel (580 m/s). The AC parts of the measured plate voltages lead to values of the flow speed between 400 and 700 m/s, depending on the axial position.

The experimentally determined values of the pressure, the flow speed, and the temperature at the entrance have been used in the theoretical model. The gradients of the flow speed and of the temperature turn out to be too large when the source term in the energy balance is taken equal to the ohmic dissipation. The assumption that the dissipation is balanced by energy losses due to a deviation from equilibrium, leads to a better agreement between theory and experiment. In a correct theoretical description, the deviation from equilibrium should also be taken into account in the basic formulation of the model. The friction factor has been fitted to obtain an exit pressure of 1 bar. This yields a value of 0.56 when the source term in the energy balance is taken equal to the ohmic dissipation and a value of 0.89 when the source term is assumed to be zero.

REFERENCES

AUB85 J. Aubreton, (private communication).

BAL85 W.J.M. Balemans et al, Internal Report, Eindhoven University of Technology, EG/85/392 (accepted for publication in J. of Prop. and Power), 1985.

BAL86 W.J.M. Balemans and L.H.Th. Rietjens, IXth Int. Conf. on MHD Electrical Power Generation, Tsukuba, Japan, Nov. 1986.

BAT81 J. Batenburg, Internal Report, Eindhoven University of Technology, VDF/NT-81-11, 1981.

BAU76 U.H. Bauder, Appl. Phys. **9**, 105 (1976).

BLO73 J.H. Blom, Ph.D. thesis, Eindhoven University of Technology, "Relaxation phenomena in an MHD generator with pre-ionizer", 1973.

BLO75 J.H. Blom, et al, XIth Int. Conf. on MHD Electrical Power Generation, Washington D.C., 1975, p. III.73.

BOB80 W. Bober and R.A. Kenyon, "Fluid Mechanics", John Wiley and Sons, New York, 1980.

BOL85 L. Bol, Internal Report, Eindhoven University of Technology, VDF/NT-85-04, 1985.

BOR82 C.A. Borghi, Ph.D. thesis, Eindhoven University of Technology, "Discharges in the inlet region of a noble gas MHD generator", 1982.

BOS85 J.C.N. Bosma, A. Veefkind, J.F. Uhlenbusch, and L.H.Th. Rietjens, 23th Symp. on Eng. Asp. of MHD, Somerset, Pa., 1985, p. 450.

BRA65 S.I. Braginskii, in "Reviews of plasma physics", Ed. M.A. Leontovich, Consultants Bureau, New York, 1965.

CAB71 F. Cabannes and J.C. Chapelle, in "Reactions under plasma conditions", Ed. M. Venugopalan, Wiley Interscience, John Wiley and Sons, New York, 1965.

CIL75 W.A. Cilliers, J.D. Hey, and J.P.S. Rash, J. Quant. Spectrosc. Radiat. Transfer **15**, 963 (1975).

DRA65 H.W. Drawin and P. Felenbok, "Data for Plasmas in Local Thermodynamic Equilibrium", Gauthiers-Villars, Paris, 1965.

DRA73A H.W. Drawin, Phys. Lett. **42A**, 423 (1973).

DRA73B H.W. Drawin and F. Emard, Z. Naturforsch. **28a**, 1289 (1973).

DRA73C H.W. Drawin and F. Emard, Beitr. Plasmaphysik **13**, 143 (1973).

FAB76 M. Fabry, J. Quant. Spectrosc. Radiat. Transfer **16**, 127 (1976).

FLI83 H.J. Flinsenberg, Ph.D. thesis, Eindhoven University of Technology, "Fossil fuel fired closed cycle MHD power generating experiments", 1983.

GRI63 H.R. Griem, Phys. Rev. **131**, 1170 (1963).

GRI64 H.R. Griem, "Plasma Spectroscopy", McGraw-Hill, New York, 1964.

GRI74 H.R. Griem, "Spectral Line Broadening by Plasmas", Academic Press, New York, 1974.

GRY65 M. Gryzinski, Phys. Rev. **138**, A336 (1965).

HAA86 J.C.M. de Haas, H.J.W. Schenkelaars, P.J. van de Mortel, D.C. Schram, and A. Veefkind, Phys. Fluids **29**, 1725 (1986).

HEL80 W. Hellebrekers, Ph.D. thesis, Eindhoven University of Technology, "Instability analysis in a nonequilibrium MHD generator", 1980.

HOL47 T. Holstein, Phys. Rev. **72**, 1212 (1947).

HOL51 T. Holstein, Phys. Rev. **83**, 1159 (1951).

HSU84 K.C. Hsu and E. Pfender, Plasma Chem. and Plasma Process. **4**, 219 (1984).

IRO79 F.E. Irons, J. Quant. Spectrosc. Radiat. Transfer **22**, 21 (1979).

KAF79 H. Kafrouni, J.M. Bagneaux, A. Gleizes, and S. Vacquie, J. Quant. Spectrosc. Radiat. Transfer **21**, 457 (1979).

KAR61 W.J. Karzas and R. Latter, Astrophys. J. **6**, 665 (1961).

KLE69 M. Klein, Ph.D. thesis, University of California, "Radiation trapping processes in the pulsed ion laser", 1965.

KRO85 G.M.W. Kroesen, Th.J. Bisschops, J.C.M. de Haas, D.C. Schram, and C.J. Timmermans, 7th Int. Symp. on Plasma Chem., Eindhoven, The Netherlands, 1985, Paper Number P-7-5, p. 698.

MAE56 H. Maecker, Z. Naturforsch. **11a**, 457 (1956).

MCA54 W.H. McAdams, "Heat Transmission", McGraw-Hill, New York, 1954.

MAT82 R. Matsuzaki, Jpn. J. Appl. Phys. **21**, 1003 (1982).

MES82 A.J. Mesland, Ph.D. thesis, Eindhoven University of Technology, "Linear and nonlinear instability theory of a noble gas MHD generator", 1982.

MIT73 M. Mitchner and C.H. Kruger, "Partially Ionized Gases", John Wiley and Sons, New York, 1973.

MUL86 J.J.A.M. van der Mullen, Ph.D. thesis, Eindhoven University of Technology, "Excitation equilibria in plasmas", 1986.

NIC82 K.P. Nick, Ph.D. thesis, University of Kiel, FRG, "Analyse des Plasmazustandes und Bestimmung Atomaren Konstanten in einem Argon-Kaskadenbogen", 1982.

NOR66 D.W. Norcross and P.M. Stone, J. Quant. Spectrosc. Radiat. Transfer **6**, 277 (1966).

OER66 H. Oertel, "Stossrohre", Springer Verlag, Vienna, 1966.

OLS63 H.N. Olsen, in "Physico Chemical Diagnostics of Plasmas", Ed. T.P. Anderson et al., Northwestern University Press, 1963.

OWC64 J.A. Owczarek, "Fundamentals of Gas Dynamics", International Textbook Company, Scranton, Penn., 1964.

POT81 B.F.M. Pots, J.J.H. Coumans, and D.C. Schram, Phys. Fluids **24**, 517 (1981).

ROS81 R.J. Rosado, Ph.D. thesis, Eindhoven University of Technology, "An investigation of non-equilibrium effects in thermal argon plasmas", 1981.

SCH83 D.C. Schram, H.W.H. Van Andel, G. Le Clair, and P. Brodeur, Plasma Phys. **25**, 1133 (1983).

SCH84 H.J.W. Schenkelaars, Internal Report, Eindhoven University of Technology, VDF/NT-84-10, 1984.

SEI76 G.R. Seikel et al, 15th Symp. on Eng. Asp. of MHD, Philadelphia, Pa, 1976, p. III.4.

SEN82 A.F.C. Sens, V.A. Bityurin, J.M. Wetzer, A. Veefkind, and J.F.G. Brauers, 20th Symp. on Eng. Asp. of MHD, Irvine, Calif., 1982, p. 10.6.

SLU80 R.E. Slusher and C.M. Surko, Phys. Fluids **23**, 472 (1980).

TIM84 C.J. Timmermans, Ph.D. thesis, Eindhoven University of Technology, "An investigation of pulsed high density plasmas", 1984.

TIM85 C.J. Timmermans, R.J. Rosado, and D.C. Schram, Z. Naturforsch. **40a**, 810 (1985).

UHL70 J.F. Uhlenbusch, E. Fisher, and J. Hackmann, Z. Phys. **239**, 120 (1970).

UHL74 J.F. Uhlenbusch, "Gaseous Electronics", North Holland Publishing Company, Amsterdam, 1974.

VAL84 P.M. Vallinga, Internal Report, Eindhoven University of Technology, VDF/NT-84-02, 1984.

VEE78 A. Veefkind, 17th Symp. on Eng. Asp. of MHD, Stanford, Calif., 1978, p. H.3.1.

WET80 J.M. Wetzer, Internal Report, Eindhoven University of Technology, EG/80/284, 1980.

WET83 J.M. Wetzer, IEEE Trans. Plasma Sci. **PS-11** (2), 72 (1983).

WET84 J.M. Wetzer, Ph.D. thesis, Eindhoven University of Technology, "Spatially resolved determination of plasma parameters of a noble gas linear MHD generator", 1984.

SUMMARY

This thesis deals with the fundamental aspects of two plasmas applied in technological processes. The first one is the cesium seeded argon plasma in a closed cycle Magnetohydrodynamic (MHD) generator, the second is the thermal argon plasma in a cascade arc with an imposed flow. Both plasmas have a pressure in the order of one bar.

The investigations of the plasma of a closed cycle MHD generator are concentrated on the dimensions of the filaments which are present in such a plasma. Collective scattering of the light of a CO_2 laser with heterodyne detection has been used to determine the radius and the electron density of these filaments. A discharge model was formulated to interpret the measured signals. The measured value of the radius is $(1.3 \pm 0.2) \times 10^{-4}$ m which weakly depends on the assumptions made for the discharge model. For the electron density at the axis a value of 5×10^{20} m^{-3} is found which is a factor 5 to 10 smaller than found in other experiments. Because it was not possible to take all light losses into account in the calibration, this value has to be considered as a minimum.

The mass and energy balances for the electrons are analysed. Because of the low electron temperature in an MHD generator, only the cesium is ionized. A collisional radiative (CR) model for the neutral cesium system with at maximum ten effective levels has been used. The CR model was formulated in terms of the overpopulations of the effective levels with respect to the Saha population. Different broadening mechanisms of resonance lines were considered because the escape of resonance radiation is important. The overpopulations of the excited levels as well as the source term can be written in a form which is linearly dependent on the overpopulation of the ground level. For cesium, the excited levels can be divided in groups in which the overpopulations are about equal. A CR model with ten levels suffices to obtain a good description of the deviation from equilibrium and the resulting non-equilibrium ionization. The deviation from equilibrium is small and so the electron density and the electron temperature are strongly coupled. Therefore the terms in the mass and the energy balances are reformulated as functions of the electron density and the overpopulation of the ground level which describes the deviation from equilibrium. The ohmic dissipation and the electron heat conductivity

are the most important terms in the energy balance. The combined mass and energy balances yield stable stationary solutions for electron densities greater than 3×10^{21} m^{-3} and electron temperatures greater than 4300 K. Using the measured value of the radius results in electric fields between 3 and 4 kV/m and current densities averaged over a filament of $(3.0 - 4.5) \times 10^5$ A/m^2.

The experiments on the cascade arc with flow have been performed at a channel with a length of 50 mm and a diameter of 5 mm, using a current of 60 A and a mass flow of 0.5 g/s. The entrance pressure is 1.5 bar. The flow of a singly ionized argon plasma through this channel has been considered theoretically. The equation of state and the one-dimensional formulations of the mass, momentum, and energy balances of a plasma in equilibrium have been used. Friction with the wall and a source term in the energy balance have been taken into account. This leads to three partial differential equations in the pressure, the flow speed, and the temperature. Besides sound waves, a thermal wave moving with the flow speed can occur in the plasma. The flow is subsonic at the applied experimental conditions and consequently the exit pressure equals the pressure of the air into which the plasma flows (1 bar).

The plate voltages, the mass flow, and the pressure at the entrance of the channel were measured. The electric field in the arc, which is derived from the plate voltages, is greater with flow than without flow and consequently the electrical conductivity and the temperature are lower. Using the electrical conductivity of an argon plasma in equilibrium, yields a temperature of about 9500 K which is almost independent of the axial position. With this temperature, the mass flow, and the entrance and exit pressures, one can determine the flow speed at the entrance (340 m/s) and at the exit of the channel (580 m/s). The plate voltages show fluctuations with a fixed frequency of about 8.1 kHz. These fluctuations are shifted in time at plates more downstream the channel and are assumed to be caused by perturbations moving with the flow speed. This leads to values between 400 and 700 m/s, depending on the axial position.

The experimentally determined values of the pressure, the flow speed, and the temperature at the entrance have been used as boundary conditions in the theoretical model. The friction factor has been fitted to obtain an exit pressure of 1 bar. The assumption that the

ohmic dissipation is balanced by energy losses due to a deviation from equilibrium and turbulent heat conductivity, leads to a good agreement between theory and experiment.

SAMENVATTING

Dit proefschrift behandelt de fundamentele aspecten van twee plasma's die in technologische processen worden toegepast namelijk het argon plasma met cesium inzaai in een "closed cycle" MHD generator en het thermische argon plasma in een cascadeboog waarbij een gasstroom wordt opgedrukt. De druk is in beide plasma's ongeveer één bar.

Het onderzoek naar het plasma van een MHD generator heeft zich toegespitst op de afmetingen van de filamenten die in een dergelijk plasma voorkomen. Collectieve verstrooiing van het licht van een CO_2 laser met heterodyne detectie is gebruikt om de straal van en de electronendichtheid in deze filamenten te bepalen. Een ontladingsmodel is geformuleerd om de gemeten signalen te kunnen interpreteren. De gemeten straal is $(1,3 \pm 0,2) \times 10^{-4}$ m en is nauwelijks afhankelijk van de aannamen die gemaakt zijn in het ontladingsmodel. Voor de electronendichtheid is een aswaarde gevonden van 5×10^{20} m^{-3} hetgeen een factor 5 tot 10 lager is dan de waarde die uit andere bepalingen volgt. Het was echter niet mogelijk om voor de calibratie alle lichtverliezen in rekening te brengen, zodat de genoemde waarde als een minimum beschouwd moet worden.

De massa- en de energiebalans voor de electronen zijn geanalyseerd. In een MHD generator is vanwege de lage electronentemperatuur alleen het cesium geïoniseerd. Een botsings-stralingsmodel (*BSM*) voor het cesium neutraal systeem met maximaal 10 effectieve niveaus is gebruikt. Het *BSM* is geformuleerd in de overbezettingen van de effectieve niveaus t.o.v. de Saha-bezetting. Verschillende verbredingsmechanismen van resonante lijnen zijn uitgewerkt omdat de ontsnapping van resonante straling belangrijk is. Zowel de overbezettingen van de aangeslagen niveaus als de bronterm kunnen in een lineaire afhankelijkheid van de overbezetting geformuleerd worden. De aangeslagen niveaus van cesium kunnen verdeeld worden in groepen waarbinnen de overbezettingen ongeveer gelijk zijn. Een *BSM* met tien niveaus is toereikend om een goede beschrijving van de afwijking van evenwicht en de resulterende niet-evenwichts ionisatie te geven. De afwijking van evenwicht is klein en dus zijn de electronendichtheid en -temperatuur sterk gekoppeld. De termen in de massa- en de energie-balans zijn daarom herschreven als functies van de electronendichtheid en de overbezetting van het grondniveau die de afwijking van evenwicht be-

schrijft. De ohmse dissipatie en de electronenwarmtegeleiding zijn de belangrijkste termen in de energiebalans. De gecombineerde massa- en energiebalans heeft stabiele stationaire oplossingen voor een electronendichtheid van meer dan 3×10^{21} m^{-3} en een electronentemperatuur van meer dan 4300 K. Samen met de gemeten straal leidt dit tot electrische velden van 3 tot 4 kV/m en stroomdichtheden van $(3,0 - 4,5) \times 10^5$ A/m^2 gemiddeld over een filament.

De experimenten betreffende een cascadeboog met gasstroom zijn verricht aan een kanaal met een lengte van 50 mm en een diameter van 5 mm. Hierbij werd een stroom van 60 A en een massastroom van 0,5 g/s gebruikt. De ingangsdruk is 1,5 bar. Een theoretische beschrijving van een enkelvoudig geïoniseerd plasma door dit kanaal is gegeven. De toestandsvergelijking en de ééndimensionale formuleringen van de massa-, de impuls- en de energiebalans van een plasma in evenwicht zijn gebruikt. Hierbij zijn wrijving met de wand en een bronterm in de energievergelijking in rekening gebracht. Dit leidt tot drie partiële differentiaalvergelijkingen in de druk, de stroomsnelheid en de temperatuur. Naast geluidsgolven kan er ook een thermische golf voorkomen die met de stroming meebeweegt. De stroming is subsoon onder de toegepaste omstandigheden en daarom is de uitgangsdruk gelijk aan de druk van de lucht waarin het plasma uitstroomt (1 bar).

De spanningen van de cascadeplaten, de massastroom en de ingangsdruk zijn gemeten. Het electrische veld in de boog, dat volgt uit de spanningsverschillen tussen de platen, is met stroming groter dan zonder stroming. De electrische geleidbaarheid en de temperatuur zijn daarom lager. Door gebruik te maken van de electrische geleidbaarheid van een argon plasma in evenwicht, kan vastgesteld worden dat de temperatuur ongeveer 9500 K bedraagt en nagenoeg onafhankelijk is van de plaats in de boog. De stroomsnelheid aan de ingang (340 m/s) en de uitgang (580 m/s) kunnen bepaald worden uit deze temperatuur, de massastroom en de ingangs- en uitgangsdruk. De gemeten spanningen vertonen fluctuaties met een vaste frequentie van ongeveer 8,1 kHz. Deze fluctuaties treden meer stroomafwaarts in het kanaal later op en er wordt aangenomen dat ze veroorzaakt worden door verstoringen die met het plasma meebewegen. Dit geeft waarden tussen 400 en 700 m/s, afhankelijk van de plaats in de boog.

De experimenteel bepaalde waarden van de druk, de stroomsnelheid en de temperatuur aan de ingang zijn gebruikt als randvoorwaarden in

het theoretische model. De wrijvingsfactor is zo gekozen dat er een uitgangsdruk van 1 bar verkregen wordt. De aanname dat de ohmse dissipatie gebalanceerd wordt door de energieverliezen t.g.v. een afwijking van evenwicht en turbulente warmtegeleiding, geeft een goede overeenkomst tussen theorie en experiment.

DANKWOORD

Het onderzoek dat beschreven is in dit proefschrift is uitgevoerd in twee (vak)groepen van de Technische Hogeschool Eindhoven en in beide groepen heb ik bij mijn werk veel steun ondervonden.

Wat betreft het eerste deel van het onderzoek: dank aan alle leden van de vakgroep Direkte Energieomzetting van de afdeling Electrotechniek en in het bijzonder aan degenen die bij het Schokbuisprojekt werkzaam zijn of waren. Onder de algehele leiding van prof. Rietjens heeft projektleider Bram Veefkind een sturende en coördinerende taak, niet alleen wat betreft de dagelijkse gang van zaken maar ook wat betreft het werk van de promovendi. Mijn dank heirvoor. Verschillende technici en met name Herman Koolmees, Loek Baede, Ad van Iersel, Jos Nouwen, Kees Kuijpers en Bram Bierens zorgden ervoor dat er een goed werkende installatie beschikbaar was en dat de meetgegevens ook nog verwerkt konden worden. Van Jos Wetzer kreeg ik een snelle inwijding in de "geheimen" van het MHD-werk. Daarnaast was hij gaarne bereid enkele tekeningen af te staan zodat deze in dit proefschrift opgenomen konden worden. Afstudeerder Dick Schenkelaars had een belangrijke inbreng bij zowel het theoretische als het experimentele gedeelte. Boven dien heeft hij zich bijzonder ingezet om de experimentele resultaten gepubliceerd te krijgen. Bij de metingen is gebruik gemaakt van een bestaande diagnostiek (CO_2 laser verstrooiing) van de afdeling der Technische Natuurkunde. Paul van de Mortel was een belangrijke steun bij het weer operationeel maken van deze diagnostiek na de verhuizing.

Voor wat betreft de tweede periode van het onderzoek: dank aan de leden van de onderwerpgroep Atoom- en Plasmafysica van de afdeling Technische Natuurkunde. Onder leiding van Daan Schram is er in de loop der jaren een grote ervaring met atmosferische plasma's verkregen. Leonard Bol heeft als afstudeerder bij de ombouw van de boog, de experimenten en de theorievorming zeker zijn steentje bijgedragen. Bovendien heeft hij de hoofdstukken die met zijn afstudeerwerk te maken hadden nog van commentaar voorzien. De technische ondersteuning van John Bleize en Ries van der Sande wat betreft de cascadeboog en van Bertus Hüsken wat betreft de electronica, wil ik nog extra noemen. Het fenomeen stroming was nieuw voor de onderwerpgroep. Wetenschappelijke en technische ondersteuning werden gegeven door Rini van Dongen en Jan Willems van de vakgroep Transportfysica.

Bij het vastleggen van de resultaten van het onderzoek was de opbouwende kritiek die ik kreeg van de beide promotoren en van de copromotor een belangrijke steun. Wat betreft de verwerking van geschreven tekst tot drukklare pagina's: dank aan Heleen en Paul die 99% van de letters, cijfers en overige tekens ingevoerd hebben. Dat alles er op een nette manier weer uit kwam is te danken aan de medewerking van Bertus Hüsken, Klaas Kopinga en Ger-Jan Lauwers. Ruth Gruijters verzorgde op een voortreffelijke manier het tekenwerk en Bob Timmermans was een goede hulp bij het nodige knip- en plakwerk.

Tot slot dank aan iedereen die tijdens de gewone dagelijkse gang van zaken en, tijdens de laatste periode, de ongewone gang van zaken vol begrip en steun was.

CURRICULUM VITAE

14 september 1958 geboren te Someren

juni 1976 Diploma Gymnasium β, St. Willibrord Gymnasium Deurne

april 1982 Doctoraal examen Technische Natuurkunde (met lof), afd. Technische Natuurkunde, Technische Hogeschool Eindhoven

april 1982 - april 1986: in dienst van de Stichting FOM als wetenschappelijk medewerker

april 1982 - mei 1984: werkzaam in de vakgroep Direkte Energieomzetting (Schokbuis MHD project), afd. Elektrotechniek, Technische Hogeschool Eindhoven

mei 1984 - april 1986: werkzaam in de groep Plasmafysica van de vakgroep Deeltjesfysica, afd. Technische Natuurkunde, Technische Hogeschool Eindhoven

april 1986 - nov. 1986: werkzaam als toegevoegd onderzoeker in de groep Plasmafysica van de vakgroep Deeltjesfysica, afd. Technische Natuurkunde, Technische Hogeschool Eindhoven

STELLINGEN

behorende bij het proefschrift van

J.C.M. de Haas

Eindhoven, 30 september 1986

STELLINGEN

1. Niet-volledig geïoniseerde plasma's die dicht bij lokaal thermisch evenwicht zijn, worden beter gekarakteriseerd door de elektronendichtheid dan door de elektronentemperatuur.
Dit proefschrift.

2. Heterodyne detectie van het collectief verstrooide licht, afkomstig van een CO_2 laser en verstrooid door een plasma, is een goede methode om de afmetingen van filamenten in dat plasma te meten.
Dit proefschrift.

3. In de plasmafysica dient het gebruik van het symbool γ voor de verhouding tussen c_p en c_V afgeraden te worden.
Dit proefschrift.

4. Bij Thomson-verstrooiing kan dat deel van het achtergrondsignaal dat afkomstig is van het plasma, gebruikt worden om de nauwkeurigheid van de meting te verhogen.
B. van der Sijde, S. Adema, J. de Haas, C.J.M. Denissen en M.J.F. van der Sande, Beitr. Plasmaphys. 22 (4), 357-368 (1982).

5. Cascadebogen kunnen worden gebruikt als betrouwbare intense bronnen voor toepassingen in de plasmachemie.
C.M.W. Kroesen, Th.J. Bisschops, J.C.M. de Haas, D.C. Schram en C.J. Timmermans, 7th Int. Symp. on Plasma Chem., Eindhoven, 1985, Paper P-7-5, p. 698.

6. Modellen voor de berekening van het totale rendement van een elektriciteitscentrale die uitgerust is met een MHD-generator met een gesloten kringloop, hebben pas betekenis, indien de in die modellen gehanteerde enthalpie-extractie van 25 % voor het MHD-gedeelte door experimenten, eventueel met een verantwoorde extrapolatie naar grotere systemen, verwezenlijkt is.
P. Massee en L.H.Th. Rietjens, IXth Int. Conf. on MHD Electrical Power Generation, Tsukuba, Japan, Nov. 1986

7. Een schokbuis is uitermate geschikt voor het onderzoek naar de excitatie van cesiumneutralen.

8. Bij het aangeven van een grens in de elektronendichtheid waarboven lokaal thermisch evenwicht geldig is, zijn behalve de elektronentemperatuur en de excitatie-energie van het eerste aangeslagen niveau, ook de specifieke eigenschappen van het beschouwde atoomsysteem belangrijk.
1) R. Wilson, *J. Quant. Spectrosc. Radiat. Transfer* **2**, 477 (1962),
2) H.R. Griem, *Phys. Rev.* **131**, 1170 (1963),
3) H.W. Drawin, *Z. Phys.* **225**, 470 (1969),
4) J.J.A.M. van der Mullen, *proefschrift Technische Hogeschool Eindhoven*, 1986.

9. Het belang van goede marsoptredens wordt door veel blaasorkesten onderschat.

10. Verzamelingen van stellingen zijn een bron van inspiratie voor het bedenken van nieuwe stellingen. Deze stelling is daarvan een voorbeeld.
Bloemlezing van promotiestellingen, Rijksuniversiteit te Utrecht, 1986